

Neutron star mergers: Mass ejection and the role of the nuclear equation of state

Neutronensternverschmelzungen:

Massenausstoß und die Rolle der nuklearen Zustandsgleichung

Zur Erlangung des Grades eines Doktors der Naturwissenschaften (Dr. rer. nat.)

Genehmigte Dissertation von Maximilian Jacobi aus Frankfurt am Main

Tag der Einreichung: 6. Februar 2023, Tag der Prüfung: 24. April 2023

1. Gutachten: Prof. Dr. Almudena Arcones

2. Gutachten: Dr. habil. Kai Hebeler

Darmstadt, Technische Universität Darmstadt



TECHNISCHE
UNIVERSITÄT
DARMSTADT

Physics Department
Institut für Kernphysik

Neutron star mergers:
Mass ejection and the role of the nuclear equation of state
Neutronensternverschmelzungen:
Massenausstoß und die Rolle der nuklearen Zustandsgleichung

Accepted doctoral thesis by Maximilian Jacobi

Date of submission: 6. Februar 2023
Date of thesis defense: 24. April 2023

Darmstadt, Technische Universität Darmstadt

Bitte zitieren Sie dieses Dokument als:
URN: urn:nbn:de:tuda-tuprints-247811
URL: <http://tuprints.ulb.tu-darmstadt.de/24781>
Jahr der Veröffentlichung auf TUprints: 2023

Dieses Dokument wird bereitgestellt von tuprints,
E-Publishing-Service der TU Darmstadt
<http://tuprints.ulb.tu-darmstadt.de>
tuprints@ulb.tu-darmstadt.de

Die Veröffentlichung steht unter folgender Creative Commons Lizenz:
Namensnennung – Weitergabe unter gleichen Bedingungen 4.0 International
<https://creativecommons.org/licenses/by-sa/4.0/>

Abstract

Binary neutron star (BNS) mergers are fascinating astrophysical events that are likely responsible for the production of about half of the heavy elements in the universe. The nuclear equation of state (EOS) plays a crucial role in the dynamics of BNS mergers. However, it is highly uncertain due to the lack of knowledge on nuclear interaction at high densities. Binary neutron star mergers emit gravitational waves (GWs) and produce an optical transient called kilonova (KN) which is powered by the radioactive decay of freshly synthesized heavy nuclei. This makes them ideal sources for multi-messenger observations providing valuable information about the dynamics of the merger and the properties of the ejected matter. By comparing the predictions of numerical simulations of BNS mergers with multi-messenger observations, it is possible to derive constraints for the EOS at high densities. This makes BNS mergers incredibly useful laboratories for studying the EOS at very high densities.

The first part of this thesis investigates the influence of the EOS on BNS mergers in a systematic way. We perform three-dimensional (3D) general-relativistic hydrodynamics simulations with eight different EOS models, where we systematically vary the effective mass, incompressibility, symmetry energy, and saturation point of nuclear matter. By analyzing the relationship of these nuclear matter properties with the evolution of the merger remnant, post-merger GW signal, and ejecta, we uncover novel insights into the connection between the EOS and the outcome of BNS mergers. We find, that the deformation of the massive neutron star (NS) after the merger is related to the incompressibility, which has implications for the post-merger GW signal and mass ejection. Furthermore, we identify correlations of the tidal and shock-heated dynamical ejecta components with the incompressibility and effective mass.

The second part of this work concerns long-term simulations of the accretion disk phase of BNS mergers. The largest component of the ejecta in a BNS merger originates from the post-merger accretion disk. Thus, it is necessary to perform numerical simulations for multiple seconds to obtain a complete picture of the ejected matter. However, running 3D simulations for such long times requires a huge amount of computational resources. We circumvent this issue by simulating the accretion-disk phase of the merger in two dimensions (2D) while assuming axisymmetry which greatly reduces the computational cost of the simulations. To consistently link a 2D simulation of the accretion disk to a 3D simulation of the merger, we create the 2D initial data using the configuration of the merger remnant from the 3D simulation. We describe the methods we use for the axisymmetric simulations and the creation of the initial data. Moreover, we perform several tests of these methods and discuss the results.

Zusammenfassung

Verschmelzungen von binären Neutronensternen (BNS) sind faszinierende astrophysikalische Ereignisse, die wahrscheinlich für die Produktion von etwa der Hälfte der schweren Elemente im Universum verantwortlich sind. Die nukleare Zustandsgleichung (ZG) spielt eine entscheidende Rolle bei der Dynamik von BNS-Verschmelzungen. Sie ist jedoch aufgrund mangelnder Kenntnisse über die nukleare Wechselwirkung bei hohen Dichten höchst unsicher. Binäre Neutronensternverschmelzungen senden Gravitationswellen (GW) aus und erzeugen eine optische Erscheinung namens Kilonova, die durch den radioaktiven Zerfall frisch synthetisierter schwerer Kerne angetrieben wird. Dies macht sie zu idealen Quellen für Multi-Messenger-Beobachtungen, die wertvolle Informationen über die Dynamik der Verschmelzung und die Eigenschaften der ausgestoßenen Materie liefern. Durch den Vergleich der Vorhersagen numerischer Simulationen von BNS-Verschmelzungen mit Multi-Messenger-Beobachtungen ist es möglich, Einschränkungen für die ZG bei hohen Dichten abzuleiten. Dies macht BNS-Verschmelzungen zu unglaublich nützlichen Laboratorien für die Untersuchung der ZG bei sehr hohen Dichten.

Der erste Teil dieser Arbeit untersucht den Einfluss der ZG auf BNS-Verschmelzungen auf systematische Weise. Wir führen dreidimensionale (3D) allgemein-relativistische Hydrodynamiksimulationen mit acht verschiedenen ZG-Modellen durch, wobei wir systematisch die effektive Masse, Inkompressibilität, Symmetrieenergie und den Sättigungspunkt der Kernmaterie variieren. Durch die Analyse der Beziehung dieser Kernmaterieeigenschaften mit der Entwicklung des Verschmelzungsüberrests, dem GW-Signal nach der Verschmelzung und den Ejekta gewinnen wir neue Erkenntnisse über den Zusammenhang zwischen der ZG und dem Ergebnis von BNS-Verschmelzungen. Wir stellen fest, dass die Deformation des massereichen Neutronensterns nach der Verschmelzung mit der Inkompressibilität zusammenhängt, was Auswirkungen auf das GW-Signal und den Massenauswurf nach der Verschmelzung hat. Darüber hinaus identifizieren wir Korrelationen zwischen den Gezeiten- und schock-erhitzten dynamischen Ejekta-Komponenten mit der Inkompressibilität und der effektiven Masse.

Der zweite Teil dieser Arbeit behandelt Langzeitsimulationen der Akkretionsscheibenphase von BNS-Verschmelzungen. Die größte Komponente der Ejekta bei einer BNS-Verschmelzung stammt aus der Akkretionsscheibe nach der Verschmelzung. Daher ist es notwendig, numerische Simulationen für mehrere Sekunden durchzuführen, um ein vollständiges Bild der ausgestoßenen Materie zu erhalten. Die Durchführung von 3D-Simulationen über so lange Zeiträume erfordert jedoch eine große Menge an Rechenressourcen. Wir umgehen dieses Problem, indem wir die Akkretionsscheibenphase der Verschmelzung in zwei Dimensionen (2D) simulieren, wobei wir Rotationssymmetrie annehmen, was die Rechenkosten der Simulationen erheblich reduziert. Um eine 2D-Simulation der Akkretionsscheibe konsistent mit einer 3D-Simulation der Verschmelzung zu verknüpfen, erstellen wir die 2D-Ausgangsdaten unter Verwendung der Konfiguration des Verschmelzungsüberrests aus der 3D-Simulation. Wir beschreiben die Methoden, die wir für die achsensymmetrischen Simulationen und die Erstellung der Ausgangsbedingungen verwenden. Außerdem führen wir mehrere Tests dieser Methoden durch

und diskutieren die Ergebnisse.

Contents

1. Introduction	1
2. Physical background	5
2.1. Dynamics of merging neutron stars	5
2.1.1. Inspiral and merger	6
2.1.2. Fate of the remnant	6
2.1.3. Evolution of the accretion-disk	7
2.2. Gravitational waves	8
2.2.1. Inspiral gravitational wave signal	9
2.2.2. Post-merger gravitational wave signal	10
2.3. Ejection of matter	10
2.3.1. Ejecta mechanisms	11
2.3.2. r -process nucleosynthesis	14
2.3.3. Kilonovae	16
2.4. The nuclear equation of state	18
2.4.1. Statistical mechanics basics	19
2.4.2. Equations of state for astrophysical applications	19
2.4.3. Characterizing the high-density equation of state	21
2.4.4. Phenomenological models	24
3. Simulating neutron star mergers	27
3.1. Numerical relativity	27
3.1.1. 3+1 decomposition	28
3.1.2. The BSSN formulation	30
3.1.3. Choosing a coordinate system	31
3.1.4. Solving Einstein's equations numerically	33
3.1.5. Gravitational Waves	33
3.2. Relativistic hydrodynamics	34
3.2.1. The Valencia formulation	35
3.2.2. Solving Euler's equations numerically	36
3.3. Neutrino transport	37
3.3.1. Leakage scheme	38
3.3.2. M0 absorption scheme	40
3.4. Simulation setup	40
4. Impact of the equation of state in neutron star mergers	43
4.1. Methods	44
4.1.1. Equation of state models	44
4.1.2. Simulation overview	47

4.1.3. Postprocessing methods	48
4.2. Merger and post-merger dynamics	49
4.2.1. Comparison of different effective masses and incompressibilities	52
4.2.2. Comparison of Shen and SkShen	55
4.2.3. Accretion disk structure	56
4.3. Ejecta properties	59
4.4. Gravitational wave emission	64
5. Long-term modeling of the post-merger system	71
5.1. The cartoon method	72
5.2. Test cases	73
5.2.1. Constant density	73
5.2.2. Isolated neutron star	73
5.3. Realistic post-merger initial data	75
5.3.1. Hydrodynamical variables	75
5.3.2. Spacetime variables	76
5.4. Long-term post-merger simulations in 2D	79
5.4.1. Comparison of the initial data	79
5.4.2. Evolution of the remnant	81
5.4.3. Mass ejection	84
5.4.4. Instability	85
6. Summary and outlook	89
Appendices	95
A. Fluid tracers	95
Acknowledgements	109
Curriculum Vitae	111

List of Figures

2.1. Overview of the different stages during BNS mergers and the possible evolution paths of the remnant.	5
2.2. Deformed massive NS in the center of the accretion disk for two different EOS	7
2.3. Example of a power-density spectrum of a GW signal emitted during a BNS merger.	9
2.4. Ejecta components and their respective timescale	12
2.5. Distribution of the electron fraction in the xz plane	13
2.6. Atomic abundance pattern of the solar system	14
2.7. Sketch of the nucleosynthesis paths of the r and s processes	15
2.8. Sketch of the energy per particle of symmetric nuclear matter and pure neutron matter	23
3.1. Foliation of spacetime	28
4.1. Pressure versus density at $T = 0$ and $Y_e = 0.1$ for the EOS used in this paper .	45
4.2. Thermal index Γ_{th} for LS220 [†] , $m_{0.8}^*$, and m_S^*	47
4.3. The mas-radius relation of cold non-rotating NSs for the EOS used in this thesis	48
4.4. Spatial mass distribution in the initial NSs in LS255 [†] and $m_{0.8}^*$	50
4.5. Temperature profiles inside the remnant in $m_{0.8}^*$	51
4.6. Average thermal, cold, and total pressure for LS220 [†]	52
4.7. Maximum density and average remnant temperature versus time	53
4.8. Complex azimuthal $m = 1$ and 2 decomposition of the density in the xy -plane	54
4.9. The average thermal pressure and temperature versus density inside the NS .	55
4.10. Evolution of the disk mass for all simulations	57
4.11. Mass-weighted histogram of the electron fraction, entropy, and temperature in the disk	58
4.12. Cumulative mass-weighted histogram of ejecta properties in model m_S^* until the end of the simulation	59
4.13. Mass-weighted histogram of the electron fraction, entropy, and asymptotic velocity of the ejected matter	60
4.14. Net neutrino heating timescale for the model m_S^*	61
4.15. Masses of the tidal, shock-heated, and disk ejecta components	63
4.16. Density distribution for the models LS175 [†] , LS220 [†] , and LS255 [†] shortly after merger	63
4.17. Distribution of the electron for the models LS220 [†] , $m_{0.8}^*$, and m_S^*	64
4.18. Mass ejection rate for the disk ejecta component as a function of time	65
4.19. Waveforms of the GW signals for all simulations	66
4.20. Post-merger GW Fourier spectra and corresponding time-frequency spectrograms	67

4.21. Comparison with various fit formulae for the post-merger GW spectrum from the literature	69
5.1. Sketch of the cartoon method	72
5.2. Evolution of the minimum and maximum density and total baryon mass in the domain for the constant density test case	74
5.3. Central density and mass conservation in the TOV test cases	74
5.4. Snapshot of the density in the xy plane of the 3D simulation before the transition to 2D	80
5.5. Density distribution in the xz plane for the 3D and 2D models at the transition time step and 40 ms later	81
5.6. Comparison of several quantities in the 2D initial data and the 3D simulation at the time of transition	82
5.7. Time series of several quantities detailing the instability, that arises in DD2_2D	83
5.8. Radial velocity in the simulations DD2_2D and DD2_2D_no ν	83
5.9. Evolution of the disk mass and the total neutrino luminosity for DD2_2D and DD2_2D_no ν	84
5.10. Mass ejection rate and total amount of mass ejected as a function of time	85
5.11. Mass ejection rate per polar angle for DD2_2D and DD2_2D_no ν at $t \approx 80$ ms.	86
5.12. Snapshots of the instability developing in the density	86
A.1. Distribution of tracers	97

List of Tables

4.1. Nuclear matter properties for all employed EOS tables	44
4.2. Overview of all models and their key results	49
4.3. Masses of the different ejecta components	62
5.1. List of the key features of the axisymmetric accretion disk models	79

1. Introduction

Neutron stars (NSs) are fascinating objects that offer exciting opportunities to gain new insights in various areas of modern physics. They were first theorized by [Baade & Zwicky \(1934\)](#) as the final stage in the life of massive stars. As the most compact class of stellar objects outside of black holes (BHs), the gravity of NSs has to be described by the laws of general relativity (GR). However, unlike BHs, they are mostly made of neutrons. The inside of NSs reaches extreme densities exceeding even the densities of atomic nuclei. This makes them invaluable astrophysical laboratories to study matter under extreme conditions. An important subclass of NSs are the so-called pulsars. These are rapidly spinning and highly magnetized NSs which emit a beam of electromagnetic radiation observable from Earth in regular pulses (hence the name). In 1967, Jocelyn Bell and Antony Hewish discovered a signal of pulsar for the first time and thereby confirmed Baade and Zwicky's hypothesis ([Hewish et al., 1968](#)).

Eight years later, Hulse and Taylor measured a pulsar signal exhibiting systematic variations in the arrival time of the pulses [Hulse & Taylor \(1975\)](#). They deduced that the pulsar was in orbit with another NS. This discovery led to the confirmation of another theoretical prediction: the existence of gravitational waves (GWs), first proposed by Einstein in 1916 ([Einstein, 1916](#)). Gravitational waves carry away energy and angular momentum of the binary partners resulting in a decrease in their orbital period. In 1982, this effect was confirmed by the continuous observation of the Hulse-Taylor binary ([Taylor & Weisberg, 1982](#)).

Gravitational waves cause the fabric of spacetime itself to stretch and squish periodically. The relative displacement of two test masses due to the passage of GWs is very small, making GW detections extremely challenging, even for strong sources. During most of a binary's lifetime, its gravitational radiation is thus too weak to be measurable on earth. However, as two compact objects (e.g., NSs or BHs) spiral ever closer towards each other, their GW luminosity rises and peaks at the moment of the merger. In 2015 – almost 100 years after the theoretical prediction of GWs – the LIGO interferometers directly detected the GW signal from the merger of a binary BH system for the first time ([Abbott et al., 2016](#)). In 2017 following the observation of the GW signal GW170817, originating from a binary neutron star (BNS) merger ([Abbott et al., 2017a,b](#)). By 2017, a third GW observatory, Virgo, was online. This enabled the triangulation of the origin of the signal and led to the observation of multiple electromagnetic transients along with the GW detection ([Andreoni et al., 2017](#); [Arcavi et al., 2017](#); [Coulter et al., 2017](#); [Cowperthwaite et al., 2017](#); [Díaz et al., 2017](#); [Drout et al., 2017](#); [Evans et al., 2017](#); [Hu et al., 2017](#); [Valenti et al., 2017](#); [Kasliwal et al., 2017](#); [Lipunov et al., 2017](#); [Pian et al., 2017](#); [Pozanenko et al., 2018](#); [Smartt et al., 2017](#); [Tanvir et al., 2017](#); [Troja et al., 2017](#); [Utsumi et al., 2017](#)). This is the only detection of a gravitational and electromagnetic signal from the same source to this day and led to a plethora of valuable information for nuclear and astrophysics.

At the end of the inspiral of two BNSs, they collide violently with orbital speeds of roughly 40% the speed of light (see, e.g., [Radice et al., 2020](#)). The two NS fuse into a new massive compact object. For most binary systems, this remnant collapses to a BH either immediately

or after a delay, ranging from a few milliseconds up to a few hours (see, e.g., [Fan et al., 2013](#)). Only very light BNS mergers leave a stable NS behind. As the stars collide, shock waves heat the matter at the collisional interface up to 10^{11} K and the outwards-facing sides of NS become tidally disrupted. The matter expelled from the collision forms an accretion disk surrounding the newly formed central object. Ejected matter can become unbound, on dynamic timescales, due to the mechanisms mentioned above. During later stages, 10 – 30% of the matter in the accretion disk can be unbound by magneto-hydrodynamical (MHD) effects, neutrino interactions, and the recombination of free nucleons. In the ejecta, radioactive isotopes are produced by nuclear reactions. This is called nucleosynthesis. The outcome depends on the hydrodynamical history and initial composition of the ejecta.

Already in 1957, [Burbidge et al. \(1957\)](#) proposed the existence of the so-called rapid neutron-capture process (r process) from the distribution of heavy elements in the solar system. However, the astrophysical site of the r -process was unclear for 60 years. During the r process, nuclei capture neutrons faster than they undergo β -decay, creating very neutron-rich isotopes. The energy set free by the radioactive decay of the newly synthesized nuclei induces a characteristic electromagnetic emission from the ejecta lasting for multiple days, known as kilonova (KN) ([Li & Paczyński, 1998](#); [Kulkarni, 2005](#); [Metzger et al., 2010](#); [Kasen et al., 2013](#); [Tanaka & Hotokezaka, 2013](#); [Rosswog, 2013](#)). In the days following GW170817, the electromagnetic transient AT2017gfo was observed in near-infrared to ultraviolet wavelengths which matched the predictions for a KN. The light curve confirmed the production of r -process elements, and thereby NS mergers as one of the sites of the r process (see, e.g., [Rosswog et al., 2018](#); [Kawaguchi et al., 2018](#)). However, other sources might be responsible for the early r -process enrichment of the galaxy (see, e.g., [Côté et al., 2019](#); [Molero et al., 2021](#)).

At the extreme densities inside NSs, the matter consists mostly of free neutrons and protons. Their mean free path is so short that the strong interaction has a large influence on the thermodynamical properties of the matter. As a result, the high density equation of state (EOS) is highly uncertain and topic of current research (see, e.g., [Lattimer & Prakash, 2016](#)). The dynamics and outcome of BNS mergers depend sensitively on the nuclear EOS because it determines the response of matter to compression (see, e.g., [Janka & Bauswein, 2022](#), for a review on the role of the EOS in BNS mergers). On one hand, this means that a better understanding of the nuclear EOS is critical to understand the role of BNS mergers in the r -process enrichment of galaxies. On the other hand, this makes merger simulations an excellent tool for studying nuclear physics. Hydrodynamical simulations of mergers, which take the EOS as input, predict observables such as the emission of GWs and ejection of matter. Constraints on the EOS can be found, by comparing these predictions with astrophysical observations.

The EOS determines how NSs respond to tidal forces during the late inspiral, leaving a detectable imprint in the GW signal (see, e.g., [Chatziioannou, 2020](#); [Dietrich et al., 2021](#)). This effect was measured in GW170817 and led to important constraints on the EOS (see, e.g., [Abbott et al., 2018](#); [De et al., 2018](#)). After the merger, the newly formed remnant is heavily deformed and rotates rapidly, resulting in further GW emission (see, e.g., [Stergioulas et al., 2011](#); [Bauswein et al., 2012](#); [Takami et al., 2015](#)). Even though this post-merger signal could not be measured in 2017 because it lay outside the frequency range of LIGO and Virgo, future GW observations with third-generation detectors will be able to detect post-merger signals for nearby events ([Chatziioannou et al., 2017](#)). The spectrum of these signals can provide new exciting insights to the EOS at very high densities (see, e.g., [Baiotti, 2019](#)). Besides the GW signal, the observation of AT2017gfo offered additional information about the merger

dynamics, which can be used to infer the properties of the EOS. The evolution of the luminosity and spectrum of KNe depend on the ejecta mass, velocity, spatial distribution, and composition (see, e.g., [Metzger, 2020](#)). The ejecta properties depend on the merger dynamics and thus on the nuclear EOS. Therefore, the observations of electromagnetic transients can be used alongside the detection of GW to constrain the EOS from merger events.

There are numerous EOS models available for use in computational simulations of supernovae and compact object mergers. They are based on various approximate and phenomenological descriptions of the nuclear interaction and, as such, are constructed from fundamentally different sets of parameters. Many studies aim to quantify nuclear physics uncertainties in numerical simulations by employing a selection of different EOS models (see, e.g., [Sekiguchi et al., 2016](#); [Radice et al., 2018](#); [Nedora et al., 2021b](#)), thereby varying many characteristics of the EOS at the same time. However, understanding the role of individual aspects of the nuclear EOS in BNS mergers is difficult, if not impossible, with this approach.

This thesis aims to systematically investigate the influence of the EOS on BNS mergers based on nuclear matter properties. We investigate the dynamical evolution and the GW emission of the merger, as well as the properties of ejected matter, including the post-merger phase.

In the first part of this thesis, we perform multiple general relativistic hydrodynamical simulations of neutron-star mergers, with different EOS models constructed from Skyrme-type interactions ([Lattimer & Swesty, 1991](#); [Schneider et al., 2017](#)). By adjusting the Skyrme parameters, we systematically vary the nuclear matter properties. For each EOS obtained this way, calculate the gravitational wave signal and dynamical ejection of matter from the simulations and relate their properties to the EOS used.

The second part of the thesis is dedicated to the ejection of matter from the accretion disks of BNS mergers on long timescales. The largest part of the ejected matter (see, e.g., [Fujibayashi et al., 2023](#)) stems from the late-time evolution of the accretion disk, taking place over several seconds. Therefore, simulating the entire mass ejection history of a BNS merger is very computationally expensive, especially when multiple models need to be run for parameter studies. The computational expenses can be scaled down by reducing the dimensionality. After the dynamical phase of the merger, the remnant is roughly cylindrically symmetric and can be approximated by a two-dimensional description. Axisymmetric simulations of BH- and NS-accretion disk systems based on artificial initial conditions have been performed in several works (see, e.g., [Fernández & Metzger, 2013](#); [Metzger & Fernández, 2014](#); [Just et al., 2015](#); [Fernández et al., 2020](#); [Just et al., 2021](#)). However, to obtain the full mass ejection history of a BNS merger, both the dynamic and the accretion disk phases need to be consistently simulated. To achieve this, we use initial data based on a previously performed 3D simulation.

The thesis is structured as follows: In Chapter 2, we explain the BNS mergers in more detail and introduce the relevant physical concepts, including the nuclear EOS. Chapter 3 describes the mathematical formulations of general relativity and hydrodynamics used in numerical simulations and gives an overview of the methods used for their solution. The results of the thesis' first part investigating the effect of nuclear matter properties in BNS merger simulations are laid out in Chapter 4. In Chapter 5, we describe our simulation framework for numerical relativity (NR) simulations in axisymmetry using the cartoon method and our method for the creation of two-dimensional initial data of the post-merger system. Furthermore, we present a first test simulation of a BNS-merger remnant. Finally, we summarize our results and give an outlook in Chapter 6.

2. Physical background

2.1. Dynamics of merging neutron stars

Coalescing binary neutron stars (BNSs) are spectacular astrophysical events with far-reaching consequences for the chemical evolution of galaxies and several exciting multi-messenger observables that can give new insights into the fields of nuclear physics, neutrinos, and general relativity. The merger of two orbiting neutron stars (NSs) has multiple phases that are dominated by different physical effects. Figure 2.1 shows a sketch of the possible evolution phases of the remnant and their outcomes. After the inspiral, the binary neutron stars collide

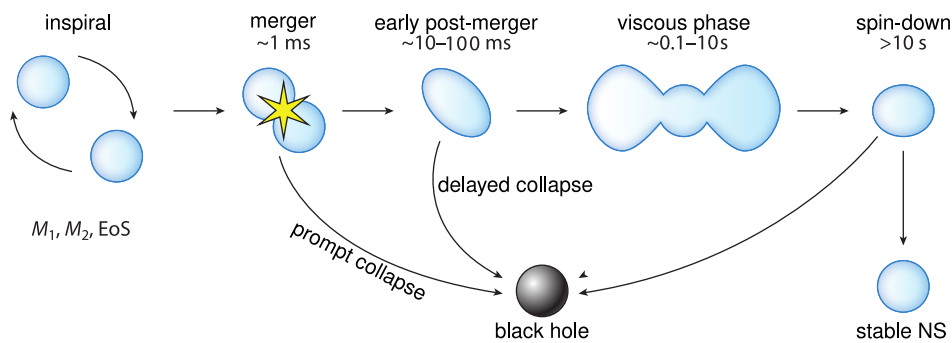


Figure 2.1.: Overview of the different stages during BNS mergers and the possible evolution paths of the remnant. Figure adapted from Radice et al. (2020).

and form a new central object which promptly collapses to a black hole (BH) if it is massive enough. Otherwise, they produce a highly deformed and oscillating massive NS. In this case, tidal torques and shocks originating at the merger interface expel matter that gathers in an accretion disk around the central object. Initially, the dynamics of the post-merger phase are dominated by remnant oscillations and the emission of gravitational waves (GWs). After $\sim 10 - 20 \text{ ms}$, the oscillations and GW emission die down and the dynamics of the disk are driven by the neutrino emission. In the center of the accretion disk remains either a metastable massive NS or a BH if a delayed collapse occurs. After $500 \text{ ms} - 1 \text{ s}$, neutrino cooling becomes ineffective and magneto-hydrodynamically (MHD) induced viscosity dominates the evolution of the accretion disk.

The inspiral and merger dynamics are described in detail Section 2.1.1. Section 2.1.2 explains the different evolutionary paths that the merger remnant can take and finally the evolution of the accretion disk is detailed in Section 2.1.3. This chapter mostly follows Radice et al. (2020); Janka & Bauswein (2022).

2.1.1. Inspiral and merger

A binary system of two massive stars will eventually evolve into a BNS system after both stars undergo supernova explosions. The orbital motion of the NSs leads to the emission of GWs which carries away orbital energy and angular momentum. Consequently, the separation of NSs decreases continuously. This effect was measured for the first time for a binary NS system including pulsar, known as the Hulse-Taylor binary (Hulse & Taylor, 1975). The observed decrease of the orbital period matched the prediction from general relativity exactly which was the first indirect observation of GWs (Taylor & Weisberg, 1982). The orbital motion of BNSs can be approximately treated in the post-Newtonian approximation of general relativity (Blanchet, 2014) or in the effective one-body approach (Buonanno & Damour, 1999). Finite-size effects are not important during most of the binary’s evolution. However, as the NSs’ separation shrinks, their tidal deformation becomes relevant (see Section 2.2.1). Finally, the NSs merge, resulting in a violent collision forming a massive compact object. In 2017, the so-called “chirp signal” (see Section 2.2.1) from the inspiral of two coalescing NSs was measured for the first time with the gravitational wave detectors LIGO and Virgo (Abbott et al., 2017a).

The fate of the resulting remnant depends on various factors (see Section 2.1.2). If the newly formed massive compact object survives the merger and remains a NS, a larger amount of matter is expelled and forms an accretion disk. Shocks heat the matter to $T \sim 100$ MeV at the merger interface. The two cores of the original NSs do not immediately merge due to their angular momentum and the increase in pressure as the maximum density increases. Instead, they start oscillating and only merge slowly while the hot material at the merger interface is redistributed to the outer layers of the remnant. On the timescale of tens of milliseconds, the hot matter forms a ring shape. The maximum temperature typically is reached at densities between $2 - 3 \times 10^{14} \text{ g cm}^{-3}$. Meanwhile, shocks can not penetrate the central region of the massive NS, due to the high sound speed at supra-nuclear densities. Therefore, the core of the massive NS stays comparably cold.

This period is highly sensitive to the nuclear equation of state (EOS). The EOS describes the pressure of the fluid as a function of its density, temperature, and composition and therefore it governs the contraction of the remnant core and its oscillations (see Section 2.4 for more detail). The bounces continue to expel matter from the remnant for up to ~ 100 ms as long as the remnant does not collapse to a BH (Nedora et al., 2019). Initially, the remnant exhibits a strong bar-shaped deformation that is mostly responsible for the emission of GWs. However, a one-sided deformation can develop as the cores merge (Paschalidis et al., 2015). In this case, the remnant develops a “bump” of high density on one side and a region of lower density and higher temperature on the opposite side. How long it takes for this transition to occur is linked to the EOS and can have a large impact on the emission of GWs, the disk mass, and the ejection of matter in the early disk phase. Figure 2.2 shows the remnant 15 ms after the merger for two simulation with identical BNS masses but different EOS. In the simulation shown in the left panel, a bar-shaped deformation of the NS core is visible while in the simulation shown in the right panel, the bar-shaped deformation has been replaced by a one-sided deformation.

2.1.2. Fate of the remnant

As described above, the newly formed remnant can either promptly collapse to a BH or form a metastable massive NS. In the case of a prompt collapse, the BH swallows almost all matter dispelled from the merger. The remaining matter typically collects in an accretion disk with

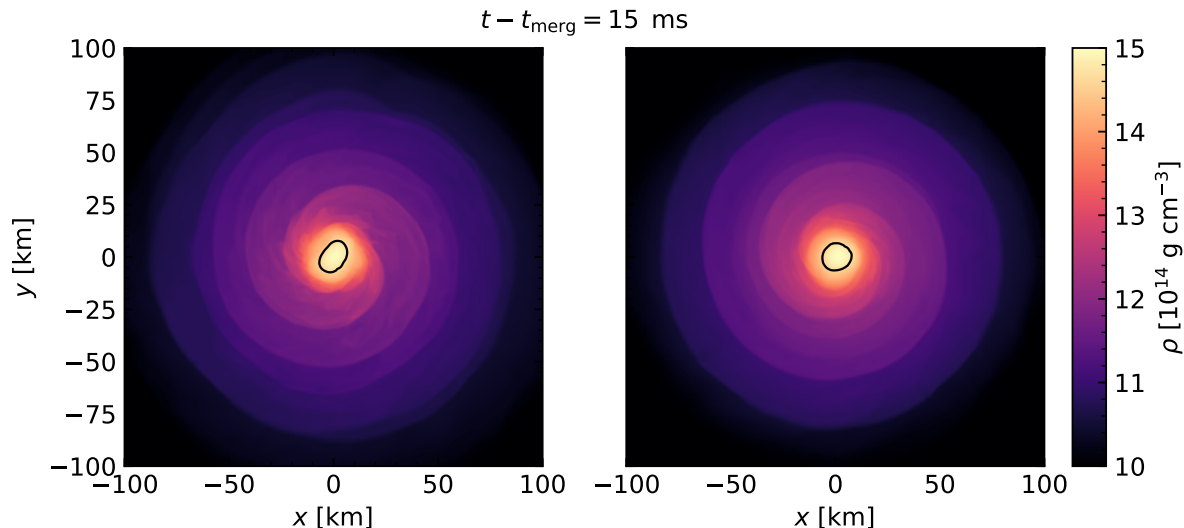


Figure 2.2.: Deformed massive NS in the center of the accretion disk for two different EOS. Shown is the density distribution in the equatorial plane 15 ms after the merger. The black lines show the contours with $\rho = 5 \times 10^{14} \text{ g cm}^{-3}$.

very low mass and the amount of unbound material is negligible. The maximum total mass that does not result in a collapse, the so-called threshold mass, depends on the nuclear EOS. It can be inferred from multi-messenger observations and can thus be used to constrain the EOS, which was done for the event in 2017 by several works (Margalit & Metzger, 2017; Rezzolla et al., 2018; Shibata et al., 2019; Most et al., 2020; Nathanail et al., 2021). A uniformly rotating NS can be $\sim 20\%$ heavier than the maximum mass allowed by the EOS where the upper limit on the rotation is set by the mass-shedding limit of the outer layers of the NS (Paschalidis & Stergioulas, 2017). However, shortly after the merger, the remnant is supported by differential rotation and can thus reach even higher masses. In such cases, the NS core contracts and the remnant collapses to BH on the timescale of a few to tens of milliseconds, as angular momentum and energy are redistributed or lost. In the context of merger remnants, a NS supported by uniform and differential rotation is referred to as supra-massive NS (SMNS) and hyper-massive NS (HMNS), respectively. Which of these three scenarios – prompt collapse, HMNS, or SMNS – happens depends on the total mass, the mass ratio, and the EOS.

2.1.3. Evolution of the accretion-disk

During the first few milliseconds, matter is expelled from the merging NSs by tidal torques and shocks at the merger interface. A large fraction of this matter is still gravitationally bound and therefore stays within $\sim 100 \text{ km}$ of the remnant. If the central newly formed NS is not collapsing promptly after the merger, this matter forms an accretion disk. Oscillations in the NS keep ejecting matter into the disk for several tens of milliseconds after the merger as long as the massive NS does not collapse. The final disk mass depends on the EOS and the mass ratio of the BNS system (see, e.g., Fernández & Metzger, 2016; Radice et al., 2018; Nedora et al., 2021b). Larger mass ratios favor more efficient mass ejection from tidal torques and therefore larger disk masses. The influence of the EOS is not as straightforward. For softer EOS,

the BNSs collide more violently and consequently eject more mass from the contact surface. At the same time, the initial NSs has a smaller tidal deformability and therefore eject more matter due to tidal torques. These two effects are competing and the overall impact of the EOS is not clear and depends on the mass ratio.

The bar-shaped deformation in the center of the newly formed massive NS launches two spiral arms into the disk. This can be seen in the left panel of Fig. 2.2. However, as the bar-shaped deformation disappears a one-armed spiral arm can form (see the right panel). Initially, the two cores of the original BNSs oscillate against each other in the center of the newly formed massive NS, which unbinds matter with each bounce. The ejection of this matter proceeds through the disk due to angular momentum transport in the spiral arms (Nedora et al., 2019). Furthermore, additional matter can be unbound by the spiral arms due to shock heating in the disk. The disk bulk is dominated by cooling due to neutrino emissions and is very close to weak equilibrium. The emitted neutrinos are partially reabsorbed in the region directly above the NS and in the outer layers of the disk leading to net neutrino heating which can unbind a small amount of matter (see, e.g., Perego et al., 2014). If the massive NS collapses to a BH a large fraction ($\gtrsim 50\%$) of the disk is swallowed almost immediately. This results in a drop in the maximum density to $\sim 10^{12} \text{ g cm}^{-3}$. At the same time, the neutrino irradiation is reduced because most of the neutrino emission stems from the hot interface of the NS and the disk. Furthermore, the spiral arms disappear and the disk becomes more axisymmetric. Consequently, the ejection of matter due to neutrino absorption and remnant oscillations stops.

On timescales of $\sim 1 \text{ s}$, the disk evolution is determined by an effective viscosity driven by MHD effects, most importantly, the magneto-rotational instability (MRI) (Balbus & Hawley, 1991). After 10-20 ms, GWs have dampened the bar mode in the NS and neutrino emission becomes the most relevant cooling mechanism. The neutrino emission carries away the internal energy generated by viscous heating. However, due to the transport of angular momentum by the MRI, the disk expands outward and matter falls into the BH. Consequently, the disk temperature drops and neutrino cooling becomes less efficient. After $\sim 1 \text{ s}$ the disk reaches a low enough temperature ($k_{\text{B}}T \lesssim 2 - 3 \text{ MeV}$), the viscous heating outweighs the neutrino cooling, and viscosity-driven mass ejection occurs (Fujibayashi et al., 2018). This effect unbinds 10 – 30% of disk mass.

2.2. Gravitational waves

During the inspiral and early post-merger phase of coalescing NSs, large amounts of energy are emitted by GWs. Figure 2.3 shows a schematic representation of a power-density spectrum together with the corresponding waveform of a GW signal emitted during a BNS merger. The signal continuously evolves towards larger frequencies during the inspiral and undergoes a sudden change at the merger after which the spectrum is dominated by a large peak at even higher frequencies. Each phase of GW emission carries interesting information about the merger dynamics and can be used to constrain the EOS at nuclear and supra-nuclear densities. For an introduction to the mathematical description of GW see Section 3.1.5. The inspiral signal and what can be learned from it is described in Section 2.2.1. Section 2.2.2 details the post-merger GW emission.

2.2.1. Insprial gravitational wave signal

The orbit of binary compact objects, such as NSs and BHs decreases with time due to the emission of GWs. For most of the binary's evolution, it can be approximated as an adiabatic system and treated in the post-Newtonian approximation to general relativity, which is an expansion in the relative velocity $\frac{v}{c} \ll 1$ of the binary partners and thus only valid for large separations. During this phase, the GW frequency is twice the orbital frequency (at leading order). As the orbit shrinks, the orbital velocity and consequently the frequency of the emitted GWs increases (see red line in Fig. 2.3). From the GW signal the chirp mass, defined as

$$\mathcal{M} := \frac{(M_A M_B)^{3/5}}{(M_A + M_B)^{1/5}} \quad (2.1)$$

and the mass ratio $q = \frac{M_A}{M_B}$ can be deduced. The subscripts A and B are referring to the two stars in the binary with $M_A > M_B$, i.e., $q \geq 1$. For the last thousands of orbits, the stars inspiral toward one other, emitting a GW signal that rises in amplitude and frequency until it reaches a maximum named the “chirp” (see the waveform in Fig. 2.3). At merger, the frequency is $\sim 1.5 - 2$ kHz. When the separation of the NS becomes sufficiently small, they become tidally deformed which has a measurable impact on the emission of gravitational waves (see, e.g., Shibata, 2015). The tidal deformability Λ of a NS quantifies the quadrupolar deformation of a star due to the tidal field of its binary companion and has a strong dependence on the EOS (see Section 2.4.3). A larger tidal deformability accelerates the late inspiral and leads to faster orbital velocities. At leading post-Newtonian order this effect is described by the reduced tidal deformability

$$\tilde{\Lambda} = \frac{16}{13} M^{-5} \left[(M_A + 12M_B) M_A^4 \Lambda_A + (M_B + 12M_A) M_B^4 \Lambda_B \right]. \quad (2.2)$$

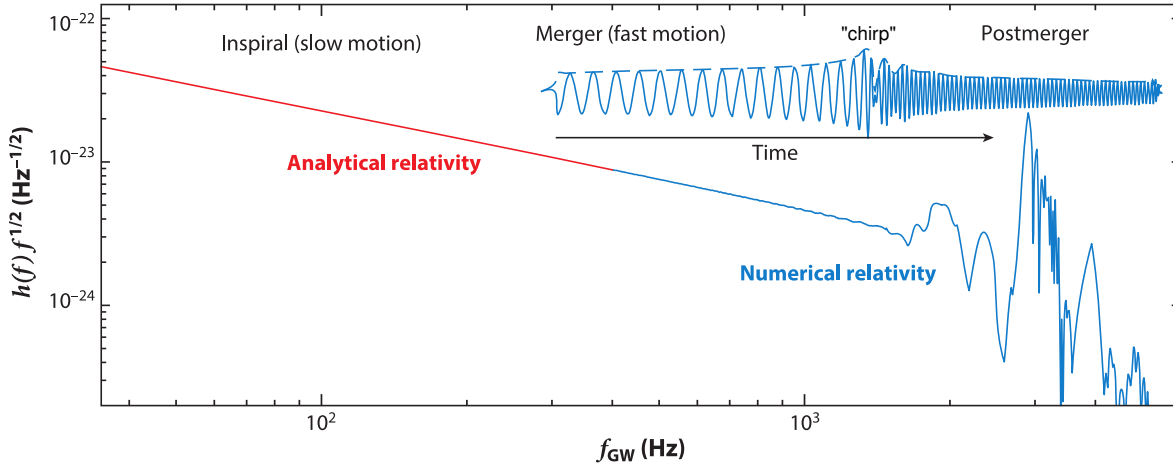


Figure 2.3.: Example of a power-density spectrum of a GW signal emitted during a BNS merger. The inspiral waveform can be analytically described by post-Newtonian methods and the effective one-body approach (red part of the spectrum) while numerical relativity has to be employed to follow the late inspiral, merger, and post-merger signal (shown in blue). The top right corner shows the corresponding waveform of the GW strain. Figure from Radice et al. (2020).

The dimensionless tidal love number $k_2 = \frac{3}{2}C^5\Lambda$ and the tidal coupling constant

$$\kappa_2^T = 3M^{-5} \left[M_B M_A^4 \Lambda_A + M_A M_B^4 \Lambda_B \right] \quad (2.3)$$

are related quantities which are also often used in the literature, where $C = \frac{M}{R}$ is the compactness parameter. For equal mass binaries, κ_2^T and $\tilde{\Lambda}$ are related by $\kappa_2^T = \frac{3}{16}\tilde{\Lambda}$.

From the measurement of the gravitational wave signal GW170817, the chirp mass, the mass ratio, and the reduced tidal deformability of the original BNSs were constrained to be $\mathcal{M} = 1.186(1)M_\odot$, $q \in [1, 1.34]$, and $\tilde{\Lambda} \lesssim 800$, respectively (Abbott et al., 2017a, 2019). The constraints on the tidal parameters are not as tight because they are most sensitive to the GW signal at high frequencies where the signal-to-noise ratio of ground-based GW detectors is lower. These measurements deliver valuable constraints on the EOS and new insights on the origin of r -process elements, especially if combined with the observation of electromagnetic counterparts.

2.2.2. Post-merger gravitational wave signal

After the merger, the violent oscillations of the newly formed remnant continue to emit gravitational waves. The luminosity of the GW signal in the post-merger phase is larger than during the inspiral but it is emitted at higher frequencies ($\gtrsim 1$ kHz), as seen in the spectrum in Fig. 2.3. The sensitivity of ground-based detectors like Ligo and Virgo declines in this frequency range which is why the post-merger signal could not be measured for GW170817. Nonetheless, observations of post-merger GWs might be possible in the near future with third-generation GW telescopes for very nearby events (Chatziioannou et al., 2017).

The post-merger spectrum is typically made up of several oscillation modes. The dominant mode due to the quadrupolar deformation of the remnant produces a pronounced peak at frequencies $\sim 2 - 4$ kHz and is usually called f_2 or f_{peak} . Several works (Stergioulas et al., 2011; Bauswein et al., 2012; Bauswein & Janka, 2012; Hotokezaka et al., 2013a; Takami et al., 2014, 2015; Rezzolla & Takami, 2016; Kiuchi et al., 2020) have found correlations of f_2 and the tidal deformability or $R_{1.6}$, the radius of a cold, non-rotating (TOV) star with a fixed mass of $1.6M_\odot$. A measurement of the f_2 peak could thus provide important constraints on the EOS. Several other modes have been identified in numerical relativity (NR) simulations. While the primary f_2 mode can be active for more than 30 ms, the secondary modes decay after ~ 10 ms. Their origin is still topic of active research but is most likely related to the collision of the NSs (see, e.g., Baiotti, 2019). The f_2 peak, on the other hand, is mostly determined by the orbital frequency of the stars at merger, which is why it depends on the low-density physics of $R_{1.6}$ and $\tilde{\Lambda}$. Apart from the measurement of the peak frequencies in the GW spectrum, valuable information about the fate of the remnant can be obtained from the detection of the post-merger signal. While the ring-down signal after the formation of a BH will be most likely at too high frequencies to be measurable, the presence or absence of a post-merger signal can be used to constrain the threshold mass for prompt collapse, when combined with the mass information from the inspiral phase.

2.3. Ejection of matter

The ejection of matter is one of the most important outcomes of BNS mergers. Throughout the different phases of the merger and post-merger, matter can be ejected which possibly

undergoes various nucleosynthesis processes. We give an overview of the different ejecta mechanisms during the merger and disk phase in Section 2.3.1. So far, BNS mergers are the only observationally confirmed source of r -process elements in the universe. Section 2.3.2 gives an overview of r -process nucleosynthesis and observational constraints. The electromagnetic counterpart, driven by radioactive decay in the ejecta is the most promising observation accompanying future GW observations. In Section 2.3.3, we discuss the kilonova (KN) and how light curves are related to the ejecta properties as well as other counterparts. Sections 2.3.1, 2.3.2, and 2.3.3 are mostly based on Radice et al. (2020); Janka & Bauswein (2022), Cowan et al. (2021), and Fernández & Metzger (2016), respectively.

2.3.1. Ejecta mechanisms

The most crucial parameters for the KN are the total mass, velocity, and composition of the ejected matter (see Section 2.3.3). In the expanding ejecta, heavy elements are synthesized via the r process for which the abundance of free neutrons is crucial. Since the ejecta are charge neutral and initially only consist of protons and neutrons, the electron fraction Y_e is equal to the proton fraction and is often used to quantify the neutron-richness of the ejecta. Thus, the final ejecta composition is mostly dependent on the electron fraction (see Section 2.3.2). Neutron star matter is (like the name suggests) mostly composed of free neutrons. However, weak reactions (electron/positron captures, neutrino absorptions, and β -decays) tend to increase the electron fraction of the initially neutron-rich material.

Neutron-star mergers eject matter due to a variety of mechanisms that operate on different timescales. The ejecta are commonly grouped in dynamical ejecta, which become unbound during the first ~ 10 ms after the merger, and secular ejecta, which are ejected on timescales up to several seconds. However, both dynamic and secular ejecta can be further grouped into multiple components based on their ejection mechanisms which each unbind different amounts of matter with differing compositions. Figure 2.4 displays the different ejecta components and their respective timescale. The mechanisms operating on dynamical timescales can unbind between 10^{-4} and $10^{-2} M_\odot$ with velocities ranging from $v \approx 0.1 - 0.3c$ (see, e.g., Hotokezaka et al., 2013b,a; Radice et al., 2018; Nedora et al., 2021b). Close to the time of the merger, tidal torques disrupt the outer layers of the merging NSs. A part of this matter, commonly called the tidal ejecta, becomes unbound and escapes from the remnant without being exposed to shocks. Therefore, it only experiences relatively low temperatures and weak reactions only have a minor influence and the electron fraction stays below 0.1. In a merger with a large mass ratio, the smaller star is torn apart by the larger one, resulting in more tidal ejecta.

The second component of the dynamical ejecta is the result of direct interactions of colliding NSs. The collision of the NSs launches a shock wave into the surrounding debris which unbinds matter. These ejecta are typically called the shocked or shock-heated ejecta. They reach very high temperatures ($T > 10$ MeV) and thus positron and neutrino captures increase their electron fraction (see Section 2.3.2). This results in a broad distribution of Y_e ranging from 0.1 to 0.5. An accretion disk is formed in the equatorial plane from debris originating from the tidal disruption of the BNSs. The higher densities of the disk bulk shield the expanding unbound matter from neutrino irradiation. Closer to the rotational axis, on the other hand, the density quickly drops and the flux of neutrinos is larger. Therefore, matter expanding in the polar direction is exposed to more intensive neutrino irradiation increasing its electron fraction. As a result, the electron fraction is correlated with the polar angle. This can be seen in Fig. 2.5

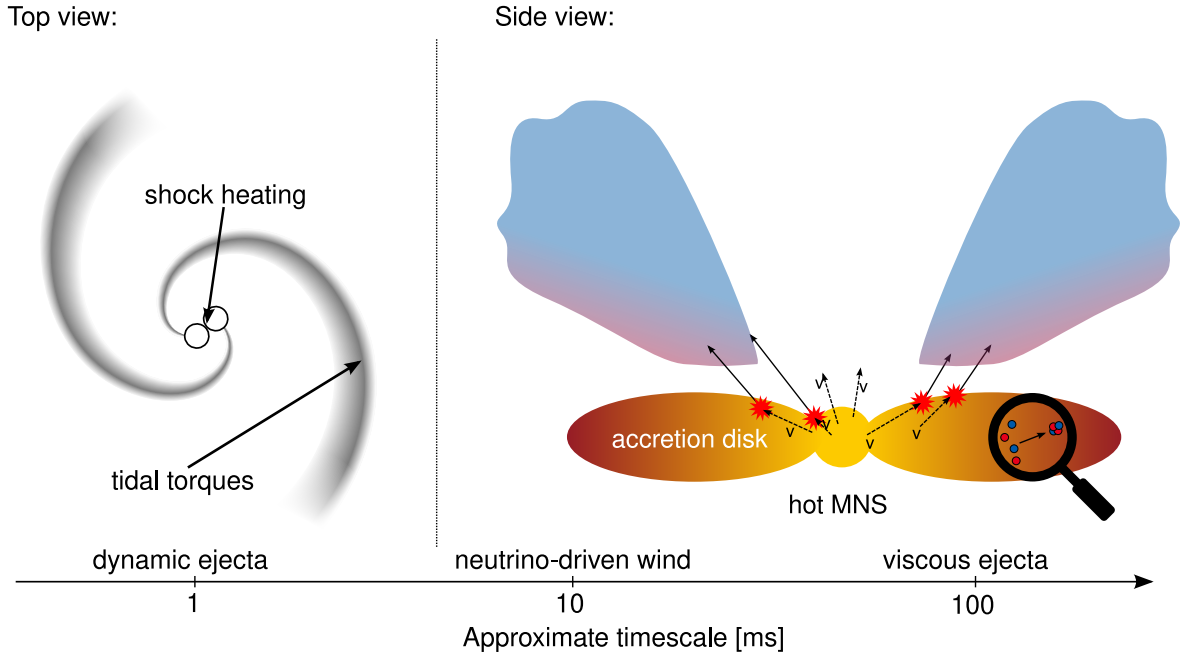


Figure 2.4.: Ejecta components and their respective timescale. On dynamical timescales, tidal torques, and shock heating eject matter from the outer regions of the NSs and the collision interface. In the early post-merger phase, spiral waves and neutrino interactions unbind matter from the remnant. After more than ~ 100 ms, viscous heating in the accretion disk leads to the ejection of 10–30% of the disk on timescales of seconds. Recombination of nucleons into alpha particles provides additional energy that assists in the ejection of matter. Courtesy of Dirk Martin.

which shows the distribution of the electron fraction in a numerical merger simulation 10 ms after the merger.

A small fraction of the shocked ejecta ($\sim 10^{-5} - 10^{-6} M_{\odot}$) can be accelerated to mildly relativistic velocities ($v \gtrsim 0.6c$). Despite its low mass, this matter might produce observable features in the electromagnetic counterpart (see Section 2.3.3).

The dynamical ejecta are followed by the so-called secular ejecta. During the early disk phase (~ 10 -100 ms after the merger) the newly-formed massive NS exhibits an oscillating double core structure. As the remnant reaches minimum compactness during the oscillation matter becomes unbound. This launches spiral waves into the accretion disk which transport angular momentum and heat the disk (Nedora et al., 2019, 2021b). This component is sometimes called the spiral wave wind. It is occasionally attributed to the dynamical ejecta because they have a similar origin and properties but the ejection of matter due to the bounces of the central NS can continue for up to ~ 100 ms and eject up to $\sim 10^{-2} M_{\odot}$ as long as no BH is formed. These ejecta typically have velocities between $0.1 - 0.2c$ and their electron fraction distribution usually shows a peak at $Y_e \approx 0.3$ (Nedora et al., 2019, 2021b). A word of caution is in order regarding the spiral wave wind because it was so far only found in simulations with the WhiskyTHC code which might artificially enhance the neutrino heating above the disk. In the first few tens of milliseconds, neutrinos are emitted in vast amounts and partially reabsorbed in outer layers

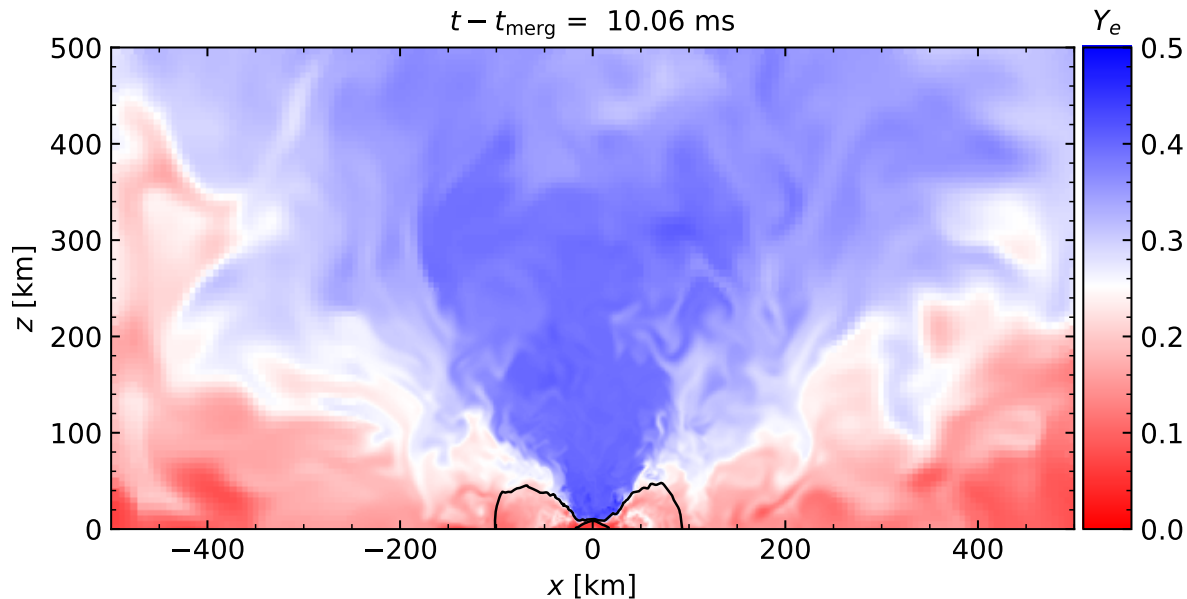


Figure 2.5.: Distribution of the electron fraction in the xz plane of a numerical merger simulation ~ 10 ms after the merger. The electron fraction Y_e of the dynamically ejected material is correlated with the polar angle. Black contours roughly mark the locations of the disk and the central massive NS.

of massive NS and disk, especially close to the poles. This drives an outflow of material with comparably high electron fractions ($Y_e \gtrsim 0.35$) and low mass ($10^{-4} - 10^{-3} M_\odot$). While this neutrino-driven wind is often mentioned as a separate ejecta component, it is usually hard to separate from the other components ejected on similar timescales. Instead, the importance of neutrino heating for the ejection of matter increases with larger polar angles, which is why we simply refer to the mass ejected due to oscillations of the remnant, and neutrino absorption as “early disk ejecta”.

The largest contribution to the ejecta mass becomes unbound on the timescales of seconds (see, e.g., [Fernández & Metzger, 2013](#); [Metzger & Fernández, 2014](#); [Just et al., 2015](#); [Fujibayashi et al., 2020a, 2023](#)). The MRI results in an effective viscosity which transports angular momentum outwards and generates heat in the disk through the dissipation of kinetic energy ([Fernández & Metzger, 2013](#); [Metzger & Fernández, 2014](#); [Just et al., 2015, 2021](#); [Siegel & Metzger, 2018](#); [Fujibayashi et al., 2020a,b,c, 2023](#); [Hayashi et al., 2022](#); [Fahlman & Fernández, 2022](#); [Kiuchi et al., 2022](#)). Furthermore, the recombination of nucleons into alpha particles and heavier nuclei contributes an additional source of heating at late times ([Fernández & Metzger, 2013](#); [Siegel & Metzger, 2017, 2018](#)). Eventually, as the accretion rate drops and neutrino cooling becomes inefficient the disk expands and becomes partially unbound. This is usually referred to as the viscous or viscosity-driven ejection mechanism and can eject matter for up to 10 s ([Fujibayashi et al., 2023](#)). As the disk expands, nucleons recombine to α particles which can enhance the heating in the disk on similar timescales. The velocity of the viscous ejecta is comparably slow $v \approx 0.1c$. Their electron fraction is determined by a competition of the expansion, electron/positron capture, and neutrino absorption timescales and typically lies

between 0.25 – 0.5 (see, e.g., Fujibayashi et al., 2020c; Just et al., 2021). If a BH is formed before the start of the viscous disk phase, the mass of the secular ejecta is similar to that of the dynamic ejecta but if the central NS remains stable, the viscous ejecta are substantially more massive by up to two orders of magnitude (Fujibayashi et al., 2023).

2.3.2. r -process nucleosynthesis

Elements heavier than iron are predominantly synthesized by neutron-capture reactions because charged-particle reaction cross-sections become very small due to the coulomb repulsion of heavier nuclei. As nuclei capture neutrons, they become unstable and decay via β -decays. The combination of β -decays and neutron captures eventually builds up heavy elements. In the abundance distribution of elements heavier than iron in the solar system, a series of three double peaks can be found (see Fig. 2.6). The double-peak structure is caused by the existence

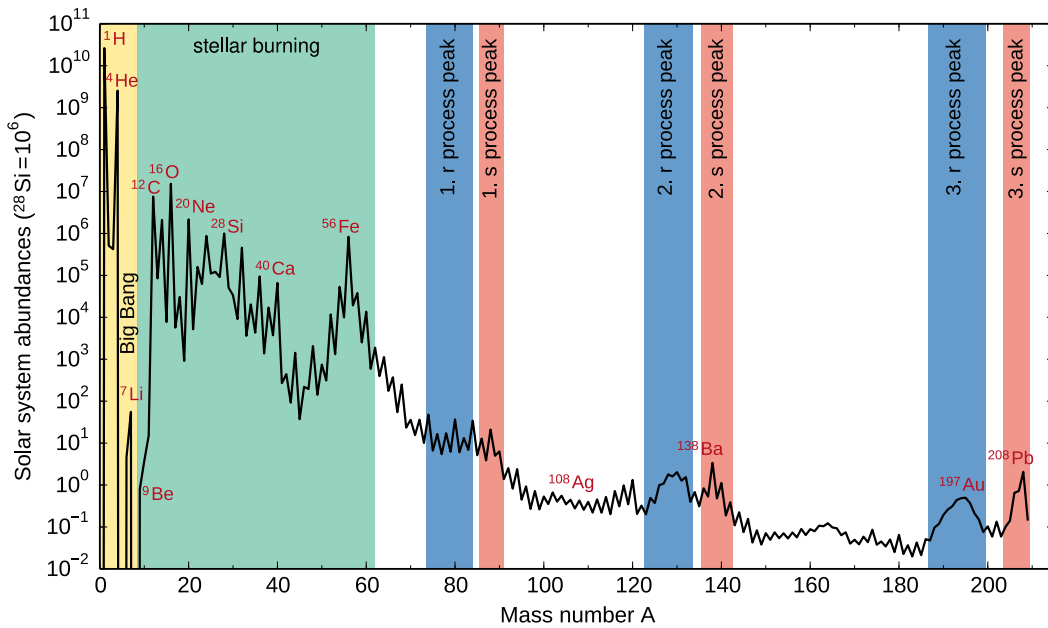


Figure 2.6.: Atomic abundance pattern of the solar system. Color-shaded regions mark the nucleosynthesis process that is responsible for the production of the majority in the respective mass number range. Light elements up to iron are made in the primordial nucleosynthesis and stellar burning. The double-peak structures in the remaining heavy elements hint towards the production of heavy elements by two separate nucleosynthesis processes, the r and s processes. Courtesy of Julia Bliss.

of two different neutron-capture processes (Burbidge et al., 1957), the rapid and the slow neutron-capture process (r and s process), each responsible for the production of roughly half the heavy elements in the universe. Both processes create heavy elements by a combination of neutron captures and β -decays. However, in the r process the neutron-capture timescale is much faster than the β -decay timescale ($\tau_n \ll \tau_\beta$) while the opposite is true for the s process ($\tau_n \gg \tau_\beta$). Figure 2.7 shows a sketch of the nucleosynthesis paths of the r and s processes. During the s process each time a neutron is captured it is followed by a β decay so the nucleosynthesis runs along the valley of stability. The r process involves very neutron-rich

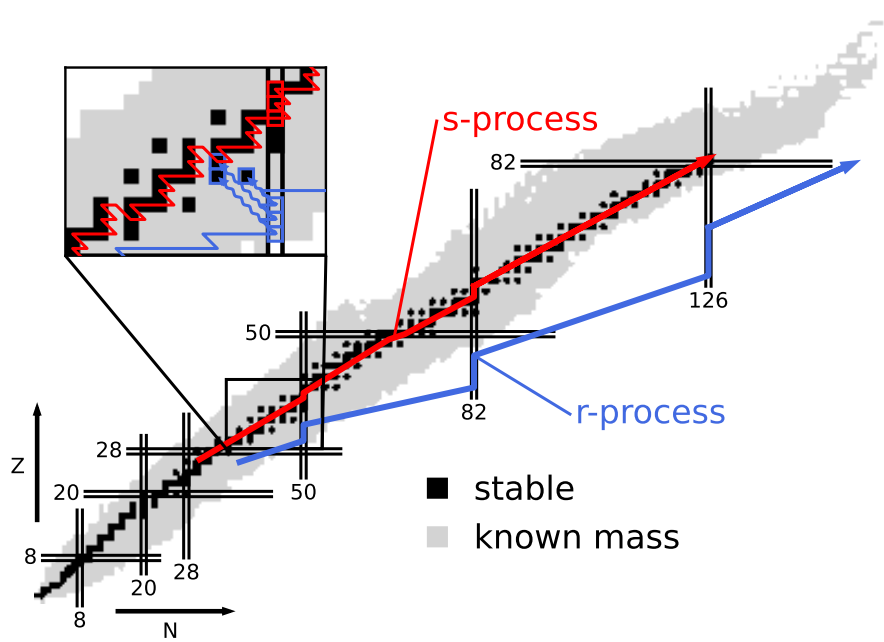


Figure 2.7.: Sketch of the nucleosynthesis paths of the r and s processes. Black and gray squares mark stable nuclei and isotopes with measured masses (Wang et al., 2017), respectively. The inset in the top-left corner shows how the different paths of the two processes result in two separate abundance peaks.

isotopes close to the neutron drip line because nuclei capture multiple neutrons before a β decay occurs. After the neutron captures freeze out, the nuclei decay to stability. Nuclei with closed neutron shells (at $N = 50, 82$, and 126) have larger binding energies compared to isotopes close to them in the nuclear chart. Consequently, they are more abundant during the nucleosynthesis (marked by colored squares in the inset in Fig. 2.7). Due to the different paths of the s and r process, this accumulation of matter occurs at different mass numbers and therefore forms two separate peaks in Fig. 2.6. Spectra of several metal-poor (metal-poor indicates old) stars show an abundance pattern, that matches the r -process abundances in the solar system (Snedden et al., 2008). However, the lighter trans-iron elements in these r process enhanced stars show a star-to-star scatter, indicating some variance in the production site or a separate production site that only produces a limited r process (see, e.g., Travaglio et al., 2004; Hansen et al., 2014).

The s process requires relatively low neutron densities ($n_n \approx 10^8 \text{ cm}^{-3}$) (Busso et al., 1999) over an extended period and is believed to take place in asymptotic giant branch stars (see, e.g., Käppeler et al., 2011). It is relatively well understood since it involves nuclei close to stability with well-known properties. The r process takes place in explosive environments with extremely high neutron densities ($n_n \approx 10^{24} - 10^{28} \text{ cm}^{-3}$) and involves exotic nuclei with unknown properties, far away from isotopes with measured masses (shown as gray squares in Fig. 2.7). Until 2017, it was unclear which astrophysical site provides these extreme conditions, but the spectral evolution of the KN AT2017gfo revealed the presence of lanthanides in the ejecta of a BNS merger (see Section 2.3.3), thereby confirming BNS mergers as one of the sites of the r process. However, the detection of r -process elements in the spectra of metal-poor

stars hints towards other sources that might have contributed to the r -process enrichment in the early galaxy (see, e.g., Côté et al., 2019; Molero et al., 2021).

The r process starts with the formation of seed nuclei with $A \lesssim 60$, predominantly by α -capture reactions and neutron captures for very low electron fractions. As the ejecta expand, their density and temperature drop, leading to the freeze-out of charged particle reactions. Below 3 GK, the mass numbers of seed nuclei are primarily raised by neutron captures. The efficiency of this process is determined by the ratio of neutrons to seed nuclei n_S . The production of lanthanides requires $n_S \gtrsim 50$ to be produced, while actinides require $n_S \gtrsim 150$. A large neutron-to-seed ratio can be reached either by high entropies (“hot” r process) or low electron fractions (“cold” r process) (Freiburghaus et al., 1999; Arcones & Martínez-Pinedo, 2011). In high entropy conditions, the triple- α reaction ($\alpha + \alpha + \alpha \rightarrow {}^{12}\text{C} + \gamma$) which forms the starting point of the seed nuclei production is inefficient, leading to a lower seed abundance and thus higher n_S . However, all ejecta from BNS mergers have low entropies ($\lesssim 30k_B/\text{baryon}$) (see, e.g., Radice et al., 2020). In this case, the nucleosynthesis outcome is mostly determined by the electron fraction of the ejected material. Low electron fractions limit the formation of α particles due to the lack of free protons. If $Y_e \lesssim 0.2$, heavy r -process nuclei with a solar-system-like pattern (including lanthanides) are synthesized. However, if $Y_e \gtrsim 0.3$, only a lighter r -process nuclei with a small fraction of lanthanides are created. The transition between the two scenarios is very sharp and lies approximately at $Y_e = 0.25$.

The electron fraction in the ejecta of BNS mergers is mostly determined by weak reactions, depending on the fluid elements’ trajectory and hydrodynamical history. Most of the fluid elements unbound during and after the merger stem from the inner crust region of the initial NSs which features densities around $10^{14} \text{ g cm}^{-3}$. Their electron fraction is set by the neutrino-less beta equilibrium which lies close to $Y_e \approx 0.05$ at these densities. Due to the high temperatures reached in the merger remnant, large amounts of electron-positron pairs are created and subsequently captured by nucleons. Furthermore, vast amounts of electron and electron antineutrinos are emitted from the remnant and partially reabsorbed by the expanding matter. Since neutrons are much more abundant, positrons and electron antineutrinos are more frequently captured than their respective antiparticles. Consequently, the electron fraction evolves towards more proton-rich compositions and might even become larger than $Y_e = 0.5$. For a detailed analysis of the electron fraction in NS merger ejecta, see, e.g., Just et al. (2021).

2.3.3. Kilonovae

The decay of the unstable heavy elements synthesized in the r process heats the escaping matter as it escapes. This drives an electromagnetic transient with a characteristic light curve. However, the radiation can not escape immediately from the ejecta because initially scattering and absorption processes trap photons within the expanding material making it opaque to electromagnetic radiation. The opacity κ of the material relates the photons mean free path λ to the density of the ejecta via $\lambda = (\rho\kappa)^{-1}$ and depends on the composition of the ejecta and the temperature. As the matter expands, its density and temperature drop until photons can eventually escape. A simple model based on a spherically symmetric ejecta component with mass M , velocity v , opacity κ , in homologous expansion can be used to estimate the key features of the electromagnetic transient (Metzger et al., 2010; Fernández & Metzger, 2016):

The peak time can be estimated by the diffusion timescale which is given by

$$\tau_{\text{diff}} \approx \frac{\rho \kappa R^2}{3c} \approx \frac{\rho \kappa (vt)^2}{3c}, \quad (2.4)$$

with the radius $R = vt$ and the density $\rho \approx \frac{3M}{4\pi R^3} \approx \frac{3M}{4\pi (vt)^3}$. This results in

$$t_{\text{peak}} \approx \left(\frac{M \kappa}{4\pi c v} \right)^{1/2} \approx 2.7 \text{ d} \left(\frac{M}{10^{-2} M_{\odot}} \right)^{1/2} \left(\frac{\kappa}{1 \text{ cm}^2 \text{ g}^{-1}} \right)^{1/2} \left(\frac{v}{0.1c} \right)^{-1/2}. \quad (2.5)$$

Intuitively, slower expanding, more massive ejecta and more opaque ejecta become transparent later. For typical masses and velocities, the KN light curve peaks around 1-10 days, depending on the opacity. The heating rate due to the decay of r -process nuclei can be estimated by $\dot{\epsilon} \approx \epsilon 10^{10} (t/\text{d})^{-1.3}$ and is relatively independent of the electron fraction (Metzger et al., 2010). The thermalization efficiency $\epsilon < 1$ accounts for energy lost due to escaping γ rays and neutrinos (see, e.g., Barnes et al., 2016). After the peak time, the luminosity is approximately given by the total energy deposition rate $L(t) \approx M \dot{\epsilon}(t)$. With this, the peak luminosity can be estimated by

$$L_{\text{peak}} \approx M \dot{\epsilon}(t_{\text{peak}}) \approx 10^{41} \text{ ergs}^{-1} \epsilon \left(\frac{M}{10^{-2} M_{\odot}} \right)^{0.35} \left(\frac{\kappa}{1 \text{ cm}^2 \text{ g}^{-1}} \right)^{-0.65} \left(\frac{v}{0.1c} \right)^{0.65}. \quad (2.6)$$

Due to the peak luminosity being roughly 3 orders of magnitude above typical luminosities of Novae, Metzger et al. (2010) coined the term kilonova. The effective peak temperature is given by the Stefan-Boltzmann law

$$T_{\text{peak}} \approx \left(\frac{L_{\text{peak}}}{\sigma R_{\text{peak}}^2} \right)^{1/4} \approx 3460 \text{ K} \epsilon^{1/4} \left(\frac{M}{10^{-2} M_{\odot}} \right)^{-0.17} \left(\frac{\kappa}{1 \text{ cm}^2 \text{ g}^{-1}} \right)^{-0.41} \left(\frac{v}{0.1c} \right)^{-0.09}, \quad (2.7)$$

where σ is the Stefan-Boltzmann constant. Equations (2.5) to (2.7) show, that the opacity of the ejecta plays a critical role in the KN light curve and spectrum. The opacity of the ejecta originates from a combination of a large number of Doppler-broadened atomic transitions which are not well known individually (see, e.g., Tanaka et al., 2018). The exact opacity and its dependence on the composition can therefore only be modeled approximately. However, it is generally accepted that the presence of lanthanides or actinides in the ejecta leads to orders of magnitude higher opacity due to the high line density of atoms with open f-shells. Thus, the opacity of the ejecta is high ($\kappa \gtrsim 10 - 100 \text{ cm}^2 \text{ g}^{-1}$) when full r -process nucleosynthesis has occurred, yielding a pattern similar to the r -process abundances observed in the solar system or in metal-poor stars. If instead only a weak r -process, which stops around the second peak, develops, the opacity is dominated by open d-shell nuclei and is closer to $\kappa \approx 1 \text{ cm}^2 \text{ g}^{-1}$. Consequently, the corresponding KN peaks within a day and is bright and blue. In contrast, if lanthanides are present the emission is shifted to the near-infrared and peaks later and dimmer.

The emission of AT2017gfo reached peak brightness ($\sim 10^{42} \text{ ergs}^{-1}$) in the visible spectrum within the first day. On the timescale of ~ 10 days, the bolometric luminosity¹ dropped to $\sim 10^{40} \text{ ergs}^{-1}$ with the a power-law scaling indicating radioactive decays ($\sim t^{-1.3}$) while

¹A body's bolometric luminosity is its total frequency integrated energy output per unit time.

simultaneously shifting towards near-infrared wavelengths (Smartt et al., 2017; Cowperthwaite et al., 2017). More complicated models that take into account multiple ejecta components with different properties and spatial distributions have been used to infer the ejecta properties from AT2017gfo with varying results (see, e.g., Villar et al., 2017; Perego et al., 2017; Waxman et al., 2018; Metzger, 2020; Nakar, 2020; Hotokezaka & Nakar, 2020). Most of them obtain the best fit by including at least two components: a fast “blue” (i.e., low lanthanide fraction) component, and a slower “red” (i.e., including lanthanides) component. These predictions do not line up with ejecta properties, extracted from numerical simulations (see, e.g., Siegel, 2019; Nedora et al., 2021b), which typically predict fast, low- Y_e (i.e., high lanthanide fraction) dynamical ejecta and slower moving secular ejecta with higher Y_e .

The spectral evolution of AT2017gfo was captured at different times after the merger, spanning from the near-infrared to the ultraviolet (see, e.g., Pian et al., 2017). During the first couple of days, the spectrum resembled a black body with only a few absorption features discernible. Watson et al. (2019) showed that an absorption feature at ~ 800 nm originates most likely from the absorption lines of Strontium. In the later phases, the spectra are dominated by absorption features and hints towards the existence of Lanthanum and Cerium (Domoto et al., 2022).

Alongside the KN, a short γ -ray burst (sGRB) was detected with a delay of 1.7 s (Abbott et al., 2017b). Short γ -ray bursts are emitted from powerful, narrowly collimated, relativistic jets, driven by magnetic fields and possibly aided by neutrino annihilation (see, e.g., Nakar, 2020). The jet is launched from BNS remnants, either by an BH-torus system (Blandford & Znajek, 1977; Ruiz et al., 2016) or a magnetized NS (Zhang & Mészáros, 2001; Fan et al., 2013; Lasky et al., 2014). The interaction of the jet with the previously launched KN ejecta drives shocks, producing intense forward-beamed gamma-ray emission, visible as sGRB on Earth if it lies in the beam direction. The weak nature of the sGRB observed in 2017 led to the conclusion, that it was observed off-axis (Xie et al., 2018; Lazzati et al., 2018). On longer timescales (weeks to years), the jet and the KN ejecta interact with the interstellar medium (ISM) resulting in an afterglow in the radio to X-ray (see, e.g., Piran et al., 2013; Nakar, 2020). Metzger et al. (2015) pointed out that if even a small fraction of free neutrons survive the r -process nucleosynthesis, their decay would significantly alter the electromagnetic transient during the first hours after the merger. This could be the case for a very small ejecta component with velocities of $\gtrsim 0.6c$, which is present in the dynamical ejecta in many simulations (see, e.g., Dean et al., 2021, and references therein). However, the low mass of the fast ejecta makes them hard to resolve due to the finite resolution of numerical simulations. Interactions of these fast ejecta with the ISM are also a possible explanation of the rebrightening of the KN X-ray afterglow ~ 900 d after the merger (Troja et al., 2020; Nedora et al., 2021a).

2.4. The nuclear equation of state

The mathematical description of the fluid dynamics in BNS mergers is mostly given by conservation laws (see Section 3.2). However, an extra equation relating the pressure to the density of the fluid is needed to close the system of equations. This is the EOS, which describes how matter responds to compression, usually in the form of an equation for the pressure as a function of the fluid’s density, thermal energy, and composition. It is determined by the interactions of the particle constituents of the fluid. Therefore, the EOS connects the microphysics of the strong, weak, and electromagnetic interactions with the macrophysics of hydrodynamics and

general relativity. Section 2.4.1 gives an overview of the statistical-mechanics basics of EOS models and is based on Huang (1987). In Section 2.4.2, we summarize the ingredients of EOS for astrophysical applications. The high density EOS is highly uncertain, so some form of parametrization of its properties is needed to compare different models. We outline two classes of parameters in Section 2.4.3: properties of isolated cold NSs and nuclear matter properties. Finally, we give an overview of two commonly used models for the calculation of uniform nuclear matter in Section 2.4.4.

2.4.1. Statistical mechanics basics

The macrophysical description of a system is given by thermodynamical variables, such as the temperature T or the pressure P . Their relations can be derived from thermodynamic potentials, (i.e., the internal energy U as a function of the entropy S , volume V , and particle number N). In the context of merging NSs simulations it is usually more convenient to express the thermal state of a system in terms of the temperature, not the entropy. The appropriate thermodynamical potential is therefore the free energy $F(T, V, N)$ which is given by a Legendre transformation of the internal energy

$$F = U - TS. \quad (2.8)$$

The microphysical interactions are described by quantum mechanics and are determined by the systems Hamiltonian H . The statistical properties of a system described by H can be expressed by the partition function

$$Z = \text{Tr} \left(\exp \left(-\frac{H}{k_B T} \right) \right), \quad (2.9)$$

where k_B is Boltzmann's constant and Tr denotes the trace. The free energy is then given by

$$F = -k_B T \ln(Z). \quad (2.10)$$

Once the free energy is known, other thermodynamic quantities, such as the pressure P , entropy S , and the chemical potentials μ_i can be derived from its derivatives.

2.4.2. Equations of state for astrophysical applications

In the context of astrophysical hydrodynamical simulations, the thermodynamic state of the fluid is evolved locally, so it is necessary to express all relevant thermodynamic quantities in an intensive way. This includes the internal energy density $\epsilon = U/V$ or specific internal energy $\varepsilon = \epsilon/\rho$ and the entropy per baryon $s = S/N$. The rest mass of the astrophysical fluid is almost exclusively determined by its baryonic constituents (protons and neutrons) which can be bound in nuclei. The baryonic rest-mass density is given by $\rho = mn$, where $n = \frac{(N_p + N_n)}{V}$ is the baryon particle density and m a constant reference mass, called mass factor. Since neutrons and protons have slightly different masses the mass factor should in principle be composition dependent. Instead, the mass difference is usually included in the energy density (see, e.g., Section 2.4.4) and the mass factor is kept constant. Note that different codes might use different mass factors, e.g., the average nucleon mass or the atomic mass unit. For hydrodynamical simulations, it is only important, that the same mass factor is used consistently throughout the simulation and analysis. The number density of a specific particle species n_i is related to its abundance $Y_i = n_i/n$.

The cores of NSs are mostly composed of free neutrons and protons due to the high densities $\rho \gtrsim 10^{14} \text{ g cm}^{-3}$ (although the occurrence of hyperons (see, e.g., Tolos & Fabbietti, 2020) and deconfined quark matter has been theorized (see, e.g., Blaschke & Chamel, 2018; Alford et al., 2019)). In this regime, the EOS is governed by the strong interaction and highly uncertain (see Section 2.4.3). Due to the charge neutrality of the interstellar medium, the abundance of protons (including those bound in nuclei) is equal to the electron fraction Y_e , i.e.

$$n_p = Y_e n, \quad (2.11)$$

$$n_n = (1 - Y_e)n. \quad (2.12)$$

In BNS mergers, weak reactions (electron/positron captures, neutrino absorptions, and β -decays) change Y_e and are thus crucial in determining the chemical composition. However, due to the very small interaction cross sections of neutrinos, they fall out of thermal equilibrium in the outer layers of the remnant NS and thus need to be treated separately from the EOS by a radiation transport model (see Section 3.3).

At densities below $\sim 10^{14} \text{ g cm}^{-3}$, nucleons start to form structures and recombine into nuclei. A possible way to account for this is in the single nucleus approximation (SNA), which assumes that these structures can be represented approximately by a representative nucleus. In the SNA the free-energy contribution of the representative nuclei is described by a liquid-drop model and made up of a bulk energy (e.g. calculated with a density functional, see Section 2.4.4), a surface term, and a coulomb contribution which depend on the nucleus' density, volume, and proton fraction. By minimizing the total free energy, in terms of the free parameters, the nucleus' properties are determined. At lower densities, the approximation of the SNA starts to break down, because an ensemble of nuclei appears. The abundances of the nuclei can be approximated by the statistical equilibrium of nuclear reactions, called nuclear statistical equilibrium (NSE). In NSE, the chemical potential of an isotope i with charge and mass numbers Z and A is determined by the chemical potentials of protons and neutrons $\mu_{n,p}$:

$$\mu_i = Z\mu_p + (A - Z)\mu_n. \quad (2.13)$$

While NSE, describes the contribution of bound nuclei at low densities in a more sophisticated way, the SNA captures changes in the shape and composition of the nucleus and interactions between the nucleus and its surrounding medium of lower density. For temperatures below $T \lesssim 0.5 \text{ MeV}$, a fluid element falls out of NSE, and a nuclear reaction network is needed to track its composition accurately. While reaction networks are crucial to determine the contribution of BNS mergers to the chemical evolution of galaxies and to predict the electromagnetic counterpart of the event, the assumption of NSE is usually sufficient for the modeling of the merger dynamics.

Unlike neutrinos, electrons, positrons, and photons can be assumed to be in thermodynamic equilibrium with the baryonic matter during the merger and post-merger phases of merging BNSs. Electrons and positrons are usually treated as ideal Fermi gas and their contribution to the total pressure, energy, and entropy can be calculated by evaluating Fermi integrals (see, e.g., Lattimer & Swesty, 1991). The contribution of photons can be modeled by a simple blackbody emission and calculated analytically. See, e.g., Timmes & Arnett (1999) for more details on non-baryonic contributions to the EOS

2.4.3. Characterizing the high-density equation of state

The densities inside NSs can reach up to $10^{15} \text{ g cm}^{-3}$. Under these extreme conditions, we assume that matter consists of free neutrons, protons, and electrons. These states are referred to as uniform and non-uniform nuclear matter, respectively. Because of the nucleons' small mean free paths, the strong interaction has a significant influence on the EOS of uniform nuclear matter. However, an exact ab-initio description, especially at very high densities ($\rho \gtrsim 5 \times 10^{14} \text{ g cm}^{-3}$), is currently not possible due to the strong nature of nuclear interactions. Chiral effective field theory (EFT) offers a good description of nuclear matter at intermediate densities ($\rho \lesssim 5 \times 10^{14} \text{ g cm}^{-3}$), but the error estimates of calculations in chiral EFT become very large at densities above $\sim 3 - 5 \times 10^{14} \text{ g cm}^{-3}$ (see, e.g., [Hammer et al., 2020](#)). Furthermore, solving the nuclear many-body problem at the relevant finite temperatures and isospin asymmetries requires a large amount of computational resources and has only been achieved recently ([Carbone & Schwenk, 2019](#); [Keller et al., 2021, 2023](#)). In the absence of ab-initio descriptions, astrophysical applications rely on phenomenological models, such as Skyrme-type interactions (see, e.g., [Lattimer & Swesty, 1991](#); [Schneider et al., 2017](#)) or the relativistic mean-field approximation (see, e.g., [Shen et al., 1998a](#); [Steiner et al., 2013](#); [Banik et al., 2014](#)).

The stellar properties of isolated non-rotating NSs (e.g., its radius or tidal deformability) are often used to characterize an EOS in a model-independent way. Since NSs are extremely dense, their gravitational potential has to be described by general relativity. Their stellar structure is described by the Tolman–Oppenheimer–Volkoff (TOV) equations ([Oppenheimer & Volkoff, 1939](#)):

$$\frac{dP}{dr} = -\frac{M\epsilon}{r^2} \left(1 + \frac{P}{\epsilon}\right) \left(1 + \frac{4\pi r^3 P}{M}\right) \left(1 - \frac{2M}{r}\right)^{-1}, \quad (2.14)$$

$$\frac{dM}{dr} = 4\pi r^2 \epsilon, \quad (2.15)$$

for the pressure P and enclosed mass M at radius r . TOV stars are cold, and their composition is determined by neutrinoless weak equilibrium. Therefore, the EOS reduces to a simple function of one argument, for example, the energy density as a function of pressure. Integrating Eqs. (2.14) and (2.15) with a specific initial condition (e.g. the central pressure) from the center of the NS up to its surface yields its pressure and density profiles, as well as its radius R and total mass $M(R)$. By varying the initial condition one obtains a relation between the mass and radius of cold NSs that always exhibits a maximum mass (see, e.g., [Fig. 4.3](#)). Both, the density profile of a single star as well as the mass-radius relation are uniquely correlated to the EOS (up to the maximum density in the NSs). The tidal deformability of a NS (see [Section 2.2](#)) is obtained by solving the following equation ([Hinderer, 2008](#))

$$\begin{aligned} r \frac{dy}{dr} = & -y^2 - y \left[\frac{r - 4\pi r^3(\epsilon - P)}{r - 2M} \right] \\ & - \frac{4\pi r}{r - 2M} \left[\left(5\epsilon + 9P + \frac{(\epsilon + P)}{c_s^2} \right) r^2 - \frac{6}{4\pi} \right] \\ & + 4 \left[\frac{M + 4\pi r^3 P}{r - 2M} \right]^2, \end{aligned} \quad (2.16)$$

for the quantity y along side Eqs. (2.14) and (2.15). y is an auxiliary parameter related to the gravitational field and c_s is the speed of sound given by $c_s^2 = \frac{dP}{d\epsilon}$. The tidal deformability can

then be obtained by evaluating the following expression:

$$\begin{aligned} \Lambda = & \frac{16}{15}(1 - 2C)^2[2 + 2C(y - 1) - y] \times \\ & \{2C(6 - 3y + 3C(5y - 8)) \\ & + 4C^3[13 - 11y + C(3y - 2) + 2C^2(1 + y)] \\ & + 3(1 - 2C)^2[2 - y + 2C(y - 1)] \log(1 - 2C)\}^{-1}, \end{aligned} \quad (2.17)$$

with the compactness parameter $C = M(R)/R$ and $y = y(R)$.

Astrophysical observations have delivered several constraints on the properties of TOV stars. The observations of heavy pulsars (Antoniadis et al., 2013; Arzoumanian et al., 2018; Fonseca et al., 2021) have put lower limits on the maximum NS mass and information obtained from X-ray pulse-profile modeling of the pulsars PSR J0030+0451 and PSR J0740+6620 (Miller et al., 2019, 2021; Riley et al., 2019, 2021) was used to constrain their radius. The GW signal GW170817 gave valuable constraints on the reduced tidal deformability of the merging stars (see Section 2.2). Furthermore, the observation of the electromagnetic counterpart of GW170817, indicated, that the merger remnant was initially a HMNS that collapse to a BH after a short amount of time, which puts an upper limit on the maximum NS mass (see, e.g., Margalit & Metzger, 2017; Rezzolla et al., 2018).

TOV-related quantities, such as the radius or tidal deformability of a NS with a characteristic mass (often 1.4 or $1.6M_{\odot}$), or the maximum allowed NS mass, are useful characteristics to describe the influence of the EOS on the dynamics of BNS mergers. Since merging BNSs systems initially consist of two effectively isolated NSs, TOV properties naturally correlate with the outcome of the merger. The tidal deformability has a large influence because it is the most important factor during the late inspiral and therefore also impacts the early post-merger phase (see, e.g., Radice et al., 2020). Furthermore, the velocity of the NSs at the merger is determined by the radii of the NS and has a large impact on the shock-heated ejecta and the early post-merger phase (see, e.g., Hotokezaka et al., 2013b). Finally, these quantities are a general measure of the “stiffness” of an EOS which is important for the post-merger evolution of the remnant (see Section 4.2).

However, there are some aspects of the EOS that can not be described by TOV parameters. The massive NSs resulting from the merger is hot and no longer in weak equilibrium and its central density is larger than that of isolated NSs. Meanwhile, the properties of a TOV star can only describe the cold beta-equilibrium EOS at lower densities. Nonetheless, several works have found that the peak frequencies of the post-merger GW signal are correlated to the tidal deformability or the radius of TOV stars and have developed several fit formulae (see, e.g., Bauswein & Stergioulas, 2015; Takami et al., 2015; Rezzolla & Takami, 2016; Kiuchi et al., 2020). Some studies have developed similar fit formulae for the mass of the dynamical ejecta or the disk as functions of TOV parameters (see, e.g., Nedora et al., 2021c; Henkel et al., 2023). However, these are much more uncertain, because the ejection of matter depends on several mechanisms which in turn depend on different EOS properties (see Section 2.3).

The so-called nuclear matter properties offer a different approach to the characterization of the EOS. The energy per particle of symmetric, uniform nuclear matter has a theoretical minimum close to $n \approx 0.16 \text{ fm}^{-3}$ ($\rho \sim 2.5 \times 10^{14} \text{ g cm}^{-3}$) called the saturation density n_0 . The

energy density can be expanded around the saturation density and isospin symmetry:

$$\frac{E}{A} = \frac{\epsilon}{n} = -B + \frac{1}{2}K\chi^2 + S(\chi)\beta^2 + \mathcal{O}(\chi^3) + \mathcal{O}(\beta^4) \quad (2.18)$$

where $\chi = \frac{(n-n_0)}{3n_0}$ and $\beta = \frac{n_n-n_p}{n} = 1 - 2Y_e$ are the expansion parameters. The expansion coefficients of symmetric nuclear matter are the binding energy B and the incompressibility K . The behavior away from isospin symmetry is defined by the symmetry energy term $S(\chi)$ which we define as the exact difference of the energy of pure neutron matter to symmetric matter:

$$S(\chi) = E_{\text{sym}}(\chi) = \frac{E}{A}(\beta = 0) - \frac{E}{A}(\beta = 1) \approx \left. \frac{1}{2} \frac{\partial^2 E/A}{\partial \beta^2} \right|_{\beta=0}. \quad (2.19)$$

It can also be expanded in χ

$$S(\chi) = S_v + L\chi + \frac{1}{2}K_{\text{sym}}\chi^2 + \mathcal{O}(\chi^3), \quad (2.20)$$

with the symmetry energy at saturation S_v , the slope parameter L , and the curvature parameter K_{sym} . The expansion parameters B , K , S_v , L , and K_{sym} are often referred to as nuclear matter properties. Their role is indicated in Fig. 2.8. The energy per particle of symmetric nuclear matter exhibits a minimum at the saturation density n_0 and the binding energy B . The incompressibility K measures the curvature at the minimum and the symmetry energy E_{sym} is defined as the difference of the energy per particle of symmetric nuclear matter and pure neutron matter.

Nuclear matter properties are a universally applicable and well-known tool to describe any EOS close to the saturation density. This means, that, similar to the properties of TOVs, they are not optimally suited to describe the cores of massive NSs which can reach up to 8 times the

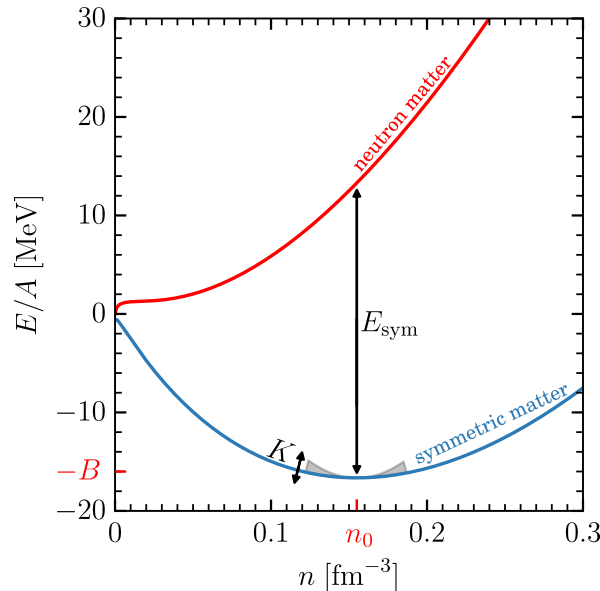


Figure 2.8.: Sketch of the energy per particle of symmetric nuclear matter and pure neutron matter. The role of the binding energy, symmetry energy, and incompressibility are indicated.

saturation density. However, unlike TOV parameters, different nuclear matter parameters are sensitive to different density regimes and therefore provide a more detailed description of the EOS' density dependence. Furthermore, they also parametrize the composition dependence. The influence of nuclear matter properties in BNS mergers is mostly unexplored. Only recently [Most & Raithel \(2021\)](#) have studied the impact of the slope parameter L on the post-merger GW emission and the ejection of matter.

2.4.4. Phenomenological models

Directly deriving an EOS from an ab-initio microphysical description of the nuclear interaction, is not possible for the extreme densities present in NSs. Therefore, simulations of supernova and compact-object mergers require the use of phenomenological models to cover all the necessary densities. A popular choice are models based on Skyrme interactions (see, e.g., [Stone & Reinhard, 2007](#)) such as the widely used Lattimer & Swesty (LS) EOS ([Lattimer & Swesty, 1991](#)). Skyrme interactions are constructed from a zero-range interaction in the mean field approximation from which a parametrized energy-density functional (EDF) is derived. The EDF depends on the particle density n , the proton fraction x , the temperature T , and several free parameters. These parameters are usually fit to experimental data and astrophysical observations. The LS EOS, as well as the Schneider-Roberts-Ott (SRO) EOS code ([Schneider et al., 2017, 2018](#)) used in this thesis, is based on a Skyrme EDF of the form ([Lattimer & Swesty, 1991](#))

$$\begin{aligned} \epsilon(n, x, T) = & \sum_t \frac{\tau_t(n, x, T)}{2m_t^*(n, x)} - xn\Delta \\ & + [a + 4bx(1-x)]n^2 + cn^{1+\delta}. \end{aligned} \quad (2.21)$$

The first term gives the kinetic-energy contribution to the internal energy with the index t summing over isospin degrees of freedom (i.e., $t \in [p, n]$) and is modeled as a non-interacting nucleon gas with the effective mass m^* . The second term contains the mass difference of protons and neutrons Δ . The last two terms parametrize nucleon interactions based on the parameters a, b, c and δ . A nucleon's motion in a potential that depends on momentum and energy is approximated by the motion of a quasi-nucleon with mass m^* in a mean field that depends on density. The effective mass is, therefore, density and proton-fraction dependent. Note that the first term of Eq. (2.21) not only includes the thermal energy at finite temperatures but also the contribution of the degeneracy energy at zero temperature because the kinetic energy density τ approaches a non-zero value in the limit of $T \rightarrow 0$:

$$\tau_t(n, x, T = 0) = \frac{(3\pi n_t)^{5/3}}{5\pi^2}. \quad (2.22)$$

On top of the contribution from uniform nuclear matter, the LS and SRO EOS include non-uniform nuclear matter, α particles, heavy nuclei, electrons, and photons. See [Lattimer & Swesty \(1991\)](#) and [Schneider et al. \(2017\)](#) for more details.

Another popular approach for the creation of EOS for astrophysics is the relativistic mean-field (RMF) model ([Shen et al., 1998b,a, 2011](#)). Several commonly used EOS models are based on the RMF approach, such as the Shen ([Shen et al., 1998a](#)), DD2 ([Banik et al., 2014](#)), and the SFHo EOS ([Steiner et al., 2013](#)). In RMF theory, the properties of uniform nuclear matter

are derived from a parametrized Lagrangian density, incorporating the strong interaction via meson exchanges. The coupling constants of the meson exchange terms and the meson masses are free parameters, which are fitted to experimental data. The Shen EOS is constructed from the TM1 parameter set (Sugahara & Toki, 1994), which is fitted to ground-state properties of stable as well as unstable nuclei. Similarly to Skyrme EDFs, the energy density includes a kinetic energy term with an effective mass m^* . However, unlike the non-relativistic Skyrme functional, the single particle kinetic energy is given by the relativistic expression $\epsilon_t = \sqrt{k^2 + m_t^{*2}}$.

3. Simulating neutron star mergers

Simulations of BNS mergers require the modeling of baryon matter (neutrons, protons, and nuclei), leptonic matter (electrons, positrons, and neutrinos), photons, and the dynamic spacetime (i.e. the metric fields). The dynamics of curved spacetimes in the presence of matter source terms are described by Einstein's equations. To be able to numerically solve them they need to be expressed as an initial value problem which is described in Section 3.1. Baryons, electrons, positrons, and photons can be considered to be in thermodynamic equilibrium and can thus be described as a single perfect fluid, the properties of which are fully determined by the EOS (see Section 2.4). Section 3.2 describes the relativistic version of Euler's equations which determine the fluid dynamical evolution. This leaves the treatment of neutrinos, which need to be modeled by a radiation transport scheme as described in Section 3.3. Finally, in Section 3.4, we summarize the methods used in the simulations described in the following chapters. This section follows the unit convention $c = G = 1$ and uses the Einstein sum convention as well as the typical convention where Greek indices and roman indices indicate summation over 4 spacetime and 3 spatial dimensions, respectively.

3.1. Numerical relativity

Neutron stars and black holes are highly compact objects with strong gravitational fields, that need to be described by general relativity (GR). The Newtonian gravitational potential can be determined by solving Poisson's equation for a given matter distribution. Einstein's equations describe the dynamic evolution of the metric fields, which depends not only on the matter distribution but also on their current state, since they have intrinsic degrees of freedom, in the form of gravitational waves. Therefore, the simulation of compact object mergers requires the computational evolution of Einstein's equations alongside the hydrodynamic equations (see Section 3.2). This section gives an overview of the methods of NR, the field of research that studies the evolution of Einstein's equations with numerical methods, and is based on the monographies on the subject by [Baumgarte & Shapiro \(2021\)](#) and [Shibata \(2015\)](#). In Section 3.1.1, we describe the 3+1 decomposition of spacetime, a useful concept for the formulation of initial value problems in GR. In Section 3.1.3, we describe how the gauge freedom of GR can be used in numerical relativity (NR) simulations by choosing a gauge that avoids the appearance of singularities. Section 3.1.2 details the BSSN formulation of Einstein's equations, a commonly used formulation in numerical simulations of GR. Finally, Section 3.1.5 explains the formalism used to describe GWs and how they are extracted from NR simulations.

3.1.1. 3+1 decomposition

In physics, numerical simulations are usually based on differential equations, that describe the time evolution of a system, given an initial condition. This is known as an initial value problem. For example, hydrodynamical simulations start from an initial condition describing the distribution of matter, momentum, and energy in a bounded area of space. However, due to the absence of the concept of absolute time, the concept of initial conditions cannot be extended to GR in such a simple fashion.

The first step to formulating an initial value problem is to define a coordinate time t as a scalar function of spacetime. The hypersurfaces of constant coordinate time Σ_t create a foliation of spacetime that is sketched in Fig. 3.1. The local ratio of proper time and coordinate

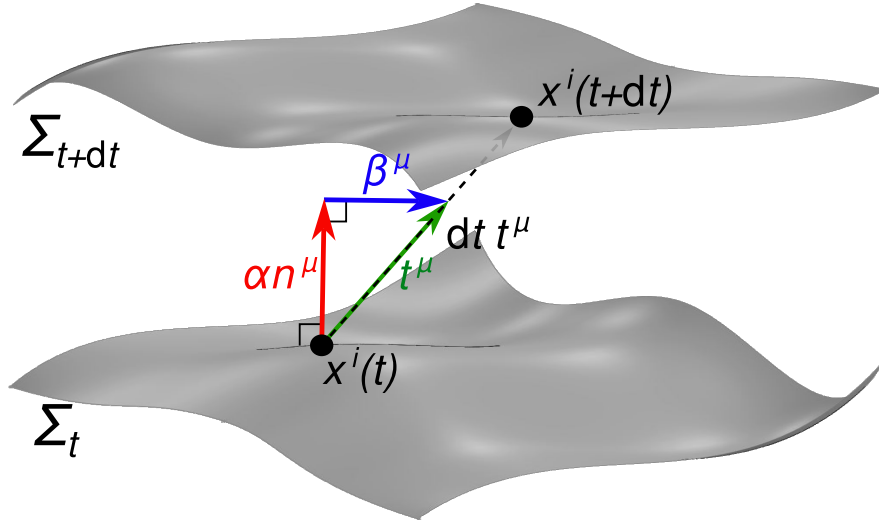


Figure 3.1.: Foliation of spacetime based on a coordinate time t .

time is called the lapse function α and given by

$$\alpha = -(\nabla_\mu t \nabla^\mu t)^{-1/2}, \quad (3.1)$$

where ∇_μ denotes the covariant derivative. The timelike, and future-directed normal to Σ_t is given by

$$n^\mu = -\alpha g^{\mu\nu} \nabla_\nu t, \quad (3.2)$$

with $n_\mu n^\mu = -1$. The 4-metric $g_{\mu\nu}$ induces a 3-metric $\gamma_{\mu\nu}$ onto the slices Σ given by

$$\gamma_{\mu\nu} = g_{\mu\nu} + n_\mu n_\nu, \quad (3.3)$$

which raises and lowers the indices of purely spatial tensors. We can now define a vector t^μ with $t^\mu \nabla_\mu t = 1$ as

$$t^\mu = \alpha n^\mu + \beta^\mu, \quad (3.4)$$

where β^μ can be any vector orthogonal to n^μ and is thus purely spacelike. It turns out t^μ is a useful choice for the time base vector because the vector $t^\mu dt$ connects two neighboring hypersurfaces Σ_t and Σ_{t+dt} . Accordingly, we chose the spatial coordinates $x^i(t)$ and $x^i(t+dt)$ such, that they are connected by $t^\mu dt$. The vector β^μ measures the amount by which the spatial

coordinates are shifted within a slice with respect to the normal vector and is thus called shift-vector. Note that the choice of lapse function and shift vector is equivalent to the choice of the coordinate system (see Section 3.1.3 for more detail). With these definitions in place, the spacetime line element can be rewritten as

$$ds^2 = \alpha^2 dt^2 + \gamma_{ij} (dx^i + \beta^i dt) (dx^j + \beta^j dt) . \quad (3.5)$$

We can now express the following 4-vectors/tensors in the new coordinate base:

$$t^\mu = (1, 0, 0, 0) , \quad (3.6)$$

$$\beta^\mu = (0, \beta^i) , \quad (3.7)$$

$$n^\mu = \alpha^{-1} (1, -\beta^i) , \quad (3.8)$$

$$g_{\mu\nu} = \begin{bmatrix} -\alpha^2 + \beta^i \beta_i & \beta_i \\ \beta_i & \gamma_{ij} \end{bmatrix} . \quad (3.9)$$

Furthermore, it is useful to express the determinant of the 4-metric g in terms of the determinant of the 3-metric γ :

$$g = -\alpha^2 \gamma . \quad (3.10)$$

Now that we have defined a distinction between space and time, we need an equivalent to the time derivative, that customarily determines the evolution of initial value problems. In the case of the 3+1 decomposition, this is given by the Lie-derivative along t^μ , \mathcal{L}_t which describes the change of tensors along world lines with constant coordinates x^i . The Lie-derivative of a vector v^μ along a curve with the tangential vector u^μ is given by

$$\mathcal{L}_u v^\mu = u^\nu \partial_\nu v^\mu - v^\nu \partial_\nu u^\mu . \quad (3.11)$$

Our partial time derivative is therefore given by

$$\mathcal{L}_t = \alpha \mathcal{L}_n + \mathcal{L}_\beta , \quad (3.12)$$

with

$$(\mathcal{L}_n \gamma)_{\mu\nu} = -2\alpha K_{\mu\nu} , \quad (3.13)$$

which defines the purely spatial tensor K_{ij} , called the extrinsic curvature. Equation (3.12) can be rewritten in terms of our coordinate basis as

$$\left(\partial_t - \beta^k \partial_k \right) \gamma_{ij} = -2\alpha K_{ij} + \gamma_{ik} \partial_j \beta^k + \gamma_{jk} \partial_i \beta^k . \quad (3.14)$$

Next, an equation specifying K_{ij} in terms of the matter and energy distribution has to be derived from Einstein's equations

$$R_{\mu\nu} - \frac{1}{2} R g_{\mu\nu} = 8\pi T_{\mu\nu} , \quad (3.15)$$

where $R_{\mu\nu}$ and R are the Ricci tensor and the Ricci scalar and $T_{\mu\nu}$ is the energy-momentum tensor (see Section 3.2). Note that Einstein's equations are second-order differential equations for $g_{\mu\nu}$, so we are looking for an equation that specifies the first time derivative of the extrinsic curvature and thereby the second time derivative of γ_{ij} . We can use n^μ and γ_{ij} to project out

the spatial and timelike components of Eq. (3.15) (for a detailed derivation see, e.g., [Shibata \(2015\)](#)). The energy-momentum tensor decomposes to

$$T_{\mu\nu} = En_\mu n_\nu + S_\mu n_\nu + S_\nu n_\mu + S_{\mu\nu}. \quad (3.16)$$

Contracting Eq. (3.15) twice with n^μ yields the Hamiltonian constraint equation

$$R - K_{ij}K^{ij} + K^2 = 16\pi E, \quad (3.17)$$

where $K = \gamma^{ij}K_{ij}$ is the trace of K_{ij} . Projecting once with n_μ and once with γ_{ij} yields the momentum constraint equations:

$$\nabla_i K^i_j - \nabla_j K = 8\pi S_j, \quad (3.18)$$

where we have used ∇_i , the covariant derivatives associated to γ_{ij} . Equations (3.17) and (3.18) are elliptic equations and do not contain time derivatives, so they are not the evolution equation for the extrinsic curvature we are looking for. Instead, they are conditions, that need to be fulfilled on all spatial hypersurfaces and have to be solved to construct initial data (see Section 5.3). Furthermore, it is useful to define H and M^i as the residual of the Hamiltonian and momentum constraint equations. Mathematically, the constraint violation should stay zero if the initial conditions satisfy the constraint equations and the system is evolved according to Einstein's equations. However, due to numerical inaccuracies, this is only approximately the case in numerical simulations. It is common to compute the violation of the constraint equations to monitor the spacetime evolution.

Finally, we obtain the equation specifying the evolution of K_{ij} by contracting Einstein's equations twice with γ_{ij} :

$$\begin{aligned} (\partial_t - \beta^k \partial_k) K_{ij} = & -8\pi\alpha \left[S_{ij} - \frac{1}{2}\gamma_{ij}(S - E) \right] \\ & + \alpha \left(-2K_{ik}K_j^k + KK_{ij} \right) \\ & + \alpha R_{ij} - \nabla_i \nabla_j \alpha \\ & + K_{ik} \partial_j \beta^k + K_{jk} \partial_i \beta^k, \end{aligned} \quad (3.19)$$

with $S = \gamma^{ij}S_{ij}$, the trace of S_{ij} .

Equations (3.14) and (3.19) are known as the ADM equations ([Arnowitt et al., 2008](#)). They specify the time derivatives for the fields γ_{ij} and K_{ij} needed for the evolution of the spacetime in an initial value problem and are thus referred to as the evolution equations in the context of NR.

3.1.2. The BSSN formulation

The evolution and constraint equations, Eqs. (3.14) and (3.17) to (3.19), introduced in Section 3.1.1 enable the formulation of Einstein's equations as an initial value problem but they are not strongly hyperbolic. Strong hyperbolicity is needed for the problem to be well-posed because it ensures that the solution does not grow faster than exponentially with respect to the initial data (see, e.g., [Kreiss & Lorenz, 1989](#)). Since the formulation of the ADM equations, a lot of effort has been devoted to finding a hyperbolic form of the ADM equations. The

Baumgarte-Shapiro-Shibata-Nakamura (BSSN) formulation of Einstein's equations (Shibata & Nakamura, 1995; Baumgarte & Shapiro, 1998; Brown, 2009) achieves strong hyperbolicity via a conformal decomposition of the 3-metric together with several other modifications.

The conformal decomposition is an often-used formulation in NR based on writing the spatial metric as the product of a scalar conformal factor and a conformal metric $\tilde{\gamma}$. In the BSSN formulation, the conformal factor ϕ and conformal metric are defined as

$$\phi = \frac{1}{12} \ln \gamma \quad (3.20)$$

$$\tilde{\gamma}_{ij} = e^{-4\phi} \gamma_{ij}. \quad (3.21)$$

Here, the conformal factor ϕ appears in an exponential form but there are other conventions (see, e.g., Section 3.1.3 and Section 5.3). Furthermore, the contraction of the Christoffel symbols $\tilde{\Gamma}^i_{jk}$ associated to $\tilde{\gamma}$

$$\tilde{\Gamma}^i = \tilde{\gamma}^{jk} \tilde{\Gamma}^i_{jk} \quad (3.22)$$

are promoted to independently evolved variables. In addition to ϕ , $\tilde{\gamma}_{ij}$, and $\tilde{\Gamma}^i$, the evolved fields include K and $\tilde{A}_{ij} = e^{-4\phi} A_{ij}$. The evolution equations are given by (see, e.g., Brown, 2009)

$$\partial_{\perp} \phi = \frac{1}{6} \partial_k \beta^k - \frac{1}{6} \alpha K \quad (3.23)$$

$$\partial_{\perp} \tilde{\gamma}_{ij} = -2\alpha \tilde{A}_{ij} - \frac{2}{3} \tilde{\gamma}_{ij} \partial_k \beta^k \quad (3.24)$$

$$\partial_{\perp} K = \alpha \left(\tilde{A}_{ij} \tilde{A}^{ij} + \frac{1}{3} K^2 \right) - \gamma^{ij} \nabla_i \nabla_j \alpha + 4\pi(S + E) \quad (3.25)$$

$$\begin{aligned} \partial_{\perp} \tilde{A}_{ij} = e^{-4\phi} [& \alpha (R_{ij} - 8\pi S_{ij}) - \nabla_i \nabla_j \alpha]^{\text{TF}} \\ & - \frac{2}{3} \tilde{A}_{ij} \partial_k \beta^k + \alpha (K \tilde{A}_{ij} - 2\tilde{A}_{ik} \tilde{A}^k_j) \end{aligned} \quad (3.26)$$

$$\begin{aligned} \partial_{\perp} \tilde{\Gamma}^i = & \tilde{\gamma}^{jk} \partial_j \partial_k \beta^i + \frac{2}{3} \tilde{\Gamma}^i_{jk} \partial_l \beta^l \\ & + \frac{1}{3} \tilde{\nabla}^i (\partial_k \beta^k) - 2\tilde{A}^{ij} \partial_j \alpha + 2\alpha \tilde{A}^{jk} \tilde{\Gamma}^i_{jk} \\ & + 12\alpha \tilde{A}^{ij} \partial_j \phi - \frac{4}{3} \alpha \tilde{\nabla}^i K - 16\pi \alpha \tilde{\gamma}^{ij} S_j, \end{aligned} \quad (3.27)$$

where the operator ∂_{\perp} is shorthand for $\partial_t - \mathcal{L}_{\beta}$ and the notation $[\dots]^{\text{TF}}$ indicates that the term is made trace free with respect to the conformal metric. Equations (3.25) and (3.27) contain the Hamiltonian and momentum constraint equations, respectively. Since they are equal to zero, their addition does not change the solution, but it turns out that it is crucial for the hyperbolicity of the equations (Brown, 2009).

3.1.3. Choosing a coordinate system

The lapse function and shift vector are not constrained by the Einstein equations. Instead, they can be freely chosen and represent the freedom of coordinate choice in GR. In NR simulations, they are usually chosen in a way to avoid unwanted properties related to singularities.

The lapse function can be evolved in such a way that it tends to zero at the singularity in the center of an BH. This way, the proper time does not advance in the center of the BH, even

if the coordinate time does, and the singularity is never reached, thus making it possible to evolve the interior of BH. This property is called singularity avoidance and is crucial for the successful evolution of BH spacetimes. One possible choice is the maximal slicing condition which corresponds to the choice $K = 0 = \partial_t K$. It introduces an equation for α :

$$\nabla_i \nabla^i \alpha = 8\pi\alpha \frac{S + E}{2} + \alpha A_{ij} A^{ij}, \quad (3.28)$$

where $A_{ij} = K_{ij} - \frac{1}{3}K$ is the traceless part of K_{ij} . The choice $K = 0$ is equivalent to $\Delta_\nu n^\nu$ and thus prohibits the focusing of the timelike normals and hence, the appearance of irregular regions in the spatial hypersurfaces. However, in numerical simulation, it leads to a phenomenon called horizon stretching (see [Shibata, 2015](#), for more detail). However, it is still employed in the context of initial data generation (see Section 5.3). Many simulations instead use the 1+log slicing condition given by

$$(\partial_t - \beta^i \partial_i)\alpha = -\alpha K. \quad (3.29)$$

Experience has shown, that this choice has a similarly strong singularity avoidance property.

A useful condition for the shift is the minimal distortion condition. Using the conformal decomposition given by

$$\gamma_{ij} = \psi^4 \tilde{\gamma}_{ij}, \quad (3.30)$$

it can be written as

$$\tilde{\nabla}_i (\delta_t \tilde{\gamma}^{ij}) = 0, \quad (3.31)$$

which results in an elliptic equation for the shift:

$$\begin{aligned} \tilde{\nabla}^i \tilde{\nabla}_i \tilde{\gamma}_{jk} \beta^k + \frac{1}{3} \tilde{\nabla}_j \tilde{\nabla}_i \beta^i + \tilde{R}_{ji} \beta^i \\ - 2\tilde{A}_{ij} \left(\tilde{\nabla}^i \alpha - \frac{\alpha}{\sqrt{\gamma}} \tilde{\nabla}^i \sqrt{\gamma} \right) - \frac{4}{3} \alpha \tilde{\nabla}_j K = 16\pi\alpha S_j, \end{aligned} \quad (3.32)$$

where $\tilde{\nabla}_i$ and \tilde{R}_{ij} are the covariant derivative and Ricci tensor associated with the conformal metric $\tilde{\gamma}$ and $\tilde{A}_{ij} = \psi^{-4} A_{ij}$. It can be shown, that this choice corresponds to a minimal change of the coordinate distortion, hence the name.

A common gauge choice for the use with the BSSN formulation of Einstein's equations, is the 1+log slicing condition, Eq. (3.29), and the Gamma-driver or moving puncture gauge for the shift. The latter is similar to the minimal distortion condition but takes the form of two hyperbolic equations:

$$(\partial_t - \beta^k \partial_k) \beta^i = \frac{3}{4} b^i \quad (3.33)$$

$$(\partial_t - \beta^k \partial_k) b^i = \partial_t \tilde{\Gamma}^i - \eta b^i, \quad (3.34)$$

where b^i is an auxiliary field that is independently evolved by Eq. (3.34) and η is a damping constant, that can be adjusted to suppress unphysical oscillations of the shift vector. The fact that these equations are hyperbolic instead of elliptic like Eq. (3.32) lowers the computational cost of their solution.

3.1.4. Solving Einstein's equations numerically

The solutions to Einstein's equations in the 3+1 decomposition are always smooth, so their numerical integration is not as complicated as for hydrodynamical conservation laws (see Section 3.2.2) and can be performed with standard finite difference methods. Finite difference methods usually approximate a derivative by calculating the derivative of a high-order Lagrange polynomial interpolant. We typically use 4th-order centered finite-difference stencils given by

$$\partial_x v(x_i) \approx \frac{v_{i-2}/4 - 2v_{i-1} - 2v_{i+1} + v_{i+2}/4}{3\Delta x}, \quad (3.35)$$

for a field v on a discrete grid x_i with grid spacing Δx . No special treatment needs to be applied except for the shift advection equations (3.33) and (3.34), which require the use of upwind stencils (i.e. stencils, that are biased in the direction of the advection) to achieve stable evolutions.

3.1.5. Gravitational Waves

Accelerated masses cause the emission of gravitational waves – ripples in spacetime – which were already predicted by Albert Einstein in 1916 (Einstein, 1916). They are wave-like perturbations of the metric $g_{\mu\nu}$ which can be described as small deviations from the Minkowski metric $\eta_{\mu\nu}$ in vacuum,

$$g_{\mu\nu} = \eta_{\mu\nu} + h_{\mu\nu}. \quad (3.36)$$

In the limit of linearized gravity ($|h_{\mu\nu}| \ll 1$) together with the gauge conditions

$$h_{\mu 0} = h_{\mu}{}^{\mu} = 0 \quad (\text{transverse traceless gauge}), \quad (3.37)$$

$$\nabla_{\mu} h^{\mu\nu} = 0, \quad (3.38)$$

one obtains a homogeneous wave equation for the perturbation $h_{\mu\nu}$:

$$\nabla_{\sigma} \nabla^{\sigma} h_{\mu\nu} = 0. \quad (3.39)$$

Only two degrees of freedom remain for $h_{\mu\nu}$, representing the two polarization states of GWs. For GWs traveling along the z -axis in a Cartesian coordinate system, $h_{\mu\nu}$ takes the form

$$h_{\mu\nu} = \begin{bmatrix} 0 & 0 & 0 & 0 \\ 0 & h_{+} & h_{\times} & 0 \\ 0 & h_{\times} & -h_{+} & 0 \\ 0 & 0 & 0 & 0 \end{bmatrix}. \quad (3.40)$$

The relative displacement of two test masses in free fall due to the passing of GWs is proportional to h_{+} and h_{\times} , so they are called the GW strain and can be thought of as the wave's amplitude.

To extract GW waveforms and spectra we employ the Newman-Penrose formalism (Newman & Penrose, 1962), following Sect. 5 of Hinder et al. (2013) for its practical implementation. The starting point of the procedure is the Weyl tensor given by the traceless part of the Riemann tensor (associated with the 4-metric)

$$C_{\mu\nu\sigma\rho} = R_{\mu\nu\sigma\rho} - \frac{1}{2}R(g_{\mu\sigma}R_{\nu\rho} - g_{\mu\rho}R_{\nu\sigma} - g_{\nu\sigma}R_{\mu\rho} + g_{\nu\rho}R_{\mu\sigma}), \quad (3.41)$$

which has 10 independent components. It can be expressed by the five complex Newman-Penrose scalars given by the contractions with the vectors of a suitable null tetrad $(l^\mu, k^\mu, m^\mu, \bar{m}^\mu)$, where l_μ and k_μ are respectively radially outgoing and ingoing null vectors and \bar{m}^μ is the complex conjugate of m^μ . The second time derivative of the GW strain polarization components \ddot{h}_+ and \ddot{h}_\times can then be related to the fourth scalar Ψ_4 by:

$$\ddot{h}_+ - i\ddot{h}_\times = \Psi_4 = \sum_{l=2}^{\infty} \sum_{m=-l}^l C_{lm} {}_{-2}Y_{lm}(\theta, \phi), \quad (3.42)$$

where Ψ_4 was expanded in weighted spherical harmonics of spin weight -2, ${}_{-2}Y_{lm}(\theta, \phi)$. The expansion coefficients C_{lm} are extracted at multiple finite coordinate radii inside the simulation domain and extrapolated to null infinity along outgoing radial null geodesics. From them, the strain components h_+ and h_\times are obtained by performing the time integration with the ‘‘fixed frequency integration’’ (FFI) method (Reisswig & Pollney, 2011). Finally, the power spectral density (PSD) of the signal is given by

$$\tilde{h}(f) = \sqrt{\frac{|\tilde{h}_+(f)|^2 + |\tilde{h}_\times(f)|^2}{2}}, \quad (3.43)$$

with the frequency-domain strain components

$$\tilde{h}_{+, \times}(f) = \int_0^\infty h_{+, \times}(t) e^{-i2\pi ft} dt. \quad (3.44)$$

3.2. Relativistic hydrodynamics

The fluid motion of NS collisions is described by the conservation equations of a relativistic perfect fluid in a curved spacetime (called the relativistic Euler equations). In Section 3.1, we already introduced a framework for evolving curved spacetimes numerically. While the fluid is in principle made from a huge number of interacting particles, described by kinetic theory, it is in practice much more useful to approximate it, in the form of a perfect fluid obeying Euler’s equation (see, e.g., Chapter 2 of Rezzolla & Zanotti (2013), for a detailed derivation). Euler’s equation describes the conservation of energy and momentum

$$\nabla_\nu T^{\mu\nu} = 0 \quad (3.45)$$

and the rest-mass conservation (also known as the continuity equation)

$$\nabla_\mu(\rho u^\mu) = 0, \quad (3.46)$$

where ρ is rest-mass density and u^μ is the fluids 4-velocity field. The fluid’s energy and momentum are described by the energy-momentum tensor of a perfect fluid

$$T_{\mu\nu} = \rho h u_\mu u_\nu + p g_{\mu\nu}, \quad (3.47)$$

where $h = 1 + \varepsilon + \frac{p}{\rho}$ is the relativistic specific enthalpy and p is the pressure. Inserting Eq. (3.47) into Eq. (3.46) gives the relativistic Euler equations:

$$u^\mu \nabla_\mu u_\nu + \frac{1}{\rho h} (g^\mu{}_\nu + u^\mu u_\nu) \nabla_\mu p = 0 \quad (3.48)$$

$$u^\mu \nabla_\mu \varepsilon + \rho h \nabla_\mu u^\mu = 0. \quad (3.49)$$

Equations (3.46), (3.48) and (3.49) are 6 independent equations containing 7 free variables: ρ , u^μ , ϵ , and p . The set of equations is closed by the EOS, which gives a relation for the pressure in terms of the other thermodynamic variables (see Section 2.4). Note that the conservation laws hold for any kind of perfect fluid and are thus independent of the microphysical interaction of the particles, which is entirely represented by the EOS. As mentioned in Section 2.4.2, most realistic microphysical EOS models are formulated in terms of the baryon-number density which is converted to a rest-mass density via a constant mass factor. This means that, in practice, Eq. (3.46) actually describes the conservation of the total baryon number.

3.2.1. The Valencia formulation

While Eqs. (3.46), (3.48) and (3.49) describe the fluid dynamics of BNS mergers, they are not well suited for numerical integration. The main reason is that shocks, i.e., discontinuities, can appear in the solution of the conservation equations whenever fluid elements collide supersonically. In the presence of shocks, several mathematical and numerical problems arise, from which the necessity for special numerical methods arises (see, e.g., [LeVeque, 1992](#), for a detailed explanation). One class of numerical schemes commonly used to simulate fluid dynamics in the presence of shocks are the so-called “high-resolution shock-capturing” or HRSC schemes (see Section 3.2.2 which require the evolved equations to be of the form

$$\partial_t \mathcal{U} + \partial_i \mathcal{F}^i(\mathcal{U}) = \mathcal{S}(\mathcal{U}), \quad (3.50)$$

which is commonly called the flux-conservative form. The vector \mathcal{U} describes the state of the fluid and \mathcal{F}^i and \mathcal{S} are the flux and source vectors, respectively, which do not contain any derivatives of \mathcal{U} . The state vector \mathcal{U} is made up of the conserved variables which in turn are built from the primitive variables ρ , ϵ , and the 3-velocities v^i .

In the Valencia formulation of hydrodynamics ([Banyuls et al., 1997](#)), the conserved variables are given by

$$\mathcal{U} = \begin{pmatrix} \tilde{D} \\ \tilde{S}_j \\ \tilde{\tau} \end{pmatrix} = \sqrt{\gamma} \begin{pmatrix} D \\ S_j \\ \tau (= E - D) \end{pmatrix} = \sqrt{\gamma} \begin{pmatrix} \rho W \\ \rho h W^2 v_j \\ \rho h W^2 - p - \rho W \end{pmatrix}. \quad (3.51)$$

where we have introduced the Lorentz factor

$$W = \alpha u^t = \frac{1}{\sqrt{1 - v^i v_i}} \quad (3.52)$$

and the 3-velocities

$$v^i = \frac{u^i}{W} + \frac{\beta^i}{\alpha}. \quad (3.53)$$

To reduce numerical error, the conserved internal energy density $\tau = E - D$ is evolved instead of the conserved energy density E . The flux vectors and the source vector are given by

$$\mathcal{F}^i = \begin{pmatrix} (\alpha v^i - \beta^i) \tilde{D} \\ \alpha \tilde{S}_j - \beta^i \tilde{S}_j \\ \alpha (\tilde{S}^i - \tilde{D} v^i) - \beta^i \tilde{\tau} \end{pmatrix}, \quad (3.54)$$

and

$$\mathcal{S} = \begin{pmatrix} 0 \\ \frac{1}{2}\alpha\tilde{S}^{ik}\partial_j\gamma_{ik} + \tilde{S}_i\partial_j\beta^i - \tilde{E}\partial_j\alpha \\ \alpha\tilde{S}^{ij}K_{ij} - \tilde{S}^k\partial_k\alpha \end{pmatrix}, \quad (3.55)$$

respectively. Here we recognize the source terms E , S_i , and $S_{ij} = \tilde{S}_{ij}/\sqrt{\gamma}$ from Section 3.1.1. Strictly speaking, the momenta S_i and the internal energy τ are not conserved, since they are coupled to the spacetime through the source terms \mathcal{S} . For a multi-component fluid, the density of each component obeys a separate continuity equation. In our simulations, we actually evolve the total density D and the proton density $D_p = Y_e D$.

3.2.2. Solving Euler's equations numerically

As mentioned at the beginning of the previous section, HRSC schemes are often used for solving equations in flux-conservative form. In this section, we summarize the basic concepts of HRSC finite volume methods based on Riemann solvers. Finite volume methods evolve cell averages of the conserved quantities by solving the so-called Riemann problem at the cell boundaries and date back to Godunov (1959). In the following, we explain the basic concept of finite volume methods for a one-dimensional function u obeying a conservation law $\partial_t u + \partial_x f(u) = 0$ using Godunov's method. Finite volume schemes approximate the exact solution u on a grid of cells centered around $x_i = i\Delta x$ at finite timesteps $t^n = n\Delta t$. In this example, the grid spacing Δx and timestep Δt are constants but the method can be adapted to higher dimensions and more complicated grid structures. The function u is approximated as a piecewise constant function, where u_i^n is the average of u in the i th cell at time t^n :

$$u_i^n = \frac{1}{\Delta x} \int_{x_i - \Delta x/2}^{x_i + \Delta x/2} u(t^n, x) dx. \quad (3.56)$$

The solution of u at a cell boundary can thus be represented as

$$u(t^n, x) = \begin{cases} u_i^n & \text{for } x < x_i + \Delta x/2 \\ u_{i+1}^n & \text{for } x > x_i + \Delta x/2 \end{cases}. \quad (3.57)$$

The value in the next timestep u_i^{n+1} is then exactly given by

$$u_i^{n+1} = u_i^n - \frac{\Delta t}{\Delta x} (F_{i+1/2} - F_{i-1/2}), \quad (3.58)$$

where $F_{i\pm 1/2}$ denotes the integral from t^n to t^{n+1} of the flux f over the cell boundary at $x = x_i \pm \frac{1}{2}\Delta x$. The type of fluid configuration shown in Eq. (3.57) is called Riemann problem and the solutions are known exactly. They contain three types of non-linear hydrodynamical waves propagating from the position of the initial discontinuity: rarefaction waves, contact discontinuities and shocks (see, e.g., Rezzolla & Zanotti, 2013, for a detailed description). The fluxes $F_{i\pm 1/2}$ can thus be calculated exactly, by solving the Riemann problem at each cell interface. This approach requires the waves to be entirely contained in one cell at each timestep, i.e.,

$$\Delta t \leq \frac{\Delta x}{c}, \quad (3.59)$$

where c is the speed of sound of the fluid. This criterion is called the Courant–Friedrichs–Lewy (CFL) criterion (Courant et al., 1928) and needs to be fulfilled by any numerical scheme for the solution of hyperbolic differential equations. In practice, the timestep in a simulation is set to

$$\Delta t = C_{\text{CFL}} \frac{\Delta x}{c}. \quad (3.60)$$

The constant $C_{\text{CFL}} < 1$ is generally known as the CFL or Courant factor. Note that in NR simulations, the CFL condition is determined by the speed of light which should always be larger than the fluid's speed of sound.

A general finite-volume scheme usually uses an approximation to the exact solution of the Riemann problem and a so-called reconstruction operator. It can be divided into three steps:

- (i) It begins with the reconstruction step by calculating the primitive variables on each cell interface. Higher order accuracy can be achieved by approximating the variables with polynomials of higher order, taking multiple grid cells near the interface into account. Many reconstruction operators, such as the monotonicity-preserving scheme (MP) (Suresh & Huynh, 1997), have been developed to ensure high-order reconstruction while avoiding the creation of artificial extrema in the presence of discontinuities.
- (ii) Next, the fluxes at the cell boundaries are calculated from the reconstructed variables and used to compute the conservative variables at the new time step. In general, this is not done by exactly solving the Riemann problem. Instead, an approximation is used, resulting in so-called approximate Riemann solvers, such as the HLL solver (Einfeldt, 1988).
- (iii) Finally, the primitive variables are recovered on the new time level (the "recovery step"). Given that the equation of state needs to be evaluated in the calculation of the conserved variables, this step may not be an easy problem to solve and must be addressed numerically, i.e. by the use of a Newton-Raphson scheme. Because the calculation of realistic EOS requires a relatively large amount of computational effort, they are supplied in tabulated form and evaluated with interpolation.

3.3. Neutrino transport

While neutrinos are of great dynamical importance in supernovae, they are not as relevant for the dynamics of BNS mergers. However, as described in Section 2.3.2, they are vital for the composition of the ejected matter and thus for the KNe.

The emission and reabsorption of neutrinos change the composition and the energy and momentum content of the fluid which corresponds to source terms in Eqs. (3.45) and (3.46):

$$\nabla_{\mu} (n_{\text{p,n}} u^{\mu}) = \pm R \quad (3.61)$$

$$\nabla_{\nu} T^{\mu\nu} = Q u^{\mu}, \quad (3.62)$$

where $n_{\text{p,n}}$ are respectively the proton and neutron number densities, and R and Q are the source terms due to neutrino interactions: R is the net lepton number exchange rate due to the absorption and emission of electron neutrinos and antineutrinos, while Q is the net energy deposition rate due to the absorption and emission of (anti-) neutrinos of all flavors. Baryon

number conservation dictates, that the source terms for the number density of neutrons and protons must sum to zero. To consistently calculate the source terms, the neutrino phase-space distribution function $f(x^\mu, p^\mu)$ has to be evolved as a function of spacetime and the neutrino momenta p^μ . The evolution is described by the relativistic collisional Boltzmann equation (Lindquist, 1966)

$$p^\mu \left(\partial_\mu f - \Gamma^\nu{}_{\mu\sigma} p^\sigma \frac{\partial f}{\partial p^\nu} \right) = \left(\frac{df}{dt} \right)_{\text{coll}}, \quad (3.63)$$

where the collisional source term $\left(\frac{df}{dt} \right)_{\text{coll}}$ includes the interaction of the neutrinos the fluid and with themselves. The treatment of neutrinos in BNS merger simulations is challenging. On one hand, numerically solving of Eq. (3.63) is computationally very expensive. On the other hand, an approximative description is not trivial because the simulation domain includes vastly different regions regarding the neutrino's interaction with matter: Inside of NSs, neutrinos are trapped, i.e. their mean free path is much smaller than the NS radius. They are therefore in thermal equilibrium with the baryonic matter and only slowly diffuse out of the NS via a random walk. Outside of the NS the density and thus the probability for interactions between neutrinos and baryons drops sharply. These two regimes are called trapped and free streaming regimes.

3.3.1. Leakage scheme

A neutrino leakage scheme is an approximation to a full radiation transport scheme (van Riper & Lattimer, 1981; Ruffert et al., 1995; Rosswog & Liebendörfer, 2003). It separates the computational domain into the trapped and free streaming regimes and connects them by interpolation in the transition region. In the following, we summarize the key features of the leakage scheme used in the simulations presented in this thesis. For a more detailed description see Galeazzi et al. (2013) and references therein.

Most numerical simulations only take electrons and positrons as leptonic degrees of freedom into account (see Loffredo et al., 2023, though, for a very recent work that treats muons as separate degrees of freedom). Therefore, the neutrino can be approximately represented by three species: Electron neutrinos ν_e , electron antineutrinos $\bar{\nu}_e$, and a combined species representing μ and τ neutrinos and antineutrinos, usually simply named ν_x . In the trapped regime, the diffusion rates Q_I^D and R_I^D are calculated by estimating the diffusion timescale based on the diffusion timescale t_{diff} , where I is either ν_e , $\bar{\nu}_e$, or ν_x :

$$t_{\text{diff}} = \mathcal{D} \lambda_I(E_I) \tau_I^2(E_I), \quad (3.64)$$

The optical depths τ_I are defined as the integral of the inverse mean free path λ_I along a line of sight towards the NS

$$\tau_I(E_I) = \int \frac{ds}{\lambda_I(E_I)}, \quad (3.65)$$

with the neutrino energy E_I , and the proper line element ds . \mathcal{D} is a tuning parameter. The value of this parameter was suggested as 3 by Ruffert et al. (1995); Rosswog & Liebendörfer (2003) by random walk arguments. Calibration against more sophisticated transport methods led to a larger value of 6 (O'Connor & Ott, 2010). In practice, leakage implementations need an approximative scheme to evolve the optical depths. The scheme used for the simulations performed as part of this thesis is explained in Neilsen et al. (2014). Despite being fairly simple,

the scheme is effective in tracking the evolution of the optical depth in the complex geometry of BNS mergers.

The mean free path λ_I is the result of the combination of several scattering and absorption processes. These are the important processes (and the ones included in our simulations):

- (i) coherent neutrino scattering on heavy nuclei with mass number A

$$\nu + A \rightarrow \nu + A, \quad \nu = \nu_e, \bar{\nu}_e, \nu_x$$

- (ii) elastic neutrino scattering on free nucleons

$$\nu + [n, p] \rightarrow \nu + [n, p], \quad \nu = \nu_e, \bar{\nu}_e, \nu_x$$

- (iii) and absorption of electron neutrinos and antineutrinos on free nucleons

$$\nu_e + n \rightarrow e^- + p,$$

$$\bar{\nu}_e + p \rightarrow e^+ + n.$$

The total mean free path is given by summing up all the contributions to the inverse mean free path of the above-listed processes which are schematically given by

$$\lambda_{(\nu_I+b)}^{-1} = n_b \sigma_{(\nu_I+b)}, \quad (3.66)$$

for a process with baryonic target b and neutrino of flavor ν_I . The cross sections $\sigma_{\nu_I,b}$ are approximated by analytical formulas based on the local fluid density, energy, and composition.

The approximate emission rates and luminosities per baryon in the free-streaming regime, R_I^F and Q_I^F are also analytically and locally calculated and include the following neutrino-emission processes:

- (i) electron and positron captures

$$e^+ + n \rightarrow p + \bar{\nu}_e,$$

$$e^- + p \rightarrow n + \nu_e,$$

- (ii) electron-positron pair annihilation

$$e^+ + e^- \rightarrow \bar{\nu} + \nu,$$

- (iii) and plasmon decay

$$\gamma \rightarrow \bar{\nu} + \nu.$$

See Appendix A of [Galeazzi et al. \(2013\)](#), for the analytic formulas of the neutrino scattering and capture cross sections and emission rates. Finally, the effective rates R_I^{eff} and Q_I^{eff} are obtained via interpolation between the free streaming and the trapped regimes by

$$R_I^{\text{eff}} = R_I^F \left(1 + \frac{R_I^F}{R_I^D} \right)^{-1} \quad (3.67)$$

and the equivalent for Q_I^{eff} . The source terms R and Q in Eqs. (3.61) and (3.62) are then obtained via

$$R = R_{\nu_e}^{\text{eff}} - R_{\bar{\nu}_e}^{\text{eff}} \quad (3.68)$$

$$Q = Q_{\nu_e}^{\text{eff}} + Q_{\bar{\nu}_e}^{\text{eff}} + Q_{\nu_x}^{\text{eff}}. \quad (3.69)$$

3.3.2. M0 absorption scheme

The leakage scheme described above only treats the emission of neutrinos. However, outside of the disk and in the polar regions, of the remnant, neutrino absorption plays an important role (see, e.g., [Just et al., 2021](#)). For this reason, we employ a simple zeroth-moment (M0) transport scheme for free streaming neutrinos, detailed in Appendix A of [Radice et al. \(2016\)](#). Moment-based neutrino transport schemes are a popular method based on the expansion of the neutrino distribution functions angular dependence ([Thorne, 1981](#); [Shibata et al., 2011](#)).

The scheme tracks the neutrino number densities n_I and average energies in the fluid rest frame \mathcal{E}_I . The number current (i.e. the first moment of f) for a given neutrino flavor I is given by

$$J_I^\mu = \int f p^\mu \frac{d^3p}{-p_0}, \quad (3.70)$$

with $n_I = -u_\mu J_I^\mu$. Neglecting neutrino scattering, J_I^μ obeys the equation

$$\nabla_\mu J_I^\mu = R_I^{\text{eff}} - \kappa_I^{\text{a}} n_I. \quad (3.71)$$

Here R_I^{eff} are the effective emission rates obtained from the leakage scheme and κ_I^{a} are their absorption opacities. To close the scheme, we assume that the free-streaming neutrinos are streaming radially outwards in the fluids rest frame. Mathematically this is expressed as

$$J_I^\mu = n_I k^\mu = n_I (u^\mu + r^\mu), \quad (3.72)$$

where r^μ is a radial unit-vector orthogonal to the fluid four-velocity (i.e. $r^\mu u_\mu = 0$). Equation (3.72) can be solved together with approximate equations for the \mathcal{E}_I on a series of independent radial rays using a finite volume scheme. Subsequently, the source terms

$$R^{\text{abs}} = \kappa_{\nu_e}^{\text{a}} n_{\nu_e} - \kappa_{\bar{\nu}_e}^{\text{a}} n_{\bar{\nu}_e} \quad (3.73)$$

$$Q^{\text{abs}} = \kappa_{\nu_e}^{\text{a}} n_{\nu_e} E_{\nu_e} + \kappa_{\bar{\nu}_e}^{\text{a}} n_{\bar{\nu}_e} E_{\bar{\nu}_e} \quad (3.74)$$

are interpolated to the Cartesian grid and to numerical nodes where the average neutrino energies in the laboratory rest frame E_i are given by $\mathcal{E}_I = -E_I k_{\mu} t^\mu$.

3.4. Simulation setup

The simulations we employ to model BNS systems are carried out in the open-source framework of the EinsteinToolkit (ET) suite¹ ([Haas et al., 2020](#); [Löffler et al., 2012](#)), itself based on the Carpet computational toolkit ([Goodale et al., 2003](#)).

To handle general relativistic hydrodynamics we employ the open-source `WhiskyTHC`² code ([Radice & Rezzolla, 2012](#); [Radice et al., 2014a,b](#)). It solves Euler's equations for the balance of energy and momentum, coupled to conservation laws for the neutron and proton densities. Neutrino emission and absorption are modeled with a leakage ([Galeazzi et al., 2013](#); [Nielsen et al., 2014](#)) scheme and the so-called ‘‘M0’’ scheme of [Radice et al. \(2016\)](#), respectively. These are both ‘‘grey’’ (i.e. energy integrated) schemes evolving three neutrino species: electron

¹einstein toolkit.org

²whiskycode.org

neutrinos ν_e , electron antineutrinos $\bar{\nu}_e$ and heavy neutrinos ν_x , which accounts for all others (anti-) neutrino flavors. Furthermore, the MO scheme evolves the distribution function of neutrinos on a ray-by-ray grid, which we setup consisting of 2048 rays uniformly spaced in latitude and longitude with a radial resolution $\Delta r \approx 244$ m.

In our setup, WhiskyTHC employs a finite-volumes scheme for the discretization of the hydrodynamic quantities. The scheme reconstructs primitive variables with the fifth-order MP5 method (Suresh & Huynh, 1997), from which numerical fluxes are computed with the HLLE flux formula (Harten et al., 1983), augmented with a positivity-preserving flux limiter (Hu et al., 2013; Radice et al., 2014b) in order to handle the transition to vacuum regions (which we fill with an atmosphere of density $\rho_{\text{atmo}} \approx 1.24 \times 10^3 \text{ g cm}^{-3}$).

The hydrodynamics is coupled to a dynamically-evolved spacetime. Einstein’s equations are written in the BSSN formulation (Shibata & Nakamura, 1995; Baumgarte & Shapiro, 1998; Brown, 2009), and discretized with fourth-order finite-differences stencils by the McLachlan code (Brown et al., 2009). We furthermore choose the “1+log” and “Gamma-driver” gauge conditions (see, e.g., Baumgarte & Shapiro, 2021).

The time evolution is performed by the strong-stability-preserving RK3 integrator (Gottlieb & Shu, 1998) using a method-of-lines scheme. The time step is determined by the Courant–Friedrich–Lewy (CFL) criterion taking the speed of light as the maximum propagation speed. The CFL factor is chosen to be 0.15.

The mesh for our simulations is handled by the Carpet code (Schnetter et al., 2004), which employs a “moving boxes” Berger-Oliger adaptive mesh refinement (AMR) scheme (Berger & Oliger, 1984; Berger & Colella, 1989). We employ a Cartesian-coordinates computational domain made of 7 refinement levels. The resolution on the finest level is $0.128M_{\odot} \approx 189$ m and the full grid spans $1024M_{\odot} \approx 1512$ km in each direction. To reduce the computational cost, we only evolve the $z \geq 0$ part of the domain and impose reflecting boundary conditions at $z = 0$.

4. Impact of the equation of state in neutron star mergers

In studies of binary neutron star (BNS) mergers, the influence of the equation of state (EOS) on the dynamics is often correlated to a single quantity describing the EOS. Such quantities are for example the radius of a cold non-rotating neutron star (NS) of a specific mass or the (reduced) tidal deformability (see Section 2.4.3). These approaches encapsulate the stiffness of the EOS and have been successful in describing the peak frequencies of the post-merger gravitational wave (GW) emission, typically within a 10% error (Bauswein et al., 2012; Bauswein & Janka, 2012; Hotokezaka et al., 2013a; Takami et al., 2014, 2015; Rezzolla & Takami, 2016), as well as the threshold mass to prompt collapse (Margalit & Metzger, 2017; Rezzolla et al., 2018; Shibata et al., 2019; Most et al., 2020; Nathanail et al., 2021). Recently it has been extended to features of the remnant-disk system and the dynamical ejecta (see, e.g., Nedora et al., 2021c; Henkel et al., 2023). However, a single quantity can only be a first approximation of the full density dependence of the pressure.

The so-called nuclear matter properties offer a universally applicable and well-known description of the properties of any EOS close to saturation density. The expansion parameters which are important for the pressure of cold nuclear matter are the incompressibility K and the slope and curvature of the symmetry energy L (see Section 2.4.3 for an introduction). Furthermore, the effective mass m^* is important for the pressure at zero temperature as well as for the thermal pressure. See Section 2.4.4 for an overview of how m^* enters in Skyrme type and relativistic mean field models.

In this part of the thesis, we individually vary different nuclear matter properties in the EOS and perform three-dimensional BNSs merger simulations in full general relativity (GR). We explore their influence on the remnant structure, GW emission, and ejection of matter. To this end, we employ 8 EOS models created with the SROEOS code (Schneider et al., 2017, 2018), enabling us to selectively study the impact of the effective nucleon mass, the incompressibility parameter, the symmetry energy, and the saturation point. A similar approach was used in numerical simulations of supernovae (Schneider et al., 2019; Yasin et al., 2020). The results have been published in Jacobi et al. (2023). Section 4.1 introduces the basic properties of the EOS tables and BNS merger simulations and explains the post-processing techniques used to analyze them. The results of the simulations are reported in Sections 4.2 to 4.4, which describe the dynamics of the merger and post-merger phases, the post-merger gravitational wave emission, and the properties of the ejected material.

EOS	$\frac{m^*}{m_n}$	B [MeV]	K [MeV]	S_v [MeV]	L [MeV]	ρ_0 [$10^{14} \text{ g cm}^{-3}$]
LS175 [†]	1.0	16.0	175	29.3	73.7	2.57
LS220 [†]	1.0	16.0	220	29.3	73.7	2.57
LS255 [†]	1.0	16.0	255	29.3	73.7	2.57
$m_{0.8}^*$	0.8	16.0	220	29.3	79.3	2.57
m_S^*	0.634	16.0	220	29.3	86.5	2.57
$(m^*K)_S$	0.634	16.0	281	29.3	86.5	2.57
$(m^*KE_{\text{sym}})_S$	0.634	16.0	281	36.9	109.3	2.57
SkShen	0.634	16.3	281	36.9	109.4	2.41
Shen	0.634	16.3	281	36.9	110.8	2.41

Table 4.1.: Nuclear matter properties for all employed EOS tables. The nuclear matter parameters B , K , S_v , and L are given in MeV, the saturation density ρ_0 is given in g cm^{-3} .

4.1. Methods

4.1.1. Equation of state models

To explore the impact of specific nuclear matter properties, we use the open-source SROEOS code (Schneider et al., 2017, 2018), which is based on a liquid droplet model with Skyrme-type nucleon-nucleon interactions as given in Eq. (2.21). To describe the density dependence of m^* , we use the prescription of Lattimer et al. (1985), given by

$$\frac{1}{2m^*} = \frac{1}{2m} + \alpha n, \quad (4.1)$$

where α is a free model parameter. By adjusting the 4 Skyrme parameters we can systematically vary B , K , S_v , and n_0 . The slope of the symmetry energy L , as well as higher-order contributions to the symmetry energy, can not be varied independently this way. Instead, by fixing the zeroth order contribution S_v , the full symmetry energy E_{sym} is varied, including higher order terms. Finally, we adjust the effective mass m^* at saturation density by changing α .

The expansion parameters, which are most important for the pressure inside NSs are the incompressibility K and the effective mass m^* . The effective mass also determines the thermal contribution. The L parameter (and higher-order contributions to the symmetry energy) also affects the pressure. However, since we can not vary it independently, we focus only on K and m^* . Moreover, Most & Raithel (2021) recently investigated the role of the L parameter in BNS mergers. To explore the impact of these parameters we use nine EOS tables. Eight of the tables were created with the SROEOS code, six of which were first used in Yasin et al. (2020) while two are newly calculated by Sabrina Huth specifically for this work. Finally, the ninth EOS is the classical Shen EOS (Shen et al., 1998b) Their nuclear matter properties are summarized in Table 4.1. With each of these EOS, we systematically vary one nuclear matter property at a time.

Following Yasin et al. (2020), we use the table LS220[†] as the fiducial model which is based on the same Skyrme parametrization as the LS220 EOS. Its incompressibility parameter is $K = 220 \text{ MeV}$ and its effective mass is not density-dependent and simply given by the neutron mass $m^* = m_n = 939.5654 \text{ MeV}$. First, we vary the K parameter to 175 and 255 MeV, resulting

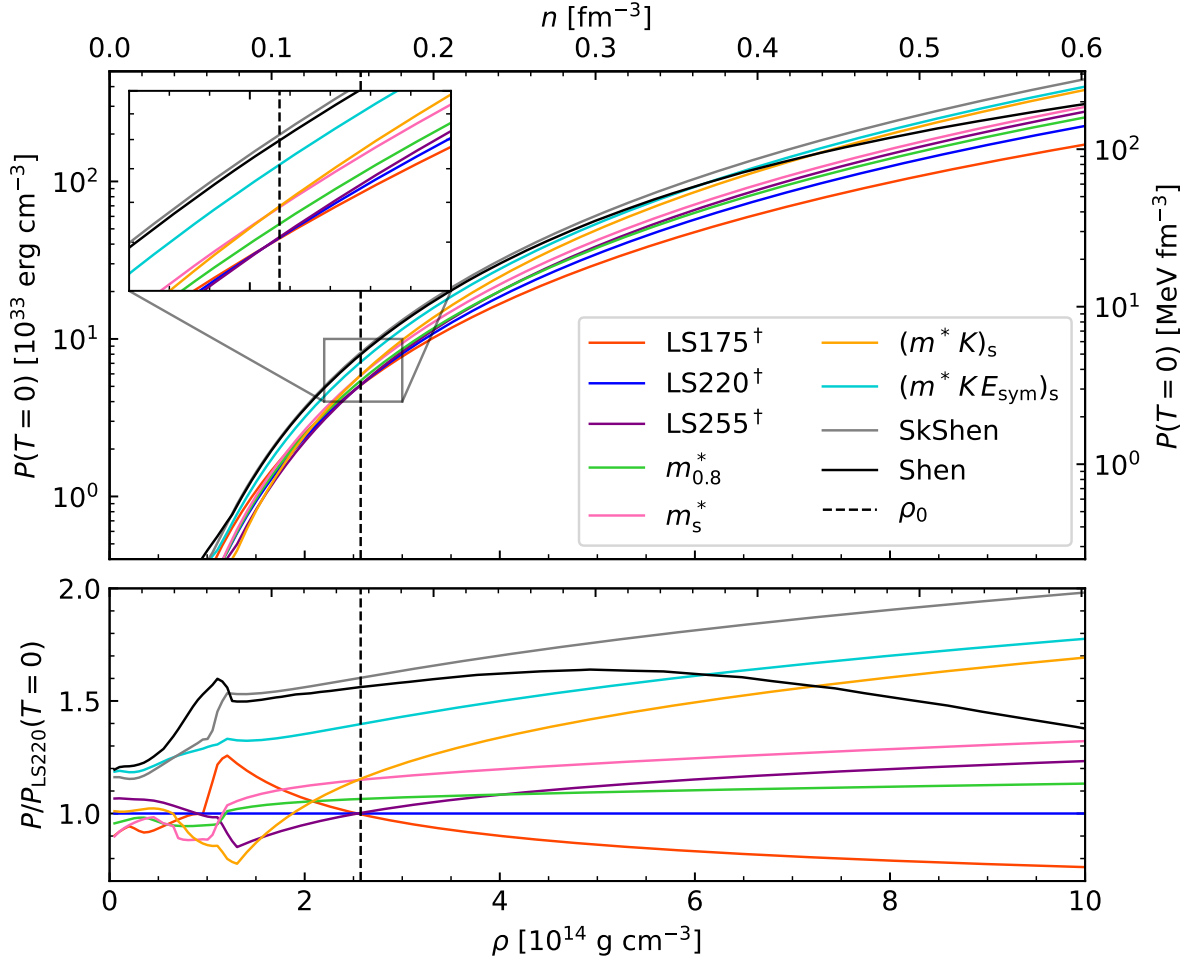


Figure 4.1.: Pressure versus density at $T = 0$ and $Y_e = 0.1$ for the EOS used in this thesis. The lower panel shows the curves normalized to the pressure in the fiducial model LS220[†] for comparison.

in the EOS LS175[†] and LS255[†], respectively. These values represent the upper and lower bounds predicted by chiral effective field theory calculations (Hebeler et al., 2011; Drischler et al., 2016, 2019). Second, we change the effective nucleon mass at saturation density to $m^* = 0.8m_n$ ($m_{0.8}^*$) and $m^* = 0.634m_n$ (m_s^*). The choice of $m^* = 0.634m_n$ is motivated by the Shen EOS. Finally, starting from m_s^* , we also change the remaining nuclear matter properties to match the values of the Shen EOS, starting with $K = 281$ MeV, followed by the symmetry energy $E_{\text{sym}} = 36.9$ MeV, and finally also the value of the saturation density $\rho_0 = 2.43 \times 10^{14} \text{ g cm}^{-3}$ and the binding energy $B = 16.3$ MeV. This results in the EOS $(m^*K)_s$, $(m^*KE_{\text{sym}})_s$, and SkShen. We also include the original Shen EOS for comparison.

Figure 4.1 shows the pressure versus density at $T = 0$ and $Y_e = 0.1$ for all the employed EOS. The pressure is given by the derivative of the energy density with respect to the particle density. Therefore, the incompressibility is related to the slope of the pressure at zero temperature (see Eq. (2.18)). Increasing K leads to larger pressure at densities above ρ_0 , but also smaller

pressures below ρ_0 (compare LS175[†], LS220[†], and LS255[†] in Fig. 4.1). Changing the symmetry energy also changes the slope parameter L , which enters the pressure in a density-independent term (see Eq. (2.20)). Thus it has a relatively large effect close to saturation density but smaller at higher densities (compare $(m^*K)_S$ and $(m^*K E_{\text{sym}})_S$ in Fig. 4.1).

Finally, the effective mass influences the degeneracy pressure which is given by (Lattimer & Swesty, 1991)

$$P(T=0) = \sum_t \left(\frac{5}{3} \frac{1}{2m^*} - \frac{1}{2m} \right) \tau_t(T=0) + P_{\text{int}} \quad (4.2)$$

where P_{int} is the pressure due to the interaction terms and $\tau_t(T=0)$ is given by the Fermi momentum (see Eq. (2.22)). Since the effective mass enters inversely in Eq. (4.2), decreasing the effective mass increases the cold pressure. The effect is significant over the full range of densities in the NS ($\rho > 10^{14} \text{ g cm}^{-3}$) and increases slightly towards higher densities (compare LS220[†], $m_{0.8}^*$, and m_S^* in Fig. 4.1).

In addition to the cold pressure, the high-density EOS depends on the temperature. This dependence is often described by the thermal index Γ_{th} given by (see, e.g., Bauswein et al., 2010)

$$\Gamma_{\text{th}} := 1 + \frac{P_{\text{th}}}{\epsilon_{\text{th}}} = 1 + \frac{P - P_{\text{cold}}}{\rho(\epsilon - \epsilon_{\text{cold}})}, \quad (4.3)$$

where $\epsilon_{\text{th}} = \rho \epsilon_{\text{th}}$ is the thermal internal energy density. The subscript cold refers to the values at zero temperature, which are obtained from the EOS. For a non-interacting gas of non-relativistic fermions, the thermal index is determined by the density dependence of the effective mass (see, e.g., Constantinou et al., 2015; Lattimer & Prakash, 2016):

$$\Gamma_{\text{th}} = \frac{5}{3} - \frac{n}{m^*} \frac{\partial m^*}{\partial n}, \quad (4.4)$$

Chiral effective field theory calculations have found this to be a good approximation for the thermal index. Several previous works investigated thermal effects in binary compact object mergers in isolation by changing the thermal pressure independently from the cold EOS (see, e.g., Bauswein et al., 2010; Hotokezaka et al., 2013b; Raithel et al., 2021). However, by changing the effective mass, we vary the temperature dependence of the EOS while also changing the cold pressure. In Fig. 4.2, the thermal index inside the NSs is shown versus density for the three values of the effective mass used in our simulations. Due to the parametrization of the effective mass (Eq. (4.1)), lowering the effective mass at saturation density increases the thermal index. However, it should be noted that recent results from chiral effective field theory imply that the thermal index might decrease with rising density (Carbone & Schwenk, 2019; Keller et al., 2021).

Figure 4.3 shows the TOV mass-radius relation for all of the EOS. As described above, the influence of changing the incompressibility mostly influences the pressure at densities close to n_0 which translates to a large influence in the radius of NSs with high masses (compare LS175[†], LS220[†], and LS255[†] or m_S^* and $(m^*K)_S$ in Fig. 4.3). Varying the symmetry energy mostly changes the pressure close to saturation density and thus has a large effect on the radii of low mass NSs. The effective mass impacts intermediate to high mass NSs but has less of an effect at high masses compared to the incompressibility. The radii of NS with a mass of $1.365M_{\odot}$ are marked by solid circles. These are the radii of the NSs in the initial data of the simulations (see Section 4.1.2).

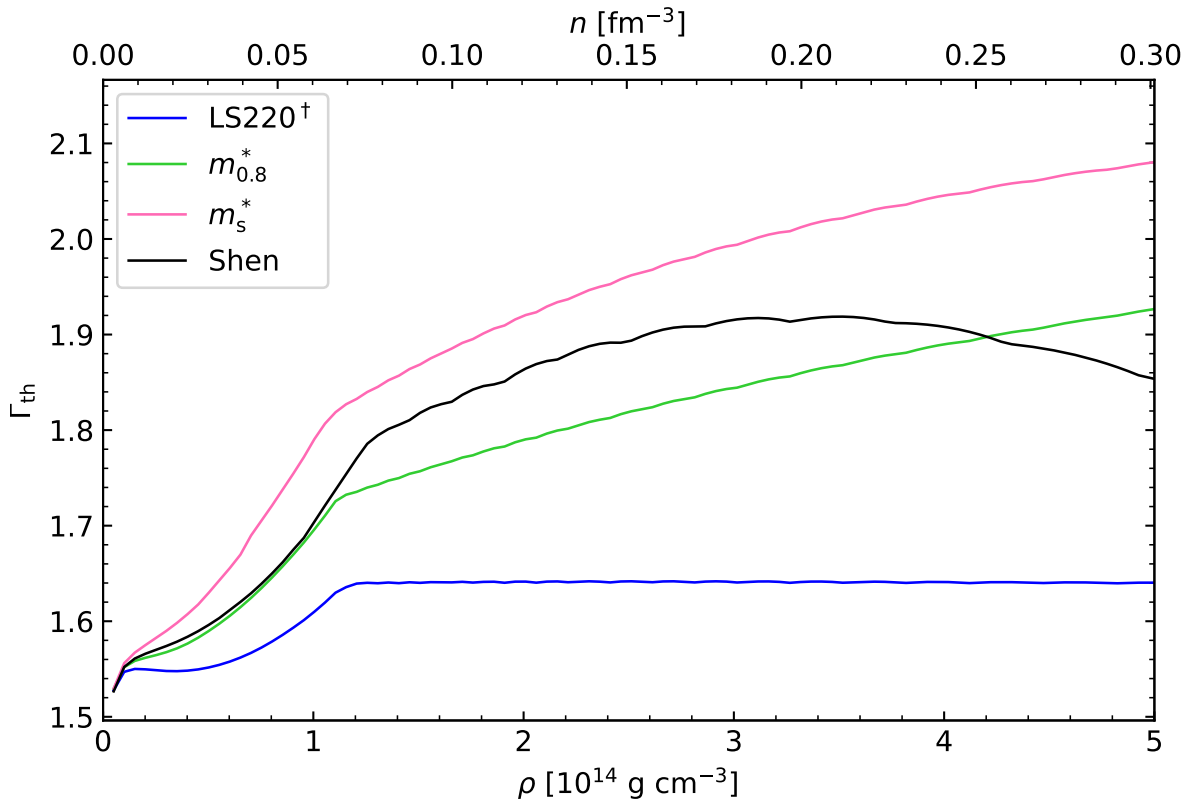


Figure 4.2.: Thermal index Γ_{th} for LS220^\dagger , $m_{0.8}^*$, and m_s^* . The black line shows the thermal index for the Shen EOS. Though the value of the effective mass at saturation density is the same as in m_s^* , the thermal index is different due to the different implementations of the microphysics.

4.1.2. Simulation overview

We perform one simulation for each EOS in Table 4.1. Each model initially consists of two irrotational identical $M = 1.364M_\odot$ NSs on quasi-circular orbits with an initial separation of 45 km. This combination corresponds to a chirp mass of $1.188M_\odot$ and is thus compatible with the GW source of GW170817. This orbital separation corresponds to an inspiral phase of 2 – 3 orbits before the merger. The initial data for all the selected simulations are constructed using the spectral elliptic solver LORENE (Gourgoulhon et al., 2001). In the construction of the initial data, the minimum temperature slice of the EOS table is used and the composition is determined by the neutrinoless beta-equilibrium.

An overview of the simulations is compiled in Table 4.2. Each simulation is run for at least 40 ms post-merger. The only exceptions are the models LS175^\dagger and LS220^\dagger . In LS175^\dagger a BH is formed almost immediately after the merger so barely any mass is ejected. In LS220^\dagger the remnant collapses after ~ 8 ms which is enough time to eject matter and form an accretion disk. However, the mass ejection and GW emission stop completely after 30 ms. In all other models, the remnant is a massive NS which stays stable for the duration of the simulation and is surrounded by an accretion disk.

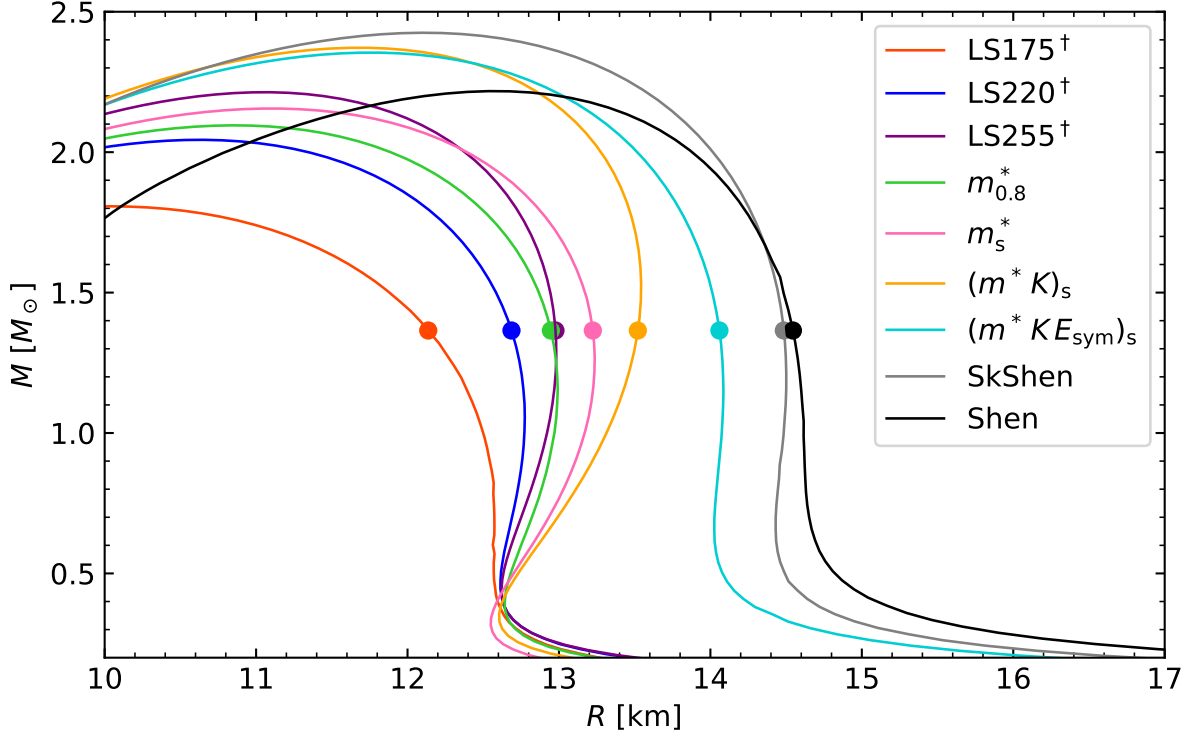


Figure 4.3.: The mas-radius relation of cold non-rotating NSs for the EOS used in this thesis. The circles mark the radii of the NSs in the initial data for the simulations.

4.1.3. Postprocessing methods

We define the NS as the region where the rest mass density is larger than $10^{13} \text{ g cm}^{-3}$. Since the gauge is evolved dynamically during the simulation we need to compare simulation data in a gauge-independent way. For this, we divide all grid cells in a snapshot of a simulation into 100 uniformly spaced density bins up to $10^{15} \text{ g cm}^{-3}$. The quantity of interest A is then averaged in each bin, weighted by the conserved rest mass density D :

$$|A|_{\rho} = \frac{\int_{\rho_{\text{bin}}} AD \, d^3x}{\int_{\rho_{\text{bin}}} D \, d^3x}, \quad (4.5)$$

where ρ is the rest mass density of the bin and $\int_{\rho_{\text{bin}}}$ indicates the integral over all cells in the density bin.

Furthermore, we make use of the complex azimuthal mode decomposition given by (Paschalidis et al., 2015; East et al., 2016a,b; Radice et al., 2016; Nedora et al., 2021b)

$$C_m = \int D e^{-im\phi} \, dx dy \quad (4.6)$$

to study the deformation of the remnant.

We extract ejecta properties on a detection sphere with a 300 km coordinate radius. The Bernoulli criterion is used to determine whether a fluid element is unbound. It is defined by $-hu_t > h_{\infty}$, where $h_{\infty} = \lim_{\rho, T \rightarrow 0} h$ is the asymptotic specific enthalpy (Foucart et al. (2021)).

EOS	t_{BH} [ms]	t_{end} [ms]	M_{disk} [M_{\odot}]	f_1 [kHz]	f_2 [kHz]	R_{NS} [km]	$\tilde{\Lambda}$
LS175 [†]	0.46	0.67	-	0.00	0.00	12.16	361.03
LS220 [†]	8.03	33.06	0.05	2.14	3.08	12.69	606.15
LS255 [†]	-	42.87	0.23	2.01	2.64	12.98	660.69
$m_{0.8}^*$	-	44.94	0.14	1.87	2.82	12.95	699.63
m_{S}^*	-	46.96	0.23	1.90	2.53	13.23	759.28
$(m^*K)_{\text{S}}$	-	49.05	0.26	1.79	2.41	13.52	982.63
$(m^*K E_{\text{sym}})_{\text{S}}$	-	47.45	0.23	1.72	2.30	14.06	1090.64
SkShen	-	54.09	0.23	1.66	2.25	14.49	1295.42
Shen	-	55.32	0.24	1.68	2.24	14.55	1221.11

Table 4.2.: Overview of all models and their key results, including the simulated time t_{end} , time until collapse to a black hole (BH) t_{BH} , disk mass at the end of the simulation M_{disk} , frequencies of the two most prominent peaks in the post-merger GW spectrum f_1 and f_2 , and radius R_{NS} and reduced tidal deformability $\tilde{\Lambda}$ of the NSs in the initial data of our simulations.

Accordingly, the asymptotic velocity of an ejected fluid element is defined as $v_{\infty} = \sqrt{1 - \left(\frac{h_{\infty}}{hu_t}\right)^2}$. This criterion is less restrictive than the geodesic criterion $-u_t > 1$, which does not take the ejecta’s thermal and binding energy into account. Typically, the ejection rate of matter meeting the geodesic criterion stops after ~ 10 ms post-merger and roughly corresponds to the fluid elements ejected by dynamical processes (see Section 4.3 for further discussion). We use the geodesic criterion to separate dynamic and disk wind ejecta. Following [Nedora et al. \(2021b\)](#); [Combi & Siegel \(2023\)](#), we define fluid elements fulfilling the geodesic criterion as dynamical ejecta. Ejecta that only satisfy the Bernoulli, but not the geodesic criterion are defined as disk ejecta. For an in-depth discussion of different ejection criteria and their impact see, e.g., [Foucart et al. \(2021\)](#).

4.2. Merger and post-merger dynamics

The remnant dynamics depend sensitively on the EOS due to multiple effects. In the following section, we describe the dynamics of the merger and post-merger and point out where and how the EOS affects the dynamics. During the merger, two effects are responsible for the ejection of matter and disk formation: Shocks originating at the contact interface of the NSs and tidal disruption on the opposite side. However, these two effects depend differently on the EOS.

Already before the merger, the structure of the initial BNSs is determined by the EOS. Stiffer EOS (for example due to a larger K , larger E_{sym} or smaller m^*) lead to larger NS radii (see Fig. 4.3) and therefore an earlier merger because the NSs come into contact at larger separations ([Radice et al., 2020](#)) and with smaller velocities. Directly after the merger, the two NS cores bounce and begin to oscillate against each other in the newly formed remnant. With a stiffer EOS, the contraction is halted earlier and the oscillation amplitude is smaller. Both effects lead to a more violent merger for softer EOS and have a large impact on the disk formation and amount of ejected material due to shock heating ([Hotokezaka et al., 2013b](#)).

The response of the BNSs to tidal deformation depends on the NS structure and thus on the cold EOS. Generally, large NSs have a larger tidal deformability, but the incompressibility parameter plays a particularly important role. Larger incompressibilities lead to a steeper pressure-density curve (see Fig. 4.1). Therefore, the maximum density in the NS is reduced but at the same time, the density in the outer layers is increased. This effect can be seen by comparing the NSs in the initial data of LS255[†] and $m_{0.8}^*$ because they have almost identical radii (see Fig. 4.3). Figure 4.4 shows their spatial mass distribution $\frac{dM}{dr} = 4\pi\rho r^2$ versus the radius. Due to the higher incompressibility of LS255[†], more mass is located at larger radii. As

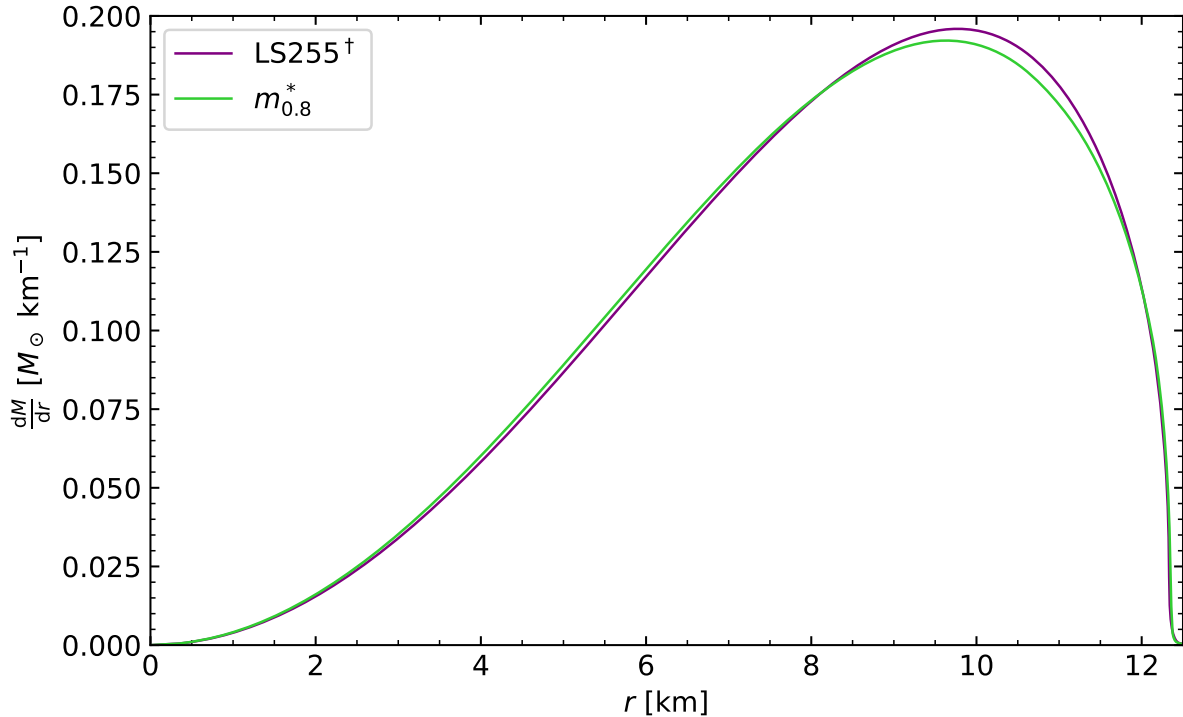


Figure 4.4.: Spatial mass distribution in the initial NSs in LS255[†] and $m_{0.8}^*$. Due to the higher incompressibility of LS255[†], more mass is located at larger radii.

we will see in Section 4.3, this leads to a more massive tidal ejecta component.

Whether the remnant collapses is determined by the initial masses of the NSs and the EOS. As the two cores of the original NSs combine after the merger, the remnant's central density and pressure rise. This process is either halted when the pressure becomes high enough to balance the NS' self-gravity, in which case a semi-stable NS remains in the center, or the contraction continues until the formation of a BH. The duration of the gravitational contraction changes depending on the slope of the pressure with respect to the density, i.e., the incompressibility. If central pressure rises only slowly with the density, the central density keeps increasing for longer before the contraction is halted. On the other hand, if the pressure-density gradient is steep, the contraction is halted sooner. Therefore, smaller incompressibilities lead to lower threshold masses and shorter delays until the collapse of hyper-massive NSs (HMNSs).

During this initial phase of contraction, the remnant is highly deformed and oscillates, where the dominant deformation mode being a $m = 2$ bar-shaped deformation. However, after

some time the $m = 1$ deformation can become relevant for gravitational wave emission, disk formation, and matter ejection (Bernuzzi et al., 2014; Kastaun & Galeazzi, 2015; Paschalidis et al., 2015; East et al., 2016a,b; Lehner et al., 2016; Radice et al., 2016; Nedora et al., 2019, 2021b). When this transition occurs, depends on the complicated non-linear oscillations of the remnant NS, which are determined by the EOS. As we will see in the next section, the transition from a dominant $m = 2$ to a dominant $m = 1$ mode might be connected to the pressure-density, i.e., the incompressibility.

During the merger, the initially cold NS matter is heated to $\sim 10 - 100$ MeV by shocks originating from the interface of the collision. The high-density NS cores remain comparatively cool because the shocks do not penetrate them. As the colder cores merge, the hot matter is redistributed into a ring shape at densities of approximately $1 - 5 \times 10^{14} \text{ g cm}^{-3}$. This evolution can be seen in Fig. 4.5, which shows temperature profiles inside the remnant in $m_{0.8}^*$ at approximately 0.5, 3, and 10 ms post-merger. Because the center of the NS is cold and

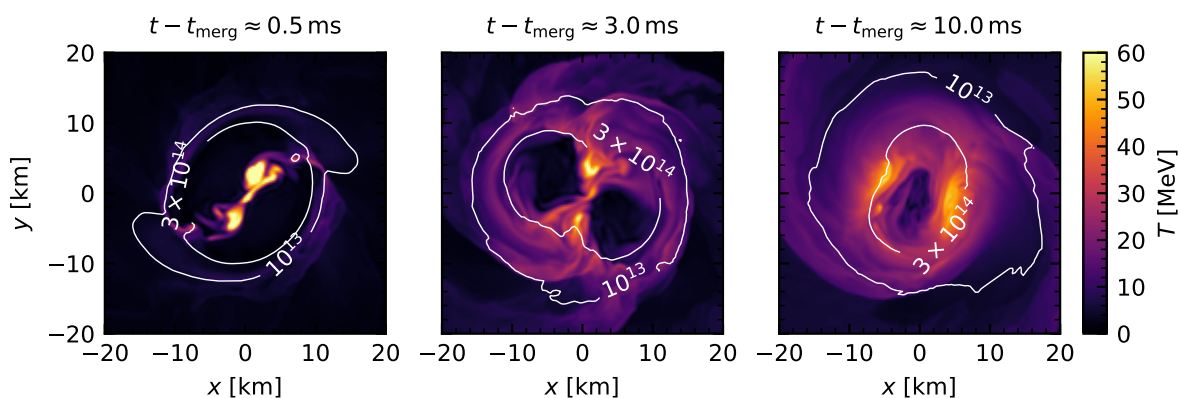


Figure 4.5.: Temperature profiles inside the remnant in $m_{0.8}^*$ at approximately 0.5, 3, and 10 ms post-merger. Density contours of 10^{13} , 10^{14} , and $5 \times 10^{14} \text{ g cm}^{-3}$ are show in white.

very dense, the cold pressure dominates and thermal contributions to the pressure are not relevant in this region. However, the thermal pressure plays a significant role in the hot ring close to saturation density and even becomes larger than the cold pressure in the outer layers of the NS as can be seen in Fig. 4.6. Thermal effects are therefore especially important for disk formation and matter ejection but their impact on the post-merger gravitational wave emission is small (see, e.g., Bauswein et al., 2010; Hotokezaka et al., 2013a). Hotokezaka et al. (2013b) found competing effects of the thermal index on the amount of mass ejection: On one hand, larger values of Γ_{th} increase the effectiveness of shock heating, resulting in more shock-heated ejecta. On the other hand, higher thermal pressures result in a less compact remnant which is therefore rotating slower. This reduces the torque exerted from the NS on the disk and consequently the amount of ejecta from the early remnant-disk system. By varying the effective mass, we change both the cold and the thermal pressure. Therefore, the explicit effect of changing the thermal index can not be observed independently in our simulations.

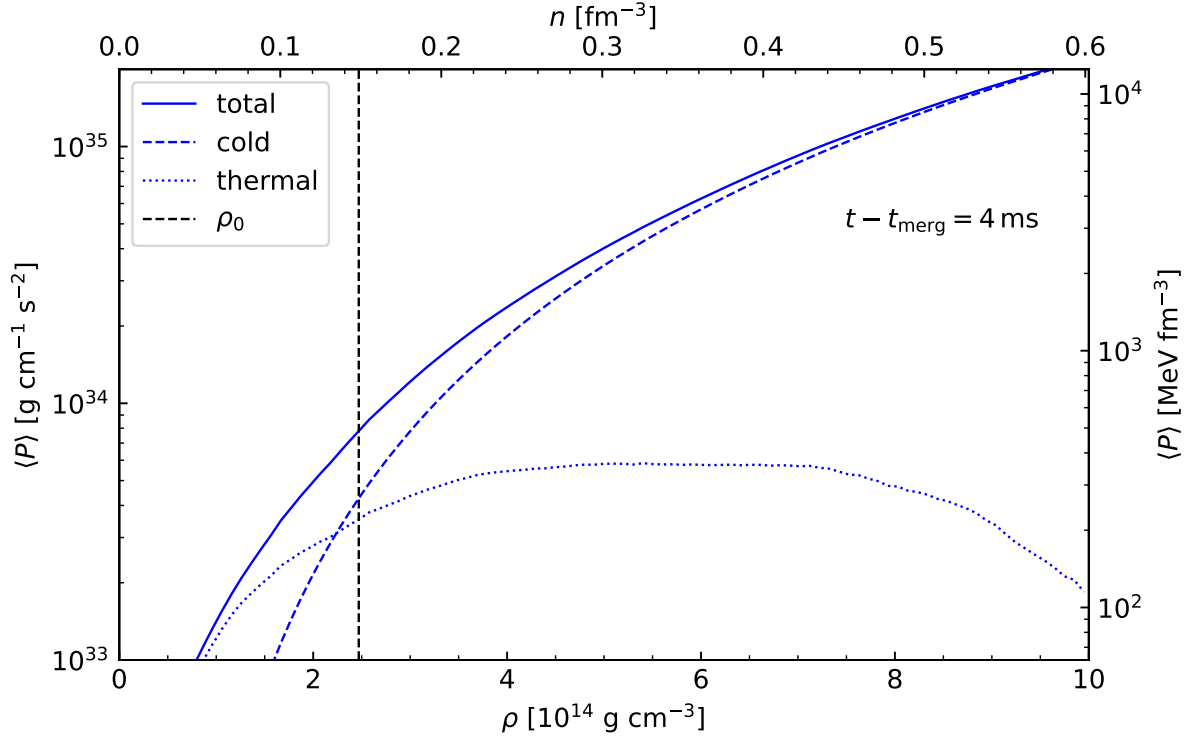


Figure 4.6.: Average thermal, cold, and total pressure for LS220[†], roughly 4 ms after the merger. The thermal contributions to the pressure become relevant close to the saturation density.

4.2.1. Comparison of different effective masses and incompressibilities

First, we compare the fiducial model LS220[†] with the simulations based on variations of the effective nucleon mass m^* (m_s^* and $m_{0.8}^*$) and incompressibility K (LS255[†] and LS175[†]). The time evolution of the maximum density inside the NS is shown in Fig. 4.7. The massive NS is initially in a highly deformed state and oscillating, as seen in the maximum density. For LS220[†], several bounces occur with increasing amplitude before the central object collapses to a BH, at roughly 8 ms after the merger. In the model LS175[†], a BH is formed immediately after the merger due to the lower pressure at high density. If the pressure in the center of the NS is large enough to stop the contraction of the remnant before collapse, the oscillation of the massive NS dies down after approximately 10 - 20 ms as the newly formed remnant settles into a more axisymmetric configuration. Both decreasing the effective mass (e.g., $m_{0.8}^*$) or increasing the incompressibility (LS255[†]) leads to this outcome. In general, the final central density is larger for EOS with lower pressures at high density.

The initial NSs in LS255[†] and $m_{0.8}^*$ have almost the same radius and tidal deformability (see Table 4.1). This leads to almost identical NS velocities at the merger and consequently, their initial bounce and the early evolution of their central densities are qualitatively very similar. However, the dependency of the pressure on density is steeper in LS255[†], due to the higher incompressibility. Therefore, the contraction of the NS stops already after ~ 10 ms, while the central density in $m_{0.8}^*$ keeps rising for longer. In Fig. 4.8, the $m = 1$ and 2 deformation

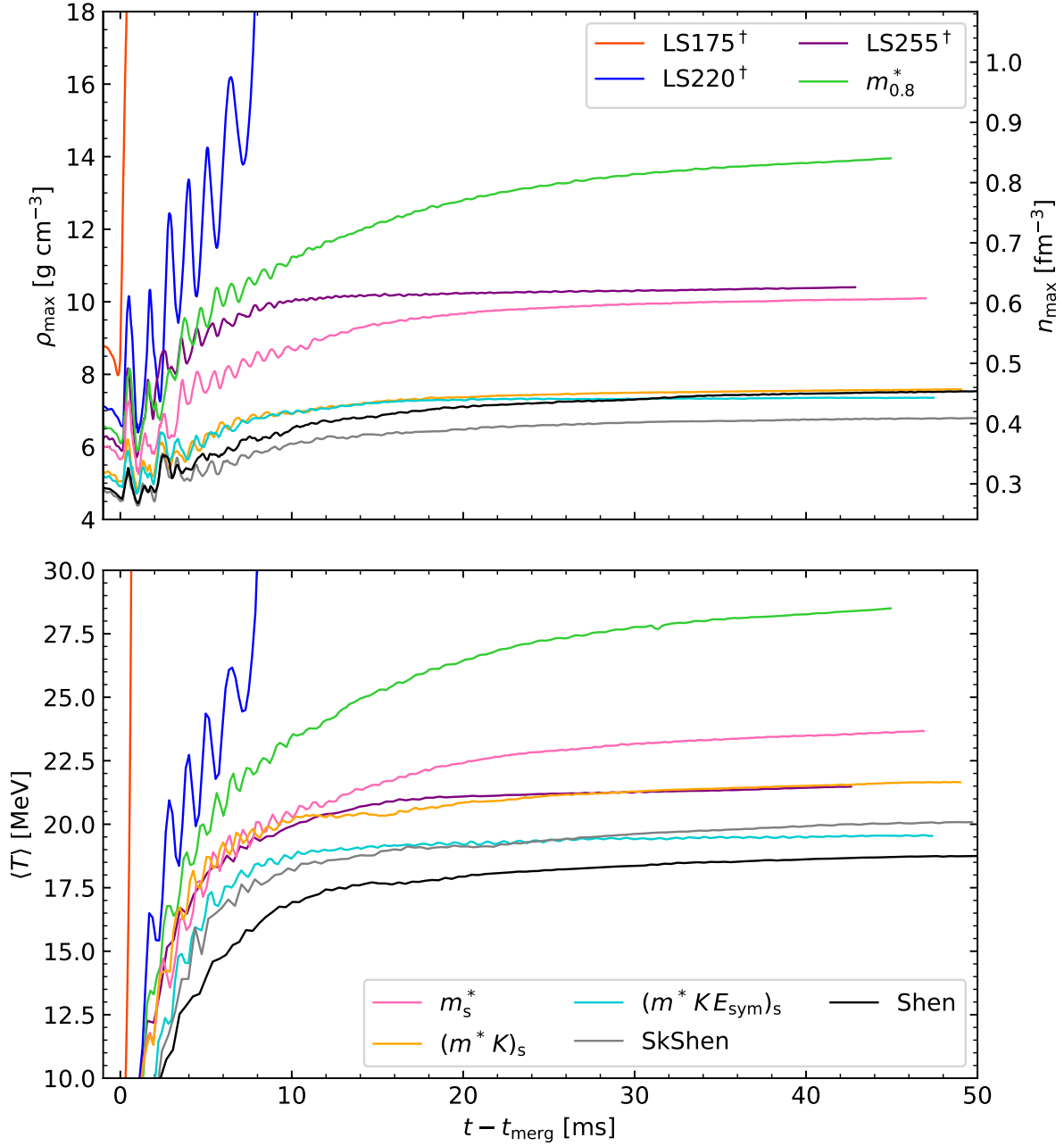


Figure 4.7.: Maximum density (upper panel) and average remnant temperature (lower panel) versus time.

calculated with Eq. (4.6) is shown. All models undergo the change from a dominating $m=2$ to a dominant $m=1$ mode at different times. In LS255[†], $(m^* K)_s$, and $(m^* K E_{\text{sym}})_s$, the transition occurs already after roughly 9, 15, and 17 ms, respectively, which is significantly earlier compared to the other models. This could also be an effect of the steep pressure-density gradient due to the higher incompressibilities. The $m = 2$ deformation of the NS is the most

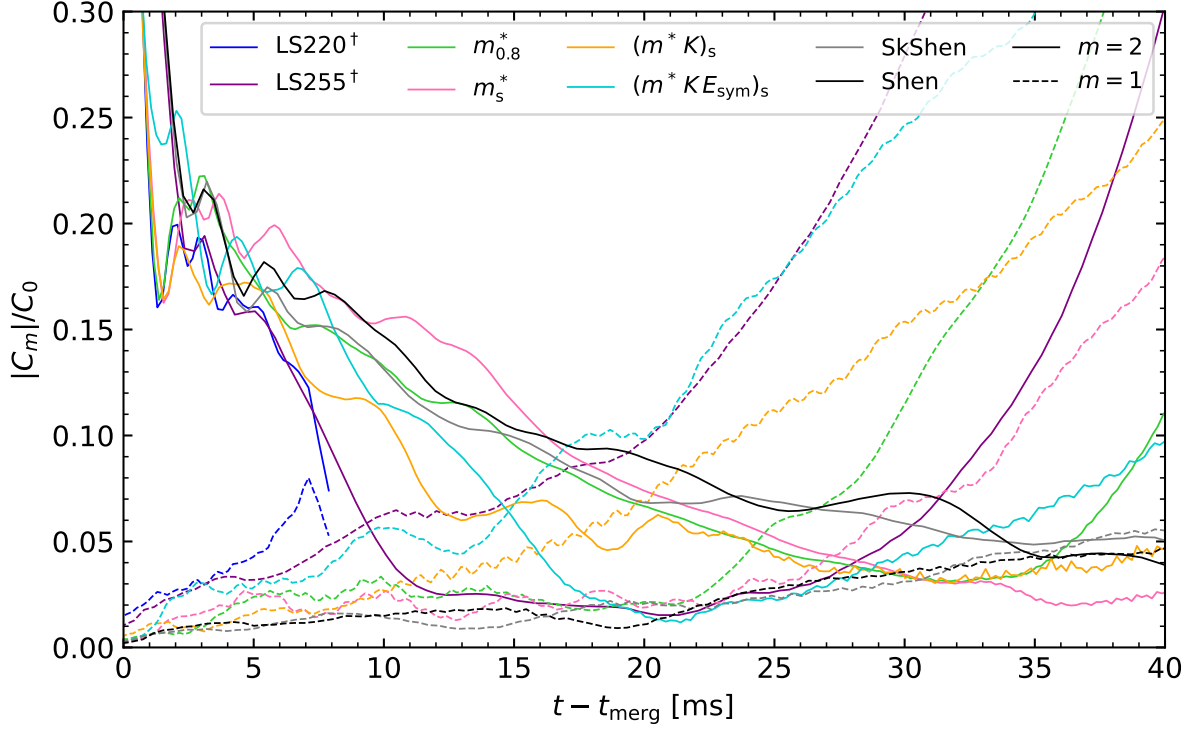


Figure 4.8.: Complex azimuthal $m = 1$ and 2 decomposition of the density in the xy -plane calculated with Eq. (4.6). Solid and dashed lines correspond to the $m = 2$ and $m = 1$ modes, respectively. The transition to a dominant $m = 1$ mode happens first for LS175[†], followed by $(m^* KE_{\text{sym}})_s$, and $(m^* K)_s$.

efficient source of post-merger GW emission (see Section 4.4).

The lower panel of Fig. 4.7 shows the evolution of the average temperature inside the remnant as a function of time. In LS220[†] the remnant is heated up much more than in the non-collapsing cases due to the increasingly violent oscillations. Non-collapsing remnants with larger maximum densities generally also have larger temperatures because stiffer EOS result in a less violent merger and reduced shock heating. However, the models with smaller effective mass show a deviation from this trend, as can be seen by comparing LS255[†] and m_s^* . The LS255[†] EOS exhibits lower pressures for all densities compared to m_s^* (see Fig. 4.1). Therefore, the central density in LS255[†] is higher than in m_s^* . Nonetheless, its average remnant temperature is lower. This is because the thermal index Γ_{th} is larger in the simulations with lower effective mass which increases the shock heating efficiency (Hotkezaka et al., 2013b).

Figure 4.9 shows the average temperature (upper panel) and thermal pressure (lower panel) versus density inside the remnant 4 ms after the merger. Since the EOS exhibit different thermal indices, the thermal pressure is not always higher for hotter remnants. This effect can be seen by comparing $m_{0.8}^*$ and LS255[†], which have comparable temperature profiles. However, the thermal pressure in $m_{0.8}^*$ is $\sim 25\%$ higher than in LS255[†], because $m_{0.8}^*$ has a smaller effective mass. Therefore, lowering the effective mass has two competing effects on the thermal pressure of the remnant. On one hand, the thermal pressure is increased due to the influence of the effective mass on the thermal index. On the other hand, lowering the effective masses reduces

the cold pressure which results in reduced shock heating and consequently lower temperatures and thermal pressures. Figure 4.9 shows that the second effect is stronger, i.e., reducing m^* generally results in a lower thermal pressure. Note, however, that this result might change if the density dependence of effective mass is different from Eq. (4.1).

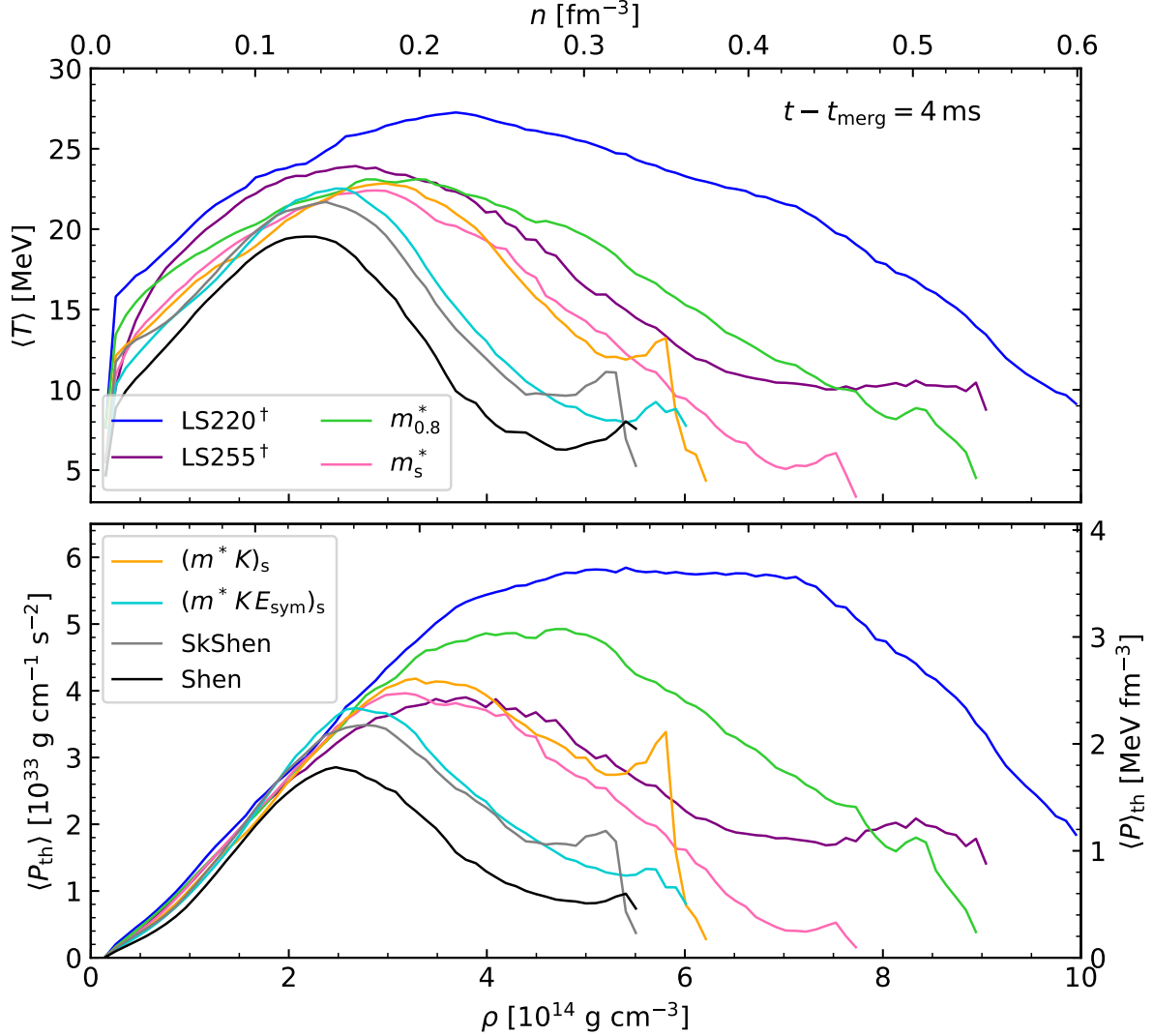


Figure 4.9.: The average thermal pressure (upper panel) and temperature (lower panel) versus density inside the NS approximately 4 ms after the merger. The cells are sorted into density bins and for each bin, the mass-weighted average of the pressure or temperature is calculated according to Eq. (4.5).

4.2.2. Comparison of Shen and SkShen

Next, we change nuclear matter properties to the values of the Shen EOS (Shen et al., 1998a) in multiple steps. We start with the effective mass (m_s^*) and change the incompressibility

$((m^*K)_S)$, the symmetry energy $((m^*KE_{\text{sym}})_S)$, and finally also the binding energy and saturation density (SkShen). By comparing the simulation results EOS we can evaluate the importance of the changed parameters.

Due to the increased incompressibility the cold pressure in $(m^*K)_S$ is larger than m_S^* above saturation density but lower below saturation density (see Fig. 4.1). Similar to LS255[†] this results in a significantly lower central density. Furthermore, the steeper density dependence of the pressure in $(m^*K)_S$ results in a faster decrease in the oscillations, and thus the average temperature in the remnant stays lower than in m_S^* after ~ 10 ms.

The EOS $(m^*K)_S$ and $(m^*KE_{\text{sym}})_S$ differ only in the symmetry energy. Increasing the symmetry energy also increases the slope of the symmetry energy L (see Table 4.1), and therefore the pressure. Comparing the cold pressure in $(m^*K)_S$ and $(m^*KE_{\text{sym}})_S$ in Fig. 4.1 shows that the effect is small in the center of the remnant but becomes large at low densities ($\rho \lesssim 2 \times 10^{14} \text{ g cm}^{-3}$). Thus, the density in the core of the NSs in $(m^*KE_{\text{sym}})_S$ and $(m^*K)_S$ is almost the same. The time evolution of the average remnant temperature (Fig. 4.7), shows that the temperature in $(m^*KE_{\text{sym}})_S$ is smaller than in $(m^*K)_S$. This is due to the larger pressure at lower densities in $(m^*KE_{\text{sym}})_S$, which results in reduced shock heating at the merger.

Also changing the binding energy and saturation density results in the model SkShen. The cold pressure in SkShen is roughly 10% to 15% higher compared to $(m^*KE_{\text{sym}})_S$ (see Fig. 4.1) which results in a slightly lower central density.

SkShen and the original Shen EOS are as close as possible in terms of their nuclear matter properties at saturation density. However, there are some differences between them. First, the cold pressure in SkShen is larger at high densities. The reason for the considerable difference is that the nuclear matter properties are an expansion around saturation density. Thus, close to the saturation density, the pressure is similar in both EOS, but it diverges at larger densities. Second, the thermal index of the Shen EOS is lower compared to SkShen, even though it is almost exactly the same in all four SROEOS models that use the Shen effective mass value. This is expected because, as explained in Section 4.2.1, matching the effective mass at saturation density does not reproduce the thermal index if the density dependence of the effective mass is different. Due to the increased pressure at high densities, the central density in the model Shen is larger than in SkShen. The average remnant temperature, however, is larger in SkShen because it has a larger thermal index, resulting in more effective shock heating (Hotokezaka et al., 2013b). Considering the large deviation in Fig. 4.1 the evolutions of the remnants in the models SkShen and Shen are remarkably similar.

4.2.3. Accretion disk structure

Figure 4.10 shows the evolution of the disk mass for all simulations except LS175[†]. The disk mass is defined as the total rest mass outside of the NS, i.e., the region with $\rho < \rho_{\text{NS}} = 10^{13} \text{ g cm}^{-3}$. The disk masses at the end of the simulations are listed in Table 4.2. We note that the hierarchy of the disk masses depends on the definition of the NS surface because a large fraction of the disk mass is located in the transition region between the disk and NS. To illustrate this effect, we show the disk masses for the definition $\rho < 10^{12} \text{ g cm}^{-3}$ as the dotted lines in Fig. 4.10. This has a larger effect on the disk masses of the simulations with larger incompressibility, i.e., LS255[†], $(m^*K)_S$, and $(m^*KE_{\text{sym}})_S$.

The formation of the accretion disk depends on the EOS properties due to multiple effects: The most important factor for the disk mass is the fate of the merger remnant. In LS175[†], the

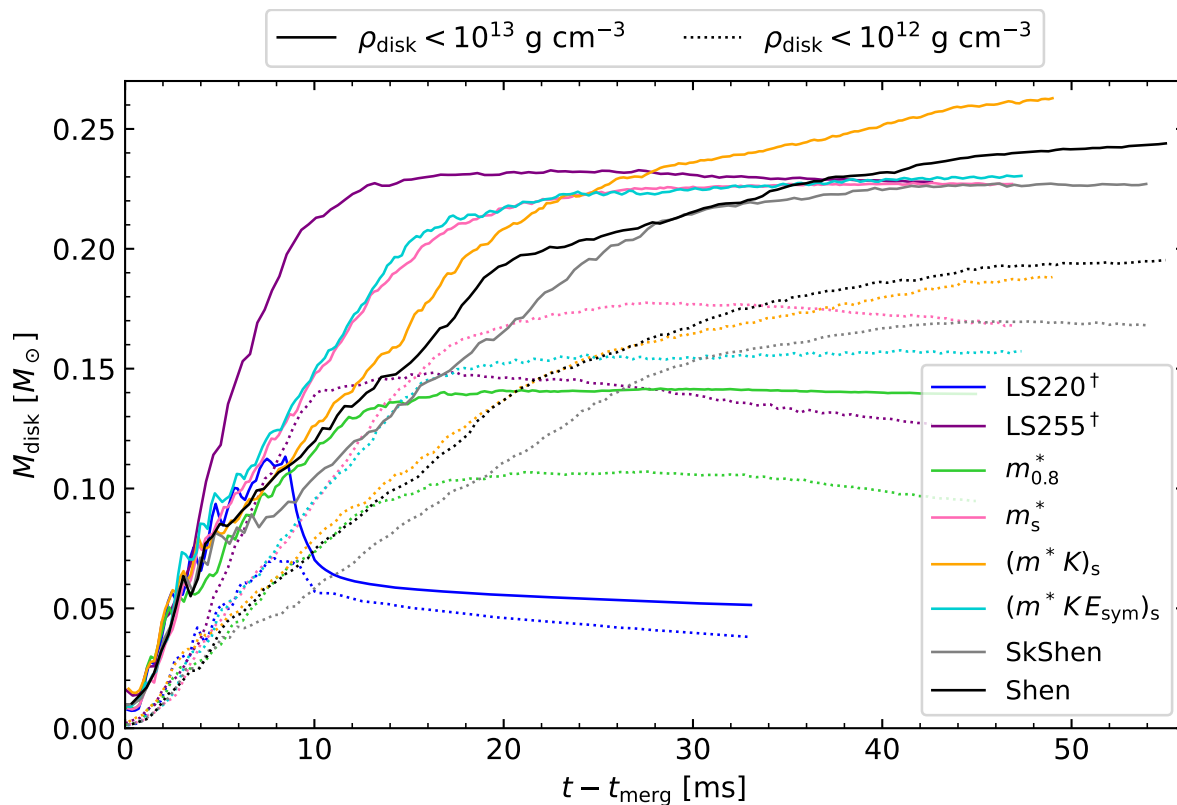


Figure 4.10.: Evolution of the disk mass for all simulations except LS175[†]. Solid and dotted lines correspond to different definitions of the disk contour.

central collapses to BH almost immediately after the merger, so no disk is formed. The BH formation in LS220[†] is delayed long enough for a disk to form. However, roughly half of the disk mass is swallowed at the collapse. For non-collapsing mergers, the relation of the disk mass to the EOS is more complicated. On one hand, the disk mass originating from the tidal disruption of the NSs is larger for stiffer EOS. For a softer EOS, on the other hand, matter ejection due to shock heating is enhanced. Furthermore, the remnant is more compact and rotates faster (see, e.g., Bernuzzi, 2020; Nedora et al., 2021b) which also increases the disk mass. In addition to the EOS at zero temperature, thermal effects have to be considered. A larger thermal index enhances the amount of matter ejected to the disk because of shock heating (see Section 4.2.1). It is thus hard to find a correlation between the disk mass and specific nuclear matter properties.

At the end of the simulations that do not form a BH the disk mass is close to $0.25M_{\odot}$. The only exception is $m_{0.8}^*$ with a disk mass of $\sim 0.14M_{\odot}$. The disk in LS255[†] is particularly massive in comparison to the other models, especially in the first ~ 20 ms after the merger. This is surprising because as described in the previous chapter, the evolution of the massive NS in LS255[†] is most comparable to $m_{0.8}^*$. Therefore, one would expect, that the two simulations also exhibit similar disk masses. This apparent contradiction is partially resolved if the inner boundary of the disk is defined by $\rho < 10^{12} \text{ g cm}^{-3}$ (dotted lines in Fig. 4.10). In this case, the disk mass at the end of LS255[†] is much closer to the one in $m_{0.8}^*$. However, the peculiarly fast

initial growth of the disk persists.

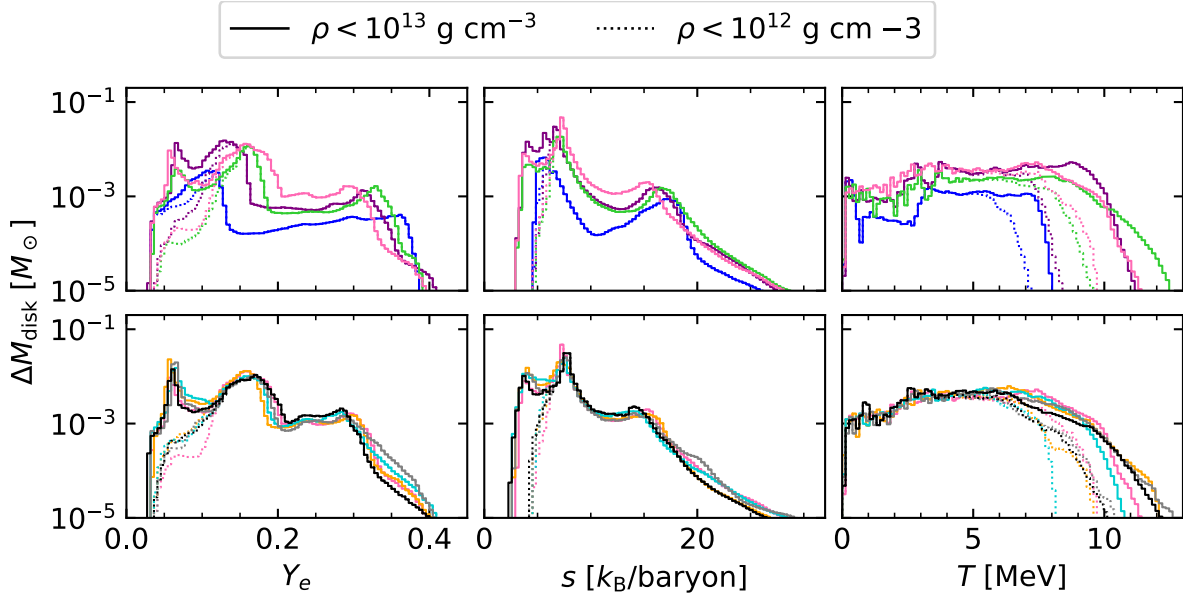


Figure 4.11.: Mass-weighted histogram of the electron fraction, entropy, and temperature in the disk at $t = 30$ ms. Dotted lines show the histograms when matter with $\rho > 10^{12} \text{ g cm}^{-3}$ is excluded. The histograms are split into two panels for better readability. The colors denote the different models and have the same meaning as in Figs. 4.7 to 4.10.

Even though the evolution of the masses of the accretion disk varies for the different EOS, the composition and structure of the disk are relatively similar in all non-collapsing simulations. The mass-weighted histogram of the electron fraction and entropy in the disk at $t = 30$ ms is shown in Fig. 4.11. All histograms show a triple peak structure, typical for equal mass BNS mergers (Nedora et al., 2021b). The peak at the lowest entropy and electron fraction corresponds to the interface between the remnant and the disk. The dotted lines in Fig. 4.10 show the histograms for the matter at densities below $10^{12} \text{ g cm}^{-3}$ which lack this high temperature, low entropy, and low electron fraction tail. The second peak at $s \approx 4 - 8 k_B/\text{baryon}$ and $Y_e \approx 0.1 - 0.2$ represents the bulk of the disk. The disk bulk has densities between $10^{10} - 10^{12} \text{ g cm}^{-3}$ and extends to roughly 100 km. For most simulations, the main peaks in the electron fraction and entropy are located at $Y_e = 0.16$ and $s = 7.5 k_B/\text{nucleon}$. The largest deviations from this trend are LS220[†] and LS255[†]. Since the central object in LS220[†] is a BH, the hot and dense interface to the NS is missing, so there are no spiral arms in the disk. Furthermore, the strong neutrino irradiation from the central NS is also missing. Therefore, the disk has lower temperatures, entropies, and electron fractions. Due to the higher incompressibility of LS255[†], a larger fraction of the disk is located closer to the massive NS. This effectively shifts the average bulk entropy and energy toward lower values. The same is true for $(m^* K)_S$ and $(m^* K E_{\text{sym}})_S$, however, to a lesser extent.

The third peak with high electron fractions and entropies is due to the matter outside of the main bulk of the disk. During the disk evolution, this matter becomes partially unbound.

Thus its composition matches that of the disk wind ejecta in Fig. 4.13 (see Section 4.3 for an extended discussion).

4.3. Ejecta properties

The mass ejection in BNS mergers occurs through multiple channels. These can be separated into two categories: dynamic and disk (or secular) ejecta. The former are expelled within a few milliseconds after the merger, while the latter are ejected over timescales of 10 ms up to 10 s (see, e.g., Fujibayashi et al., 2023). In order to distinguish the different ejecta components, we show the ejecta composition of the m_{S}^* model in Fig. 4.12. The ejecta properties are extracted

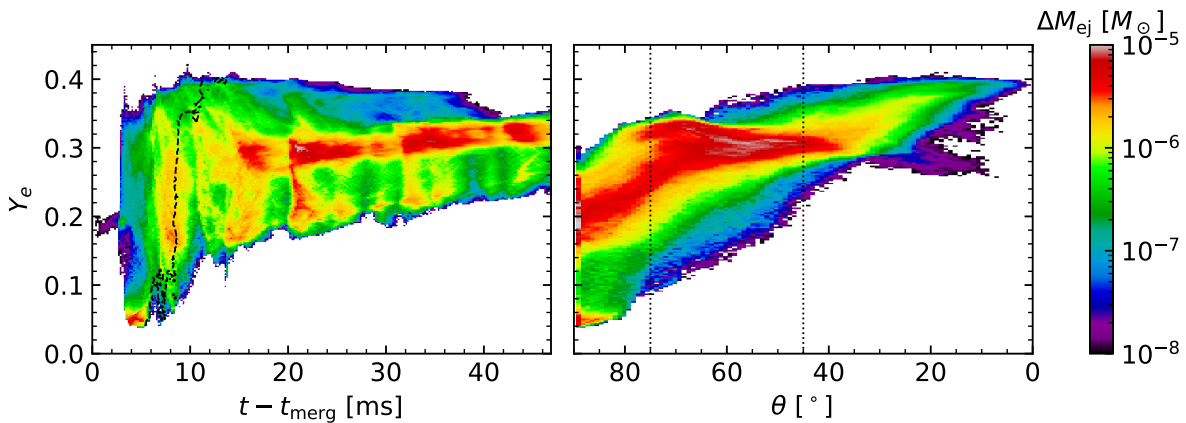


Figure 4.12.: Cumulative mass-weighted histogram of ejecta properties in model m_{S}^* until the end of the simulation. Left panel: Two-dimensional histogram of the electron versus the time after the merger. The time corresponds to the time at which the ejecta cross the detection sphere at 300 km. The dashed contour marks the transition point from dynamical ejecta to shock-heated ejecta. Right panel: Two-dimensional histogram of the electron fraction versus the polar angle. The dashed vertical lines show the angles marked in Fig. 4.14.

on a sphere at 300 km as outlined in Section 4.1.3. The left and right panels show the 2D histograms of the ejecta electron fraction versus time and angle of ejection, respectively. We use m_{S}^* as an example here but note that most other simulations show similar trends to the ones discussed below. As described in Section 4.1.3, we define the dynamical ejecta as matter that fulfills the geodesic criterion, while matter that fulfills the Bernoulli criterion but not the geodesic criterion is associated with the disk ejecta. This division is shown by the dashed contour in Fig. 4.12. The same division is used in Nedora et al. (2021b); Combi & Siegel (2023). Note, however, that the distinction is only approximate as the transition from dynamical ejecta to disk ejecta happens continuously between 5-10 ms after the merger. As outlined in Section 2.3, the dynamical ejecta are comprised of two components: Matter unbound by tidal torques and matter ejected by shock heating at the interface of the merger. We thus further divide the dynamical ejecta into the tidal and shock-heated components. Dynamical ejecta are counted toward the tidal component if their electron fraction is smaller than 0.1 and towards the shock-heated component otherwise.

Figure 4.13 shows the accumulated mass histogram of the ejecta electron fractions, entropies, and asymptotic velocities. The simulations are split into two groups (upper and lower panels) for better readability. Dashed lines show the dynamical ejecta and solid lines the disk ejecta.

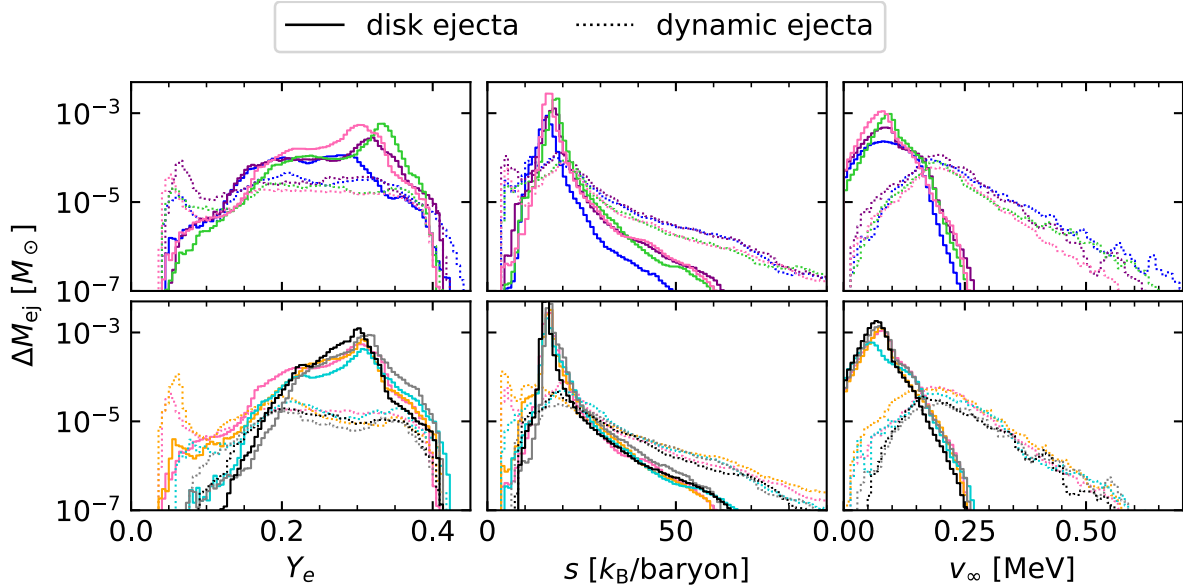


Figure 4.13.: Mass-weighted histogram of the electron fraction, entropy, and asymptotic velocity of the ejected matter. Solid and dotted lines represent dynamical ejecta and disk ejecta, respectively. The colors denote the different models and have the same meaning as in Figs. 4.7 to 4.11.

Tidal torques remove matter from the outer layers of the NSs and expel it in the equatorial direction. If the tidal ejecta do not experience significant shock heating, they consist of almost pure cold NS matter ($Y_e < 0.1$) and have low entropies ($s < 10$). This part is visible in the lower left corners of both panels in Fig. 4.12 and forms a peak at low electron fractions and entropies in Fig. 4.13. A fraction of the tidally removed matter can be reprocessed by shocks and thus counts towards the shock-heated ejecta component. In $(m^* K E_{\text{sym}})_S$, SkShen, and Shen, this effect removes almost all of the tidal ejecta.

The shock-heated ejecta component reaches much higher temperatures and entropies compared to the tidal ejecta. Therefore, positron and electron-neutrino captures increase the electron fraction of the matter to $Y_e \approx 0.2 - 0.4$. It is visible in the left panel of Fig. 4.12 as large bulk of matter at roughly 6 - 10 ms after merger. A small part of the shock-heated ejecta is responsible for the high velocity tail in the right panels of Fig. 4.13. As discussed in Section 2.3, these ejecta can lead to additional observable features in the kilonova (KN) and is larger for softer EOS.

After the NSs merge, an accretion disk forms from debris around the newly created remnant. This system can eject matter through multiple mechanisms depending on the lifetime of the remnant. On timescales above 100 ms, a sizable fraction of the disk can become unbound by magnetically induced viscosity (Fernández & Metzger, 2013; Metzger & Fernández, 2014; Just et al., 2015, 2021; Fujibayashi et al., 2018, 2020c,b,a, 2023; Hayashi et al., 2022; Fahlman & Fernández, 2022) and recombination of nucleons into alpha particles and heavier nuclei

(Fernández & Metzger, 2013; Siegel & Metzger, 2017, 2018). However, our simulations do not include effective viscosity or magnetohydrodynamics and only last for 40-50 ms post-merger.

On the simulated timescales, the mass ejection in the early post-merger phase is primarily driven by the oscillating double-core structure in the massive NS. With each bounce, matter becomes unbound as the central density reaches a minimum (Nedora et al., 2019, 2021b; Combi & Siegel, 2023). The left panel of Fig. 4.12 shows several such bursts of matter ejection after $t \approx 10$ ms. Furthermore, winds driven by neutrino absorption (Dessart et al., 2009; Perego et al., 2014; Just et al., 2015; Radice et al., 2018) expel matter from the early post-merger remnant. Above the disk, the matter is irradiated by a strong flux of neutrinos stemming from the hot remnant-disk interface (see, e.g., Perego et al., 2014). This increases the electron

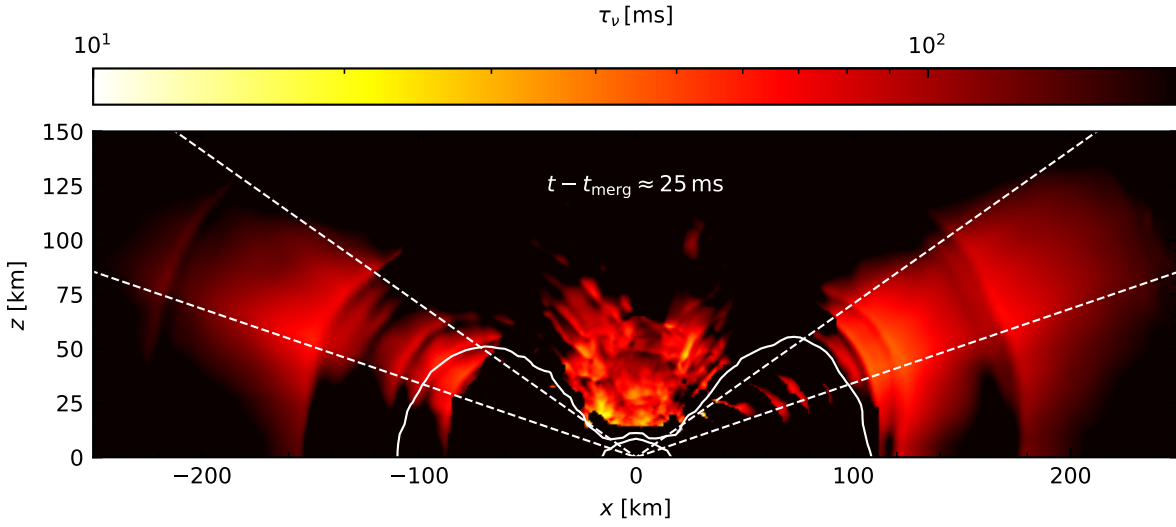


Figure 4.14.: Net neutrino heating timescale, Eq. (4.7), for the model m_S^* in the xz plane at $t - t_{\text{merg}} \approx 25$ ms. The dashed white lines mark the polar angles between $\theta = 45^\circ - 75^\circ$, corresponding to the dotted lines in the right panel of Fig. 4.12. The outer and inner accretion disk boundaries are approximately marked by the 10^{10} and $10^{13} \text{ g cm}^{-3}$ density contours which are plotted in white.

fraction and internal energy of the ejecta. In LS220[†], after the HMNS collapses the neutrino radiation is strongly reduced and the matter ejection due to the NS’s oscillation stop, so the ejection of matter stops after $t > 20$ ms.

Neutrino heating plays a major role in the early post-merger phase. The timescale of the neutrino heating τ_ν is given by the ratio of the conserved internal energy density $\tau = E - D$ and the local net neutrino heating rate $Q_\nu = Q_\nu^{\text{M0}} - Q_\nu^{\text{Leak}}$:

$$\tau_\nu = \frac{1}{\alpha W} \frac{E - D}{Q_\nu^{\text{M0}} - Q_\nu^{\text{Leak}}}, \quad (4.7)$$

where α and W are approximate corrections for the gravitational redshift of the neutrinos. In Fig. 4.14, we show the net neutrino heating timescale in the xz plane of the model m_S^* at $t - t_{\text{merg}} \approx 25$ ms. Directly above the massive NS the neutrino heating is very strong. However, the density in the polar direction is low, so the neutrino heating unbinds only a small amount

of matter in this region. This matter is ejected toward the polar direction with relatively high velocities and electron fractions. Initially, the oscillations of the massive NS ejects matter also in the equatorial direction. The dense bulk of the disk shields the matter in the equatorial plane outside the disk from neutrino irradiation. Therefore, the equatorial ejecta have lower electron fractions ($Y_e \approx 0.2 - 0.25$). Furthermore, the energy deposition by neutrinos is reduced, so the amount of mass ejected in this direction decreases continuously as the oscillations of the massive NS die down. In the diagonal direction ($\theta \approx 45 - 75^\circ$), heating due to neutrino absorption is stronger. This region is marked by dotted lines in Fig. 4.12 and Fig. 4.14. The neutrino heating in this area enhances the mass outflow significantly and increases its electron fraction. This part of the ejecta is responsible for the peaks at $Y_e \approx 0.3$ in Fig. 4.13. With time the disk becomes thinner and more transparent to neutrinos. As a result, the neutrino-enhanced outflow becomes more proton-rich and moves closer to the equatorial plane.

In Table 4.3 the masses of all discussed ejecta components at $t - t_{\text{merg}} = 40$ ms are given for all simulations. The tidal, shock-heated, and disk ejecta masses are visualized in Fig. 4.15. The mass of the tidal ejecta varies between $10^{-6} - 4.3 \times 10^{-3} M_\odot$. In the models $(m^* K E_{\text{sym}})_S$, SkShen, and Shen, the tidal ejecta are “overtaken” by the shock-heated component early on, so almost no material with $Y_e < 0.1$ remains. The tidal ejecta mass is significantly larger for LS255[†] and $(m^* K)_S$ compared to the other models. This suggests that increasing the incompressibility enhances the effectiveness of the tidal ejection mechanism as described in Section 4.2. Figure 4.16 shows the tidal arms in the xy plane shortly after merger for LS175[†], LS220[†], and LS255[†]. The size of the tidal arms grows with the incompressibility. Comparing $M_{\text{tidal}}^{\text{ej}}$ for models LS220[†], $m_{0.8}^*$, and m_S^* indicates that reducing the effective mass also increases the tidal ejecta component, though the influence is not as strong as that of the incompressibility. This can be seen in Fig. 4.17, which shows the distribution of the electron for the models LS220[†], $m_{0.8}^*$, and $m_S^* \sim 16$ ms after the merger. The tidal ejecta (red regions) are slightly more massive for lower effective masses. Even though the mass of the tidal dynamical ejecta component is relatively small in comparison to the other components it plays a significant role because it can produce actinides. This is not only important for the galactic chemical evolution

Model	$M_{\text{tot}}^{\text{ej}}$ [$10^{-3} M_\odot$]	$M_{\text{dyn}}^{\text{ej}}$ [$10^{-3} M_\odot$]	$M_{\text{tidal}}^{\text{ej}}$ [$10^{-3} M_\odot$]	$M_{\text{shock}}^{\text{ej}}$ [$10^{-3} M_\odot$]	$M_{\text{disk}}^{\text{ej}}$ [$10^{-3} M_\odot$]	$M_{v_\infty > 0.6c}^{\text{ej}}$ [$10^{-6} M_\odot$]
LS255 [†]	7.096	1.995	0.403	1.592	5.101	0.665
LS220 [†]	5.307	1.706	0.104	1.603	3.601	4.597
$m_{0.8}^*$	7.717	1.249	0.138	1.111	6.469	2.050
m_S^*	9.372	1.097	0.184	0.913	8.275	0.362
$(m^* K)_S$	8.645	1.360	0.430	0.930	7.285	0.385
$(m^* K E_{\text{sym}})_S$	5.887	0.905	0.021	0.883	4.982	0.467
SkShen	7.939	0.554	0.004	0.550	7.384	0.079
Shen	9.527	0.645	0.001	0.645	8.882	0.066

Table 4.3.: Masses of the different ejecta components at $t - t_{\text{merg}} = 40$ ms. Dynamic ($M_{\text{dyn}}^{\text{ej}}$) and disk ejecta ($M_{\text{disk}}^{\text{ej}}$) are defined by the geodesic criterion (Section 4.1.3). Tidal ($M_{\text{tidal}}^{\text{ej}}$) and shock heated dynamical ejecta are ($M_{\text{shock}}^{\text{ej}}$) distinguished by $Y_e < 0.1$ and $Y_e > 0.1$, respectively.

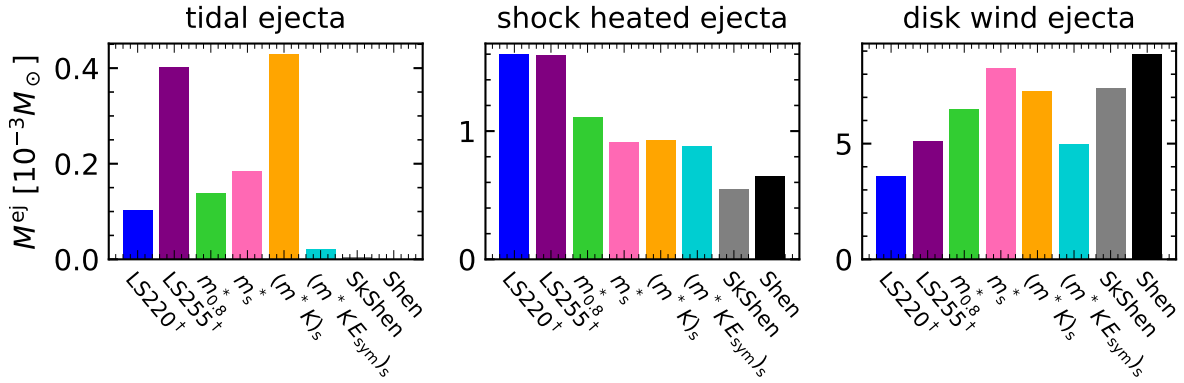


Figure 4.15.: Masses of the tidal, shock-heated, and disk ejecta components.

but also the KN light curve, which might show signatures of fission reactions if very heavy elements are produced.

The mass of the shock-heated dynamical ejecta shows a strong correlation with the effective mass. LS255[†] and LS220[†] exhibit the largest amount of shock-heated ejecta, followed by $m_{0.8}^*$ and then m_s^* , $(m^* K)_s$, and $(m^* K E_{\text{sym}})_s$. This is visible in Fig. 4.17. The amount of shock-heated ejecta (green regions) is larger for lower effective masses. Note, however, that only a fraction of the shock-heated material is ejected in the equatorial plane and thus visible in the plot. SkShen and Shen exhibit an even smaller amount of shock-heated ejecta. This might be due to the different saturation densities and/or binding energies. Note that this study

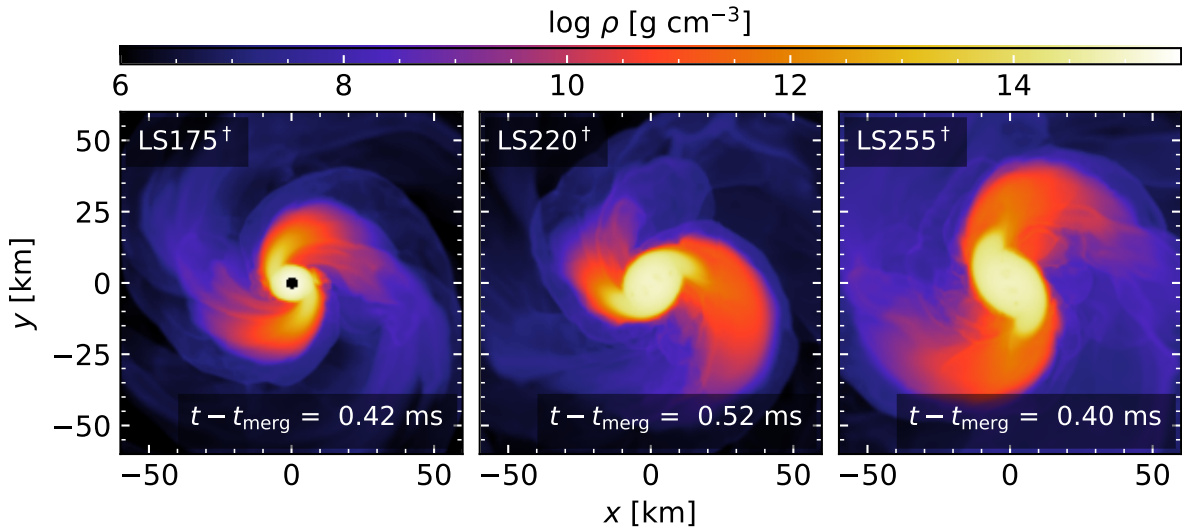


Figure 4.16.: Density distribution in the xy plane for the models LS175[†], LS220[†], and LS255[†] shortly after the merger. The size of the tidal arms is largest for LS255[†] and smallest for LS175[†]. In LS175[†], the central object already has collapsed so the tidal ejecta will be almost completely swallowed by the BH.

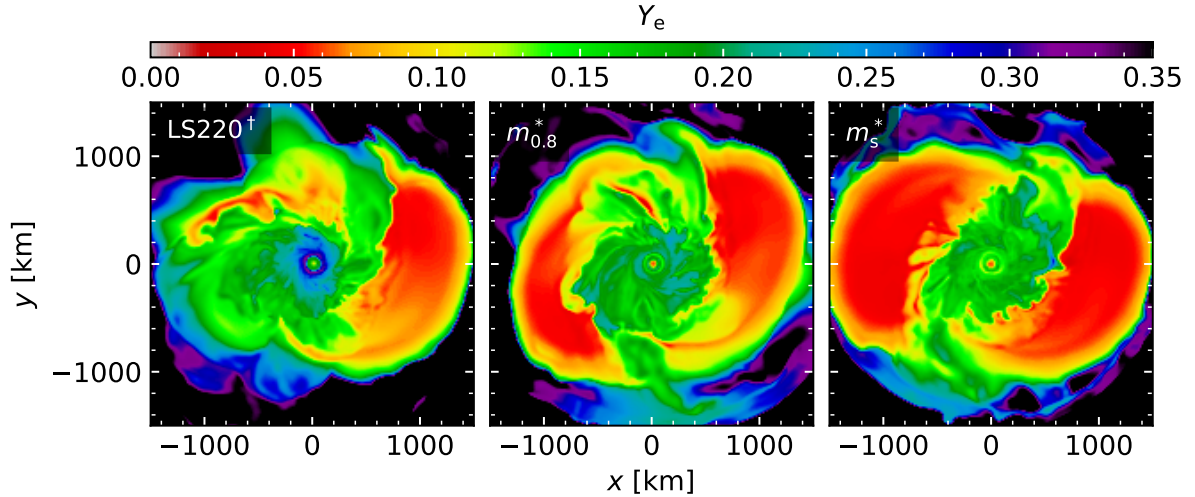


Figure 4.17.: Distribution of the electron for the models LS220[†], $m_{0.8}^*$, and $m_s^* \sim 16$ ms after the merger. Red regions show the low Y_e tidal ejecta while green regions are the ejecta driven by shock-heating. Note that only a fraction of the shock-heated material is ejected in the equatorial plane. Thus, most of the shock-heated ejecta are not visible in this plot.

represents only a small sample of models and does not include asymmetric binary mergers. A larger sample of models is thus necessary to confirm these findings.

The evolution of the mass ejection rate for the disk component is shown in Fig. 4.18. We find, that the mass ejection in the disk phase is more effective while the $m = 2$ bar-shaped deformation of the remnant drives two spiral arms into the disk (see Fig. 4.8). The model LS255[†] exhibits a period of low mass ejection after $\sim 15 - 20$ ms that lasts approximately 20 ms. A similar feature is visible for $(m^* KE_{\text{sym}})_S$ after ~ 25 ms, lasting approximately 10 ms. Both correlate well with periods of low $m = 2$ deformations of the remnant with a delay of ~ 10 ms which is roughly the time it takes ejecta to travel to the detection radius at 300 km. Later, a one-armed spiral wave, driven by the $m = 1$ deformation, appears, resulting in an increased mass ejection rate. Similar results were found by Nedora et al. (2019, 2021b). Note, however, that the mass ejection is still ongoing at the end of all simulations except LS175[†] and LS220[†], and is expected to be further enhanced by viscous effects on timescales of seconds. Thus, the secular mass ejection is not fully captured in our simulations.

We implemented a tracer particle scheme to follow the ejected matter in a Lagrangian frame. We describe the tracer-particle method in general and a novel tracer-distribution scheme we implemented in Appendix A. The trajectory and the history of the hydrodynamical quantities recorded along the path are used to calculate the detailed nucleosynthesis outcome with a nuclear reaction network. These calculations will be performed in the near future.

4.4. Gravitational wave emission

Figure 4.19 shows the $+$ mode of the GW strain for all simulations except LS175[†], since no significant post-merger signal is produced after the prompt collapse. We only show the

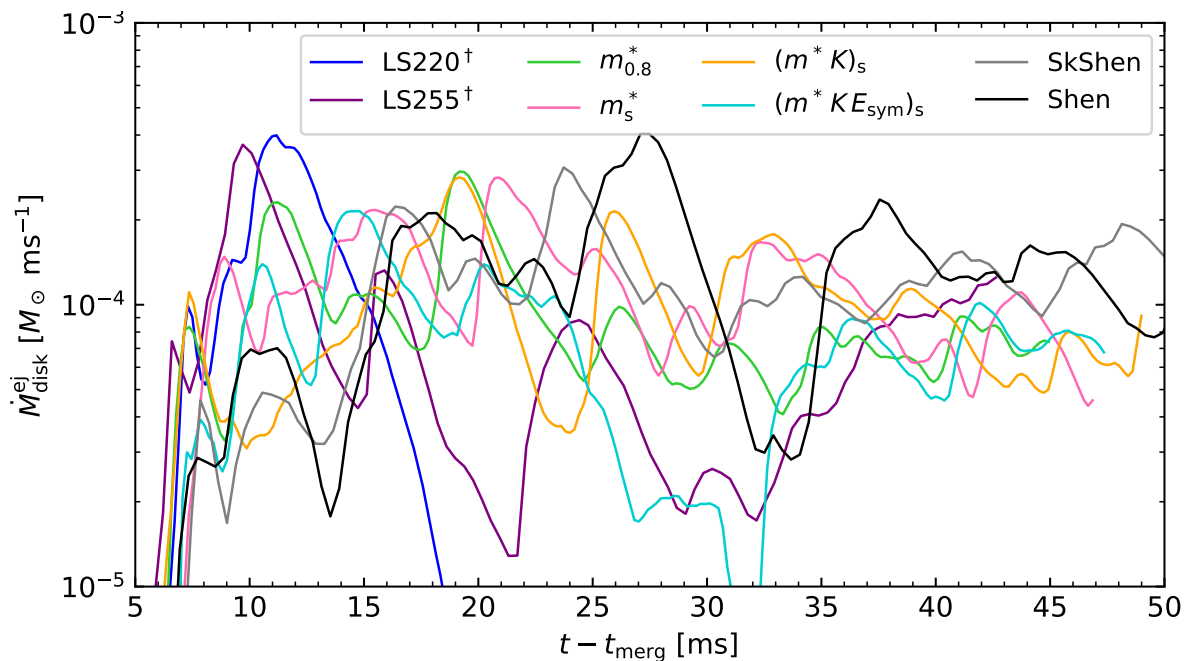


Figure 4.18.: Mass ejection rate for the disk ejecta component as a function of time.

$l = m = 2$ mode, since it is by far the most dominant mode. It shows the low-frequency pre-merger phase ($t < 0$), as well as the post-merger phase ($t > 0$). The latter consists of two periods. A transition period ($t \lesssim 3$ ms), during which the system readjusts from the inspiral of two NSs to one rotating and oscillating massive NS, and the longer ring-down phase that follows, during which the amplitude gradually decreases (see, e.g., [Baiotti, 2019](#)). The GW signal stops abruptly after the collapse of the HMNS in LS220[†]. In LS255[†] and $(m^* K E_{\text{sym}})_s$ and $(m^* K)_s$, the GW amplitude drops within the first 10-15 ms while it decreases more slowly within 20-30 ms in $m_{0.8}^*$, m_s^* SkShen, and Shen. This decrease in the amplitude is directly linked to the $m = 2$ deformation of the massive NS (see Fig. 4.8). As described in Section 4.2.3, the $m = 2$ deformation decreases much faster in the simulations with higher incompressibility. Future detections of post-merger GWs could therefore be used to constrain the slope of the pressure at high densities.

The post-merger GW time-frequency spectrograms (upper panels) and the corresponding Fourier spectra (lower panels) of the simulations are shown in Fig. 4.20. The thin lines in the Fourier spectra represent the full spectrum, while the thick lines are produced by excluding the pre-merger GW signal. Initially, several frequencies are present but they decay within approximately 5 milliseconds ([Takami et al., 2015](#); [Rezzolla & Takami, 2016](#)). Afterward, the spectrum is dominated by a single frequency, often called f_2 . This frequency has been identified and studied in many previous works ([Stergioulas et al., 2011](#); [Bauswein et al., 2012](#); [Bauswein & Janka, 2012](#); [Hotokezaka et al., 2013a](#); [Takami et al., 2014, 2015](#); [Rezzolla & Takami, 2016](#)) and is attributed to the quadrupole mode of the NS ([Bauswein et al., 2012](#); [Bauswein & Janka, 2012](#)). The solid vertical lines show the maximum of the Fourier spectra, while the dotted lines follow the time-dependent maximum frequency.

The following effects can be seen in the time-frequency spectrograms:

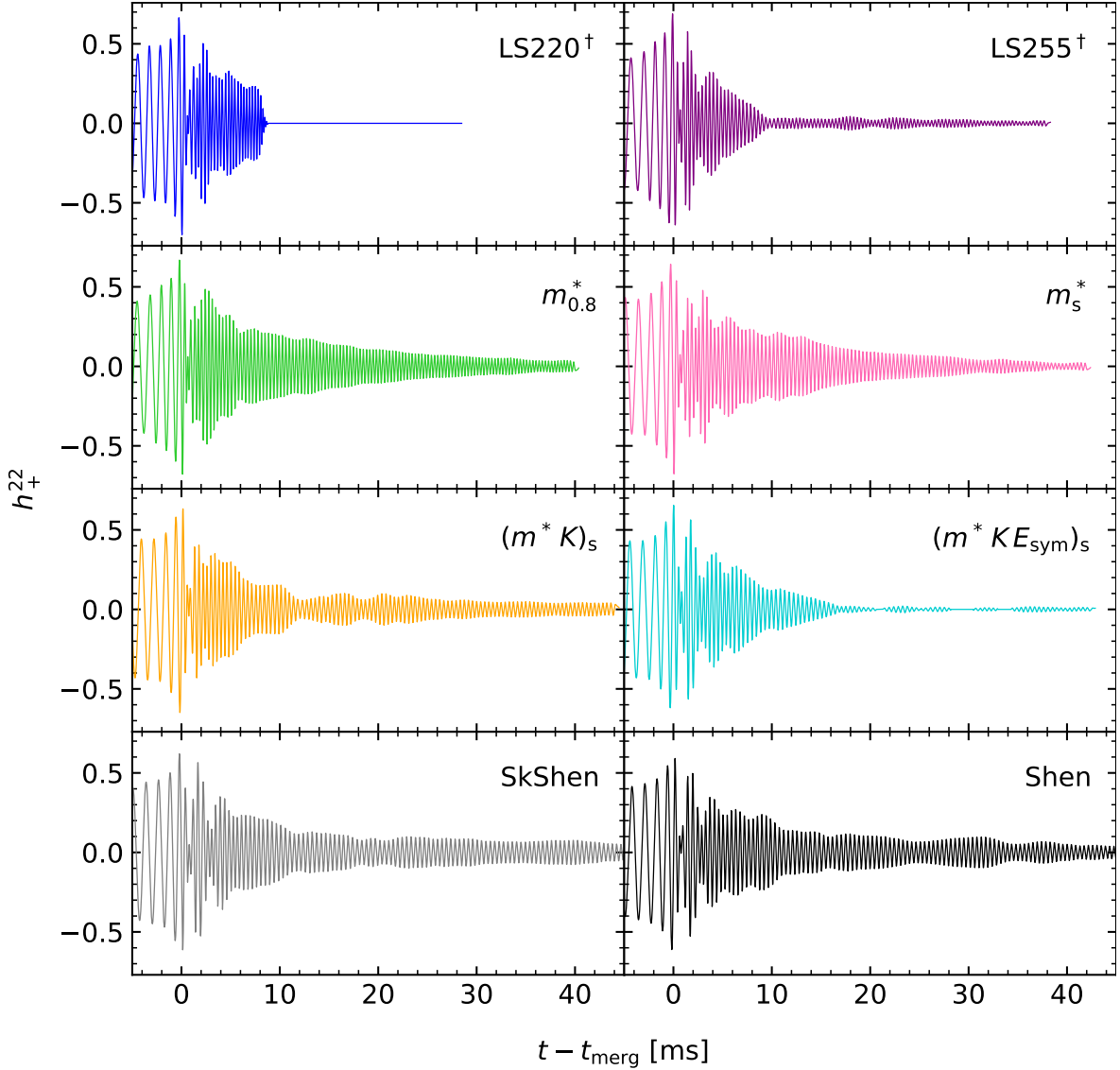


Figure 4.19.: Waveforms of the GW signals for all simulations except LS175[†].

- In LS220[†], the post-merger signal shows a “chirp-like” behavior (the peak frequency rises quickly) shortly before the remnant collapses to a BH. This is because the rotational velocity of the HMNS increases significantly as it collapses.
- In the first 10 ms of the post-merger GW emission, the f_2 frequency can vary slightly. This is especially visible for the stiffest EOS, $(m^*K)_S$, $(m^*KE_{\text{sym}})_S$, SkShen, and Shen. For these, the f_2 frequency increases until $t \approx 5$ ms and subsequently decreases again until $t \approx 10$ ms. A similar effect is described by [Rezzolla & Takami \(2016\)](#). They determine the frequency during the transient phase separately from the ring-down phase and label it $f_{2,i}$.

- After the initial transient phase, a continuous shift of the f_2 emission towards higher frequencies is visible for $m_{0.8}^*$ and m_s^* . A similar but weaker increase is visible for m_s^* , SkShen, and Shen. In these models, gravitational wave amplitude stays high for an extended period. The GWs carry away angular momentum, the NS contracts and this leads to a higher f_2 (Maione et al., 2017).

Similar trends can be seen in the spectrograms in Rezzolla & Takami (2016); Dietrich et al. (2017); Maione et al. (2017).

The second most prominent peak is the so-called f_1 peak (sometimes also called f_-), which always lies at lower frequencies than the f_2 peak and disappears after ~ 5 ms (Stergioulas et al., 2011; Takami et al., 2014, 2015; Rezzolla & Takami, 2016). Its origin has been attributed to the interaction of the f_2 and the quasi-radial f_0 mode (named f_{2-0}) (Stergioulas et al., 2011) as well as the orbital motion of antipodal bulges rotating around the central remnant with a slower frequency (thus called f_{spiral}) (Bauswein & Stergioulas, 2015). Depending on the remnant compactness, either one or both frequencies might be present (Bauswein & Stergioulas, 2015; Bauswein et al., 2016; Rezzolla & Takami, 2016; Maione et al., 2017; Kiuchi et al., 2020).

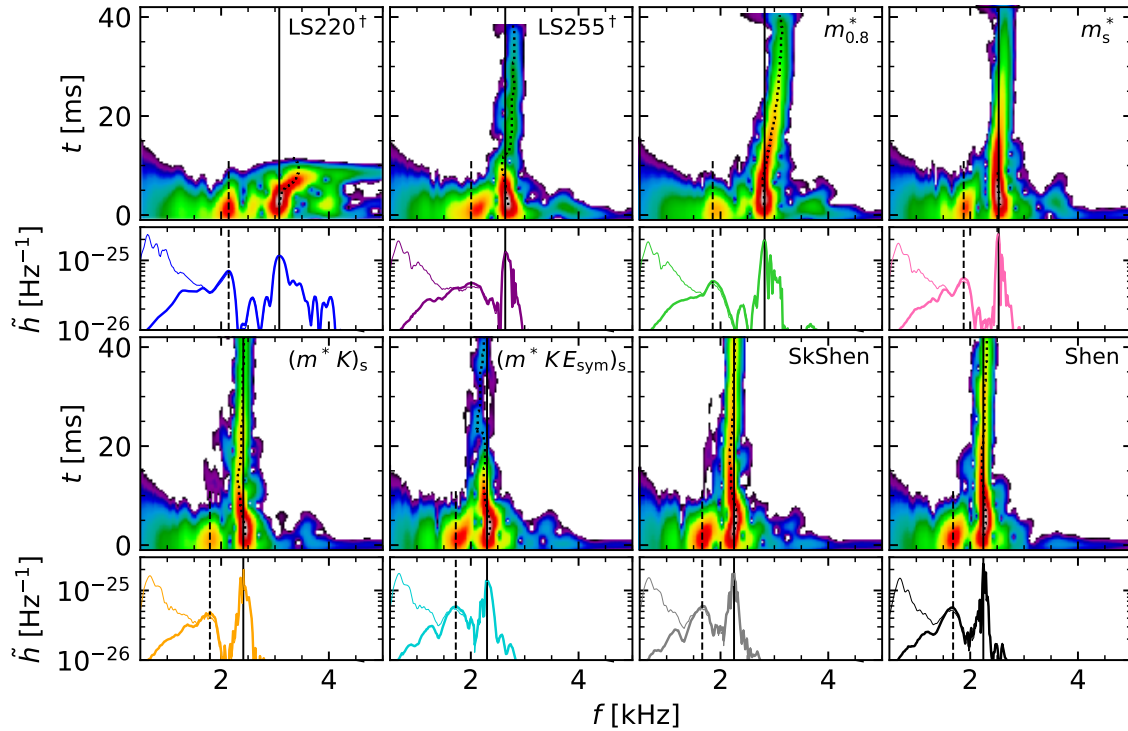


Figure 4.20.: Post-merger GW Fourier spectra and corresponding time-frequency spectrograms. The thin lines in the Fourier spectra show the full spectrum, while the thick lines are produced by excluding the pre-merger GW signal. Dashed and solid vertical lines mark the position of the f_1 and f_2 peak frequencies extracted from the time-independent Fourier spectra, and dotted lines show the time-dependent peak frequency extracted from the time-frequency map.

We define f_1 independently of its origin as the second highest peak with a frequency at least 400 Hz below the f_2 peak. The extracted f_1 peaks are marked by a dashed vertical line in Fig. 4.20.

The f_1 and f_2 frequencies for all simulations are listed in Table 4.2. They span from $f_2 = 2.24$ kHz for Shen to $f_2 = 3.10$ kHz for LS220[†] and $f_1 = 1.66$ kHz for SkShen to $f_1 = 2.14$ kHz for LS220[†] where softer EOS generally produce larger frequencies. Decreasing the effective mass and increasing the incompressibility and symmetry energy lowers the pressure in the center of the NS. This decreases the density, which in turn reduces f_2 (Bauswein et al., 2012; Bauswein & Janka, 2012). By changing the nuclear matter properties to the values of the Shen EOS (i.e., the progression m_S^* , $(m^*K)_S$, $(m^*KE_{\text{sym}})_S$, SkShen), both peak frequencies approach those of the Shen simulation. Both the Fourier spectra and the time-frequency spectrograms of models Shen and SkShen are very similar. Especially the position and width of the f_1 and f_2 peaks as well as the amplitude and time dependence of the spectrogram match almost perfectly. This implies, that the EOS-impact on the post-merger GW emission is well described by the nuclear matter properties of the EOS, while the details of the microphysics and methods (i.e., relativistic mean field and Skyrme density functionals) only play a minor role. It will thus be possible to directly constrain the properties of nuclear matter with future measurements of the post-merger GW spectra based on numerical simulations of BNS mergers.

Many works have found that the f_2 frequency is highly correlated with the properties of the high-density EOS. Takami et al. (2015); Rezzolla & Takami (2016); Bauswein et al. (2016); Kiuchi et al. (2020) have provided fit formulae relating f_1 and f_2 with various TOV properties. In Fig. 4.21, we compare their fit formulae with our results. The plot in the lower right corner shows the residuals of the fit function. All fit formulae predict the correct frequencies within an uncertainty of 5-10%. However, some trends in the difference can be identified. Fit formulae for f_2 (solid symbols connected with solid lines in the lower right panel) underestimate the value for f_2 in LS220[†] and overestimate it in LS255[†] and m_S^* , $(m^*K)_S$, $(m^*KE_{\text{sym}})_S$, SkShen, and Shen. The fit from Kiuchi et al. (2020) performs better, but also uses the most fit parameters. The fits for f_1 perform relatively well for the models with $m^*/m < 1$ but overestimate the frequency for LS255[†] and LS220[†]. Our collection of simulations is too small to make quantitative predictions for the peak frequencies. However, we plan to increase the number of models. Therefore, we will potentially be able to enhance the accuracy of universal relations in the future by incorporating additional parameters describing the equation of state (EOS) into the fits.

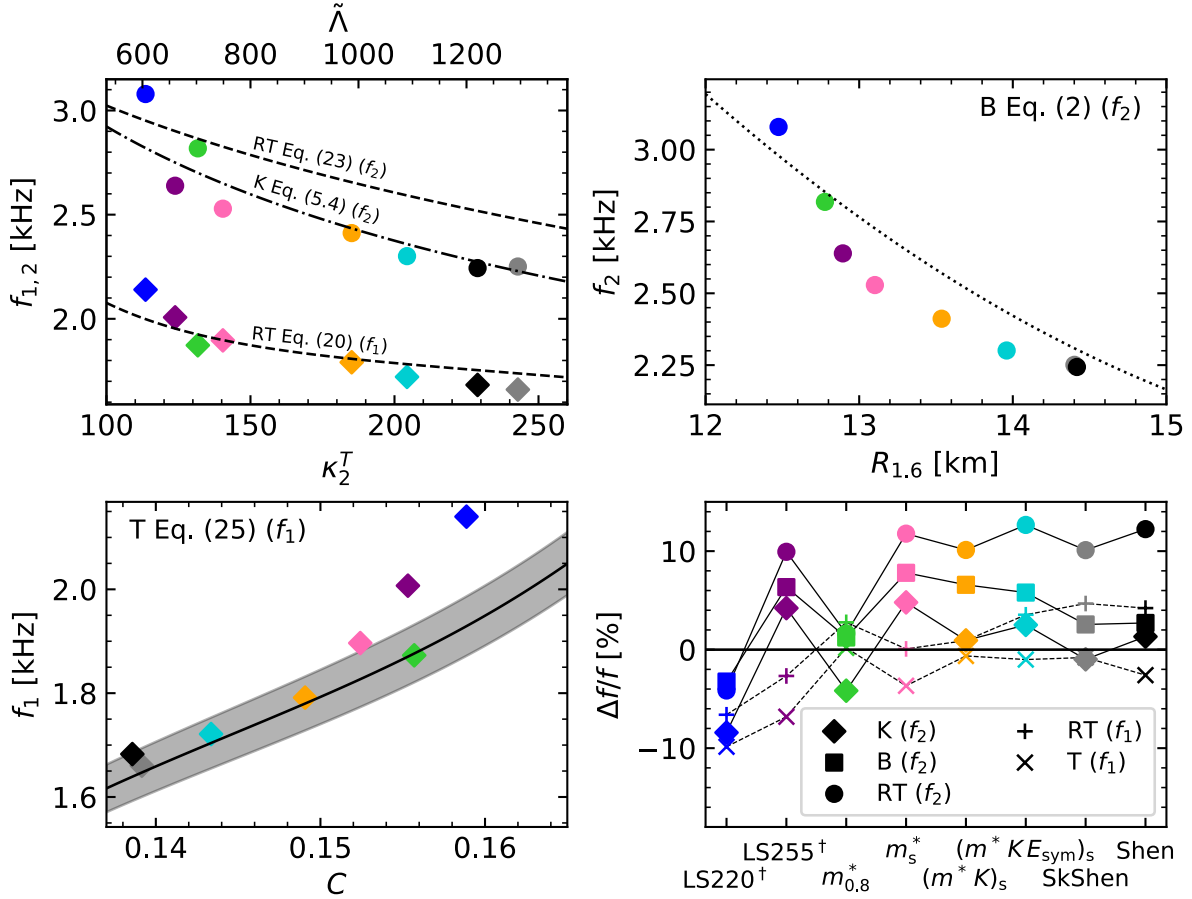


Figure 4.21.: Comparison of the post-merger GW spectrum with various fit formulae from the literature. Top left: Fit formulae for f_2 versus κ_2^T (or $\tilde{\Lambda} = 16/3\kappa_2^T$, see Section 2.2.1) from Rezzolla & Takami (2016), Eq. (23) (labeled RT) and Kiuchi et al. (2020), Eq. (5.4) (labeled K). Rezzolla & Takami (2016) also provide a fit, Eq. (20), for f_1 which is shown as diamonds. Top right: Fit formula for f_2 versus $R_{1,6}$ from Bauswein et al. (2016), Eq. (2) (labeled B). Bottom left: Fit formula for f_1 versus the compactness parameter C from Takami et al. (2015), Eq. (25) (labeled T). They also provide an uncertainty band shown in gray. Bottom right: Relative deviations of the fits. Solid symbols connected with solid lines represent fits for f_2 , while straight and diagonal crosses connected with dashed lines represent fits for f_1 . The colors denote the different models and have the same meaning as in Figs. 4.7 to 4.11.

5. Long-term modeling of the post-merger system

In the age of multi-messenger astronomy, BNS merger events such as GW170817 are among the most promising candidates for the source of r -process elements in the galaxy. Understanding the mass-ejection mechanisms of such events is crucial to interpret their electromagnetic emissions. These mechanisms can take place on time scales of a few milliseconds to a few seconds (see Section 2.3). Therefore, it is necessary to evolve simulations of BNS mergers for multiple seconds. Simulations in 3D with realistic neutrino transport and good resolution are mostly limited to a few hundred milliseconds. Only recently a few 3D simulations of BH-NS mergers and BNS mergers evolving the system for more than one second were performed [Hayashi et al. \(2022\)](#); [Kiuchi et al. \(2022\)](#). However, long-time simulations in three dimensions with sufficient resolution require immense computational resources. This makes it impossible to perform large sets of 3D simulations for parameter studies, e.g., to investigate the effect of the EOS.

After a few tens of milliseconds, the merger remnant and the surrounding accretion disk have settled into an approximately axisymmetric configuration. In this work, we exploit this configuration to evolve the post-merger system under the assumption of axisymmetry. Axisymmetric simulations of BH- and NS-accretion disk systems have been performed in several works ([Dessart et al., 2009](#); [Fernández & Metzger, 2013](#); [Metzger & Fernández, 2014](#); [Just et al., 2015, 2016](#); [Lippuner et al., 2017](#); [Fujibayashi et al., 2017, 2018, 2020a,b, 2023](#); [Fernández et al., 2020](#); [Shibata et al., 2021](#)). However, to obtain the full mass ejection history of a BNS merger, the dynamic and the accretion disk phases need to be simulated consistently. To achieve this, we create the initial data for the 2D simulations based on previously performed 3D simulations. After simulating the 3D system for a sufficient amount of time (~ 50 ms), the hydrodynamic state of the remnant is averaged around the system's rotational axis, which produces the initial data for the 2D simulation. This technique has been employed with great success by [Fujibayashi et al. \(2017, 2018, 2020c, 2023\)](#) and [Shibata et al. \(2021\)](#). Based on these initial data, we perform two 2D simulations of the post-merger accretion-disk phase in a BNS merger. Unfortunately, we encounter a numerical instability in our fiducial model, which leads to a crash of the simulation after ~ 600 ms. Thus, this part of the thesis is still a work in progress.

This project was done together with Federico Guercilena and in collaboration with Bruno Giacomazzo, Wolfgang Kastaun, Takami Kuroda, and Martin Obergaulinger.

In Section 5.1, we describe the cartoon method which we use to realize a cylindrically symmetric simulation setup. We perform several tests of our implementation of the cartoon method which we describe in Section 5.2. In Section 5.3, we explain the creation of initial data for the post-merger simulations. Finally, we show the preliminary results of the two-dimensional simulations in Section 5.4.

5.1. The cartoon method

Simulations of axisymmetric systems in numerical relativity (NR) are typically based on curvilinear (typically cylindrical) coordinate systems which require the implementation of a mostly new code base (see, e.g., Section 2.4 of [Shibata, 2015](#), for more details). This is not only cumbersome but also problematic if the goal is to evolve the inspiral, merger, and post-merger phase of BNSs consistently because different codes might employ different approximations, e.g., for the treatment of neutrinos. The so-called “cartoon method” ([Alcubierre et al., 2001](#)) is a numerical technique to impose axisymmetry on a system while using Cartesian coordinates. It is therefore relatively straightforward to implement in an existing three-dimensional, Cartesian-coordinates-based code.

The cartoon method uses a Cartesian grid with a single interior cell in the y direction while the number of grid cells in the x and z directions are similar to what is typically used in 3D simulations. The physical domain thus only covers the xz plane. To be able to evaluate derivatives in the y direction, three layers of ghost zones are added on each side of the grid in the y direction. Figure 5.1 shows a slice of the computational grid parallel to the xy plane

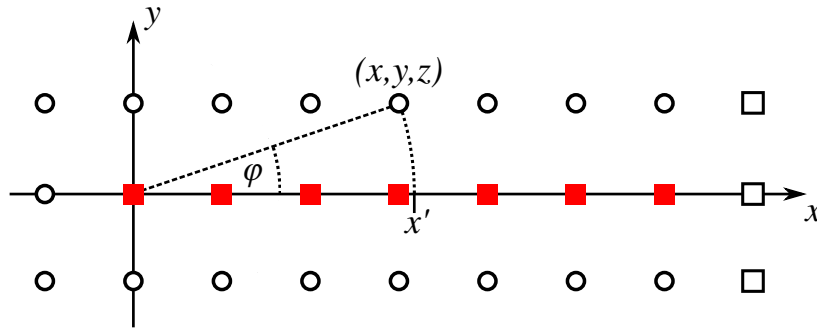


Figure 5.1.: Sketch of the cartoon method. Red squares, white squares, and white circles correspond to grid cells in the xz plane, cartoon ghost zones, and conventional ghost zones, respectively. Boundary conditions in the y directions are obtained by interpolation on the xz plane.

with red squares, white squares, and white circles corresponding to grid cells in the xz plane, cartoon ghost zones, and conventional ghost zones, respectively. Note that for simplicity, the number of grid points in the x direction is reduced and only one layer of cartoon ghost zones is shown. To mimic cylindrical symmetry the cartoon ghost zones are filled by rotating the data from the xz plan. The value of a scalar grid function A at the coordinates (x, y, z) in a cartoon ghost zone (i.e. $y \neq 0$) is given by

$$A(x, y, z) = A(x' := \sqrt{x^2 + y^2}, 0, z). \quad (5.1)$$

Evaluating the right-hand side usually requires interpolation on the x axis. Vector and tensor grid functions are treated the same way, except for the fact that a rotation around the z axis is applied before the interpolation step:

$$A^{ij\dots}(x, y, z) = R^i_{i'}(\phi) R^j_{j'}(\phi) \dots A^{i'j'\dots}(x', 0, z), \quad (5.2)$$

where $\phi = \arctan(\frac{x}{y})$ is the rotation angle and $R^i_j(\phi)$ is the corresponding rotation matrix.

The main downside of the cartoon method is the additional source of numerical error which is created by the interpolation step. Specifically problematic is the region close to the z axis. Most of the interpolation points x' are close to a grid point since x is usually much larger than the extent of the cartoon ghost zones y . However, for grid points close to the z axis, x and y are of comparable magnitude and the x' lie in the middle of two grid points on the xz plane. Interpolation routines can lead to large errors if a low-order interpolation scheme is used. For high-order schemes on the other hand, the Runge phenomenon (Runge, 1901) can become problematic in regions where the interpolated grid function has steep gradients. Since spacetime grid functions are typically smooth, their interpolations are well-behaved. Hydrodynamical quantities, however, can exhibit discontinuities, which can become problematic. This is usually not an issue, since Euler's equations can be evolved in cylindrical coordinates while the cartoon method is only needed for the evolution of the spacetime. Such an approach was for example used by Fujibayashi et al. (2017, 2018, 2020a,b,c, 2023) and Shibata et al. (2021). Unfortunately, there is no implementation of cylindrical coordinates in WhiskyTHC. Instead, we apply the cartoon method to both the hydrodynamical and the spacetime grid functions. Our implementation of the cartoon method draws upon the version found in the EinsteinToolkit Haas et al. (2020) which has been modified by Federico Guercilena.

5.2. Test cases

To gauge the accuracy of our implementation of the cartoon method for use with both hydrodynamical and spacetime variables, we select two test cases. The first tests the stability of the method by evolving flat space, constant density initial data over long time scales, in a way reminiscent of the robust stability test for spacetimes codes (Alcubierre et al., 2004). The second test case instead involves the simulation of an isolated cold NS and is meant to gauge the method's accuracy. The results of the two tests are presented in Sections 5.2.1 and 5.2.2.

5.2.1. Constant density

The computational domain for this test consists of a small region with $x_{\max} = z_{\max} \approx 24$ km. Initially, the domain is filled with a homogeneous stationary gas of density $\rho_0 \approx 6.18 \times 10^5 \text{ g cm}^{-3}$ modeled by the DD2 EOS (Banik et al., 2014). The spacetime variables are set to their flat space values, i.e., $\gamma_{ij} = \text{diag}(1, 1, 1)$, $\beta^i = K_{ij} = 0$, and $\alpha = 1$. Technically, this is not consistent with the hamiltonian constraint equation, Eq. (3.17) but the violation is very small as long as we choose a small initial density. This system should stay stationary during numerical evolution. We evolve this system with the cartoon method for approximately 500 ms. Figure 5.2 shows the evolution of the minimum and maximum density in the left panel and the evolution of the total baryon mass in the system in the right panel. The distribution of matter readjusts very slightly within the first ~ 60 ms. However, the density varies by less than 0.005 % during this time and the total baryon mass stays conserved up to 0.001%. Since the system acts as expected, we conclude that our numerical scheme produces a stable evolution.

5.2.2. Isolated neutron star

In this test case, we perform two simulations of an isolated cold non-rotating NS with a central density of $7.91 \times 10^{14} \text{ g cm}^{-3}$. The star is modeled by an ideal gas EOS with adiabatic index

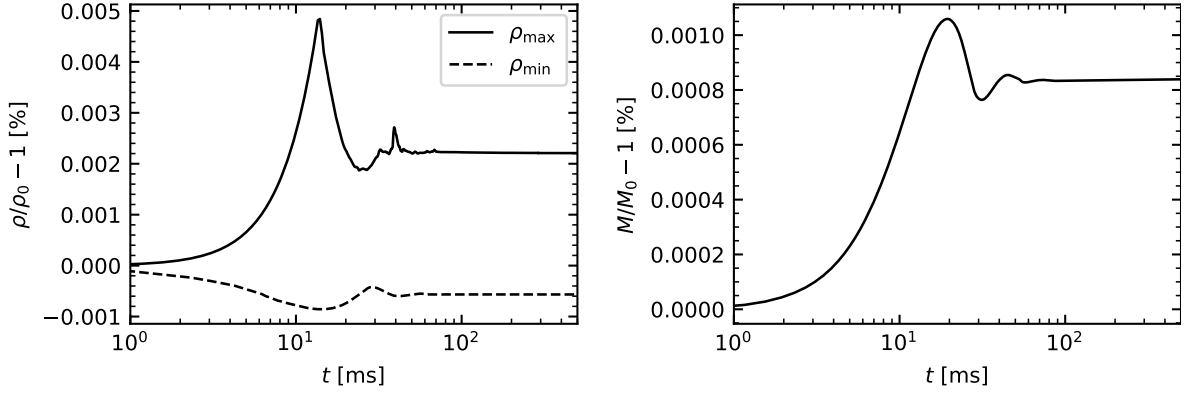


Figure 5.2.: Evolution of the minimum and maximum density (left panel) and total baryon mass in the domain (right panel) for the constant density test case. Both are normalized to their initial value.

$\Gamma = 2$ and polytropic constant $K = 100$. One simulation employs first-order and the other third-order Lagrangian interpolation for the cartoon method. In Figure 5.3, we show the change of the maximum density and total baryon mass in the simulation. In the simulation with first-order interpolation, the Tolman–Oppenheimer–Volkoff (TOV) star is oscillating, leading to a variation of $\sim 10\%$ in the central density. Furthermore, the violation of mass conservation is quite strong as $\sim 1.4\%$ of the total mass in the domain is lost within 100 ms. The central density in the simulation with third-order interpolation only varies by $\sim 5\%$ and the mass conservation is improved by almost an order of magnitude over the test with first-order interpolation. While this represents a noteworthy enhancement, it would be preferable to see an even smaller violation of mass conservation. This could potentially be achieved by higher order interpolation or the use of special interpolation methods, such as the ENO or WENO interpolation (Harten et al., 1987; Liu et al., 1994). For the time being, however, third-order interpolation is sufficient for a preliminary test simulation of a BNS post-merger system.

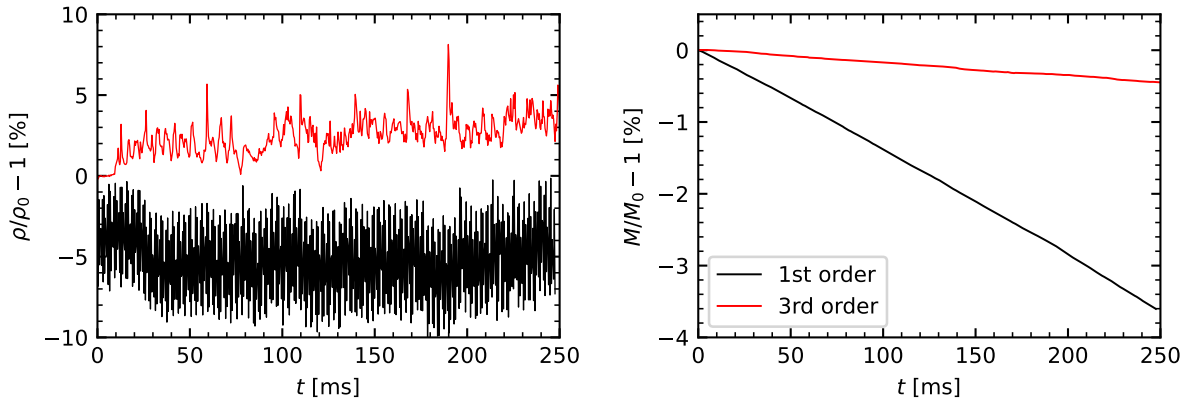


Figure 5.3.: Central density (left panel) and mass conservation (right panel) in the TOV test cases with first and third-order cartoon interpolation.

5.3. Realistic post-merger initial data

Since the inspiral and the merger of BNSs are intrinsically three-dimensional phenomena, they can not be simulated in axisymmetry. Instead, initial data of the remnant-torus system is needed. The methods typically used to create such initial data can be split into two categories: it can be either created by relying on analytic or semi-analytic models or by remapping data from a three-dimensional simulation.

Artificial initial data is typically created by imposing a hydrodynamical equilibrium configuration and by specifying certain parameters such as the mass and spin of the central object and the disk. Examples of such initial data where used in, e.g., [Fernández & Metzger \(2013\)](#); [Metzger & Fernández \(2014\)](#); [Just et al. \(2015\)](#); [Lippuner et al. \(2017\)](#); [Fernández et al. \(2020\)](#); [Fujibayashi et al. \(2020a,b\)](#); [Just et al. \(2021\)](#). Since these parameters can be chosen directly, this method can be better suited for studies that systematically investigate a large set of disk and remnant properties. However, these models often make several assumptions, such as constant electron fraction and/or entropy in the disk, which might not be justified.

The other type of method derives the initial conditions for the two-dimensional simulation directly from snapshots of three-dimensional simulations by averaging hydrodynamical quantities along circles around the z axis. This method preserves the realistic state of the disk and remnant, including the full radial and vertical distribution of the density, electron fraction, internal energy, and angular momentum. Therefore, the full evolution of the merger as well as the complete mass ejection history of the merger can be modeled consistently. The main disadvantage is that a 3D simulation has to be run for each BNS configuration and choice of microphysical parameters which is computationally expensive. Similar methods have been employed by [Dessart et al. \(2009\)](#) in simulations with Newtonian gravity and by [Fujibayashi et al. \(2017, 2018, 2020a, 2023\)](#), and [Shibata et al. \(2021\)](#) in full GR. In this study, we use initial data that is derived by averaging snapshots from three-dimensional simulations.

The initial data we intend to create has to specify the hydrodynamical state of the configuration, the geometric quantities specifying the gravitational field, and the gauge parameters. However, simply averaging all these quantities in the three-dimensional simulation and using them as initial values in the two-dimensional simulation leads to inconsistencies. The metric fields need to be consistent with the constraint equations (see Section 3.1.1) and the hydrodynamical state is constrained by the EOS. To fulfill these constraints we only need a limited number of hydrodynamical variables. Subsequently, the geometric variables can be derived by solving the general relativistic constraint equations Eqs. (3.17) and (3.18) and choosing gauge conditions. Finally, all other hydrodynamical quantities can be calculated from the EOS. We discuss the averaging procedure for the hydrodynamical variables in Section 5.3.1 and the procedure to determine the geometric variables in Section 5.3.2.

5.3.1. Hydrodynamical variables

The hydrodynamical state of the system can be specified by a set of variables that describe the rest-mass density, energy density, momentum density, and composition. For example, the primitive density ρ , electron fraction Y_e , temperature T , and 3-velocities v^i are possible choices and would be a good choice in a Newtonian simulation. In our case however, the conserved variables are a better choice, i.e., \tilde{D} , $\tilde{D}_p = Y_e \tilde{D}$, \tilde{E} , and \tilde{S}_i (see Section 3.2.1). This choice has two advantages: first, by fixing \tilde{S}_i , the momentum constraint equations decouple from

the conformal factor and can thus be solved without iteration (see Section 5.3.2); second, the integral of the averaged quantities should change only due to the source terms in Eq. (3.55) and should thus have the same value before and after the transition to 2D. This is specifically the case for the total baryon mass which is conserved and should thus be constant during both phases of the simulation. Furthermore, we need to average the six optical-depths grid functions $\tau_{(e,a,x)}^{(0,1)}$ (see Section 3.3) to specify the state of the neutrino leakage scheme. Finally, we also average $\tilde{S} = \sqrt{\gamma}S$, the trace of the hydrodynamical stress times the volume factor. In principle, S can be derived by performing a full recovery of the primitive variables but instead, we use the averaged \tilde{S} in solving the equations for the gauge condition. While this is an approximation, our tests have shown that it produces consistent results.

To average a variable defined on a three-dimensional Cartesian grid $A^{(\text{cart})}(x, y, z)$, the first step is to interpolate A onto a three-dimensional cylindrical grid $A^{(\text{cyl})}(r, \phi, z)$. If A is a vector or tensor quantity (e.g., A_{ij}) its components need to be rotated in this step:

$$A_{ij}^{(\text{cyl})} = R^{i'}_i R^{j'}_j A_{i'j'}^{(\text{cart})}, \quad (5.3)$$

where the R^i_j is the rotation matrix associated with ϕ . Next, the interpolated and rotated variable is averaged over the ϕ coordinate. The quantities \tilde{D} , \tilde{D}_p , \tilde{E} , \tilde{S}_i , and \tilde{S} are averaged directly:

$$\langle A \rangle(r, z) = \frac{1}{2\pi} \int_0^{2\pi} d\phi A(r, \phi, z), \quad (5.4)$$

while the optical depths are first weighted with the density \tilde{D} :

$$\langle \tau \rangle(r, z) = \frac{1}{2\pi \langle \tilde{D} \rangle} \int_0^{2\pi} d\phi \tau(r, \phi, z) \tilde{D}(r, \phi, z). \quad (5.5)$$

During a 3D simulation, the central object of the remnant can drift away from the coordinate origin. This can be caused by numerical errors or asymmetric mass ejection. To account for this, we shift the coordinate origin to the minimum of the lapse function before we perform the averaging procedure. We use the lapse function as a proxy for the center of mass of the system since it is typically smooth and therefore less susceptible to fluctuations.

5.3.2. Spacetime variables

Apart from the hydrodynamical quantities, the initial data has to contain information about the geometry of the spacetime, corresponding to initial values for the 3-metric γ_{ij} and the extrinsic curvature K_{ij} (see Section 3.1.1). Since both are symmetric tensors they have twelve independent components in total. There are four constraint equations, resulting in eight remaining degrees of freedom which need to be fixed. Furthermore, the gauge conditions need to be specified which determine the initial value for the gauge parameters α and β^i (see Section 3.1.3). This section details how these are calculated following the methods described in Shibata (1999) and Shibata (2015).

In the initial data creation we employ the conformal transverse traceless decomposition. We assume conformal flatness (i.e., the conformal decomposition is performed with with a flat conformal metric $\tilde{\gamma}_{ij} = \eta_{ij}$) and the absence of the trace and transverse part of the extrinsic

curvature. In Cartesian coordinates, the flat metric η_{ij} simply reduces to a Kronecker delta δ_{ij} . The 3-metric and the conformal metric are related by the conformal factor ψ :

$$\gamma_{ij} = \psi^4 \delta_{ij}, \quad (5.6)$$

where δ_{ij} is the flat space 3-metric. Since we employ Cartesian coordinates, the covariant derivative associated with the conformal metric $\tilde{\nabla}_i$ can be replaced by simple partial derivatives ∂_i and the corresponding Laplace operator $\tilde{\Delta} = \tilde{\nabla}^i \tilde{\nabla}_i$ can be replaced by the flat-space Lagrangian $\Delta = \delta^{ij} \partial_i \partial_j$. Next, we decompose the extrinsic curvature into its trace K and a traceless part A_{ij} :

$$K_{ij} = A_{ij} + \frac{1}{3} K \gamma_{ij} = \psi^{-2} \bar{A}_{ij} + \frac{1}{3} K \gamma_{ij}, \quad (5.7)$$

where \bar{A}_{ij} is a rescaling of A_{ij} with ψ^2 . Note that \bar{A}_{ij} is a different rescaling compared to the one used in the definition of the minimal distortion condition in Section 3.1.3. It can be decomposed further into a transverse part \bar{A}_{ij}^{TT} and a longitudinal part \bar{A}_{ij}^{L} (relative to the conformal metric $\tilde{\gamma}_{ij}$) which can be written in terms of a vector field W_i :

$$\bar{A}_{ij} = \bar{A}_{ij}^{\text{L}} + \bar{A}_{ij}^{\text{TT}} \quad (5.8)$$

$$\bar{A}_{ij}^{\text{L}} = \partial_i W_j + \partial_j W_i - \frac{2}{3} \tilde{\gamma}_{ij} \partial_k W^k \quad (5.9)$$

We assume that the trace and the transverse traceless part of the extrinsic curvature vanish ($K = 0 = \bar{A}_{ij}^{\text{TT}}$). The assumption of conformal flatness effectively reduces the number of undetermined components by five, since we specify the six components of γ_{ij} but introduce a new variable ψ . Furthermore, since \bar{A}_{ij}^{TT} is divergence-free ($\tilde{\nabla}^i \bar{A}_{ij}^{\text{TT}} = 0$) and traceless ($\tilde{\gamma}^{ij} \bar{A}_{ij}^{\text{TT}} = 0$) it is fully specified by two functions. Finally, $K = 0$ is a scalar equation and thus all eight free components are fixed. The remaining quantities are ψ and W_i which are determined by the constraint equations.

We can express the constraint equations in terms of the variables of the conformal transverse traceless decomposition and the conserved hydrodynamical quantities. The Hamiltonian constraint equation (3.17) becomes

$$\Delta \psi = 2\pi \tilde{E} \psi^{-1} - \frac{1}{8} \psi^{-7} \bar{A}_{ij} \bar{A}^{ij} \quad (5.10)$$

and the momentum constraint equations (3.18) become

$$\Delta W_i + \frac{1}{3} \partial_i \partial_j W^j = 8\pi \tilde{S}_i. \quad (5.11)$$

Following Shibata (1999), we simplify the expression (5.11) further by decomposing W_i into a vector potential B_i and a scalar potential χ by

$$W_i = \frac{7}{8} B_i - \frac{1}{8} \left[\partial_i \chi + (\partial_i B_k) x^k \right]. \quad (5.12)$$

The momentum constraint equations are then recast into two simple Poisson-type equations:

$$\Delta B_i = 8\pi \tilde{S}_i, \quad (5.13)$$

$$\Delta \chi = -8\pi \tilde{S}_i x^i. \quad (5.14)$$

To determine the gauge parameters we employ the maximal-slicing gauge condition for the lapse and the minimal-distortion condition for the shift vector (see Section 3.1.3). Together with the Hamiltonian constraint equation (5.10), the maximal-slicing gauge condition (3.28) becomes

$$\Delta(\alpha\psi) = 2\pi\alpha\psi^{-1}(\tilde{E} + 2\tilde{S}) + \frac{7}{8}\alpha\bar{A}_{ij}\bar{A}^{ij}\psi^{-7}. \quad (5.15)$$

Note that, in principle, $S = \rho h (W^2 - 1) + 3p$ should be consistently obtained from the EOS. However, this would require a full recovery of the primitive variables. Instead, we approximate \tilde{S} with the azimuthal average from the three-dimensional simulation Section 5.3.1).

The minimal distortion gauge condition can be expressed as

$$\delta_{ij}\Delta\beta^j + \frac{1}{3}\partial_i\partial_j\beta^j = J_i, \quad (5.16)$$

with

$$J_i := 16\pi\alpha\psi^{-6}\tilde{S}_i + 2\psi^{-6}\bar{A}_{ij}\delta^{jk}(\partial_k\alpha - 6\alpha\psi^{-1}\partial_k\psi). \quad (5.17)$$

Note that Eq. (5.16) has the same structure as Eq. (5.11) so we can apply the same decomposition as in Eq. (5.12):

$$\beta_i = \frac{7}{8}P_j - \frac{1}{8}(\partial_j\eta + (\partial_j P_k)x^k), \quad (5.18)$$

with the new auxiliary potentials P_i and η for which we obtain

$$\Delta P_i = J_i, \quad (5.19)$$

$$\Delta\eta = -J_i x^i. \quad (5.20)$$

Finally, we end up with ten Poisson-like equations: the Hamiltonian constraint equation (5.10), the momentum constraint equations (5.13) and (5.14), the gauge condition for the lapse (5.15) and the gauge condition for the shift (5.19) and (5.20). To solve these we employ the BiCgStab method (van der Vorst, 1992) where the cartoon method (see Section 5.1) is used to calculate partial derivatives in the y direction.

The full process for constructing the initial metric fields can be summarized as follows. We start by solving the momentum constraint equations Eqs. (5.13) and (5.14) to obtain χ and B_i . Since their source terms only depend on \tilde{S}_i , we can solve the equations directly. From χ and B_i we can recover W and thus \bar{A}_{ij} . Next, we solve the Hamiltonian constraint equation Eq. (5.10) to obtain ψ and Eq. (5.15) to obtain α . Since the source term in Eq. (5.10) depends on ψ and the source term in Eq. (5.15) depends on α , their solutions need to be calculated iteratively. Lastly, the shift is determined by solving Eqs. (5.19) and (5.20) and γ_{ij} and K_{ij} are recovered from ψ and \bar{A}_{ij} with

$$\gamma_{ij} = \psi^4\delta_{ij}, \quad (5.21)$$

$$K_{ij} = \psi^{-2}\bar{A}_{ij}. \quad (5.22)$$

model	EOS	neutrino treatment	t_{end} [ms]	M_{disk} [M_{\odot}]	M_{ej} [M_{\odot}]
DD2_2D	DD2	Leakage + M0	605.9	7.90×10^{-2}	5.79×10^{-3}
DD2_2D_no ν	DD2	none	618.9	1.56×10^{-1}	3.68×10^{-3}

Table 5.1.: List of the key features of the axisymmetric accretion disk models. Given are the total simulation time t_{end} , the disk mass M_{disk} after 400 ms, and the ejected mass M_{ej} after 600 ms.

5.4. Long-term post-merger simulations in 2D

We perform two long-term axisymmetric simulations to test the setup described in Sections 5.1 and 5.3. Table 5.1 lists the models and their key features. Since our methods are very similar to those presented in Fujibayashi et al. (2017, 2018, 2020c), we perform 2D simulations similar to the models labeled DD2-135M in Fujibayashi et al. (2020c), to compare our simulation setup with theirs. Specifically, the model DD2-135M-v0 is similar to our model DD2_2D because both models do not include a viscosity prescription. The initial data for our 2D simulations are based on a 3D simulation with the simulation setup described in Section 3.4. The simulation is based on the model DD2(high) presented in Sekiguchi et al. (2015) which was used for the creation of 2D initial data in Fujibayashi et al. (2017, 2018, 2020c). Our initial data is created from a snapshot taken ~ 55 ms after the merger. The corresponding 2D simulation is labeled DD2_2D in Table 5.1. Furthermore, we perform another 2D simulation with the same initial data but without neutrino emission or absorption, which we label DD2_2D_no ν .

In Section 5.4.1, we compare 2D the initial data to the 3D simulation it is based on. We analyze the evolution of the disk in Section 5.4.2 and the amount of ejected matter in Section 5.4.3. Unfortunately, the simulation DD2_2D crashes after ~ 600 ms. In Section 5.4.4 we describe the numerical instability that causes the crash and discuss possible solutions.

5.4.1. Comparison of the initial data

In the following section, we analyze the initial data produced for the model DD2_2D. Figure 5.4 shows the density in the xy plane of the 3D simulation in the iteration from which the 2D initial data was created. At this point, the massive NS has relaxed to a fairly axisymmetric configuration. The accretion disk is relatively axisymmetric as well, except for the presence of a spiral arm that results in a slightly asymmetric disk shape. The corresponding density distribution in the xz plane is shown in the top-left panel of Fig. 5.5. Several density jumps are visible in the disk due to the spiral wave. Furthermore, the region above the NS exhibits a turbulent mixture of inflowing and outflowing matter. The lower left panel shows the initial data in the 2D simulation. The matter distribution is well reproduced, except for the spiral waves and the turbulent flow in the polar direction, which are smoothed out. In Figure 5.6, we show the averaged 2D initial data along the equatorial plane, together with the corresponding profiles along the x axis of the snapshot from the 3D simulation. For better comparability, the coordinate origin of the 3D profiles is shifted to the minimum of the lapse, as described in Section 5.3. The top-left panel of figure Fig. 5.6 shows the conserved density \tilde{D} . Since the conserved variables are directly averaged, the profiles in 2D and 3D are very similar, especially in the center of the NS. In the outer layers, as well as in the accretion disk, the 3D data

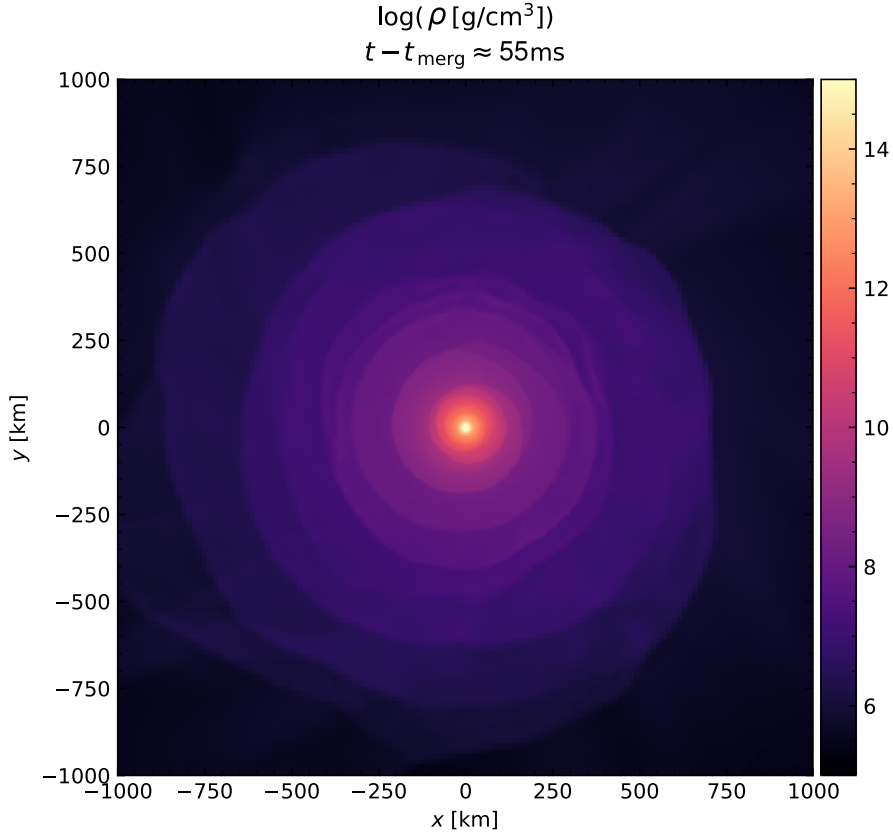


Figure 5.4.: Snapshot of the density in the xy plane of the 3D simulation before the transition to 2D. The distribution of the matter is approximately axisymmetric.

is not perfectly axisymmetric and thus shows some small deviations from the average. The top-right panel shows the conformal factor ψ . Since the 3D simulation is performed in the Baumgarte-Shapiro-Shibata-Nakamura (BSSN) formalism, we calculate the conformal factor as $\psi = e^\phi$, where ϕ is the conformal factor used in the BSSN formalism. Unlike the conserved density, the conformal factor is not directly averaged. Therefore, the profiles do not match exactly. This is expected for two reasons. As shown above, the averaging procedure removes some turbulent features and therefore, slightly reduces the momentum densities S_i . This affects the source terms in Eq. (5.11), and thus indirectly Eq. (5.10) for the conformal factor. Furthermore, the boundary condition for the conformal factor at a large distance from the remnant is given by $\psi = 1$ (or $\phi = 0$ in the case of the BSSN formulation). However, since the domain in the 2D simulation is much larger and the domain is cylindrical, the boundary conditions are effectively different compared to the 3D simulations.

After the initial data is created and the constraint and gauge equations are solved, the primitive density ρ is recovered by inverting Eq. (3.51). Since ψ differs between the 3D and 2D data, the primitive density ρ inside the NS is slightly larger in the 2D data. The center-left and center-right panels of Fig. 5.6 show the internal energy ε and the temperature T , respectively. The internal energy ε is slightly smaller in the 2D data than in the 3D data for reasons similar to those described above. While the difference is negligible for ρ or ε , the temperature inside the remnant is significantly affected. This can be explained by the following reasoning. In the NS

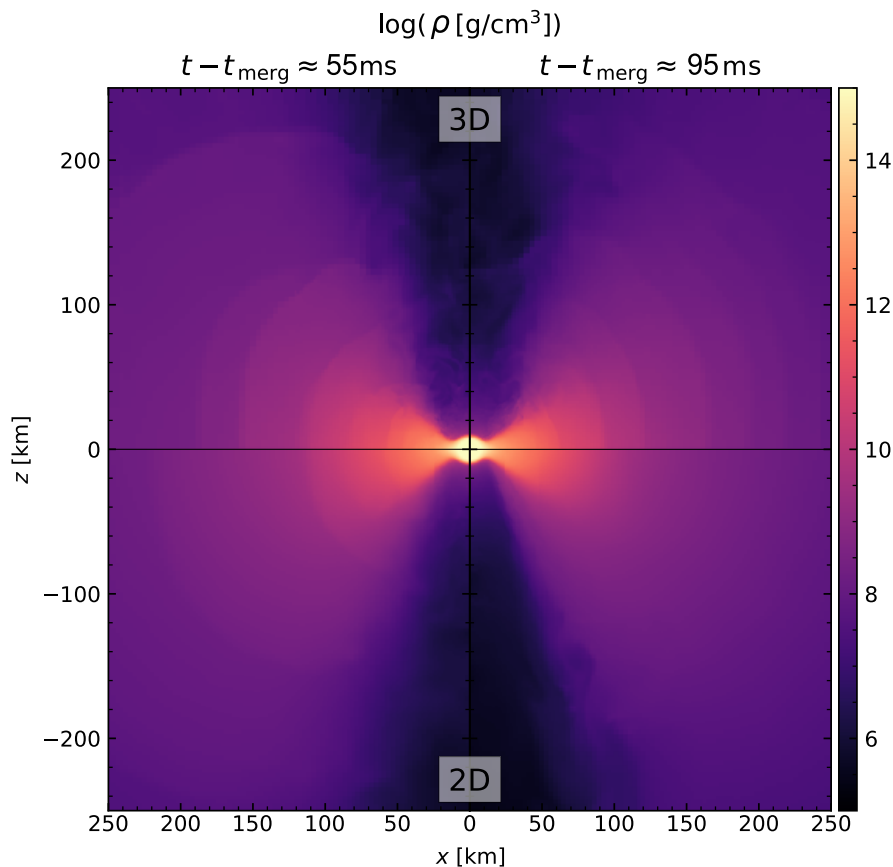


Figure 5.5.: Density distribution in the xz plane for the 3D and 2D models at the transition time step and 40 ms later. Top left: 3D simulation at the point of transition. Bottom left: 2D simulation initial data. Top right: 3D simulation 40 ms after the transition time step. Bottom right: 2D simulation initial data 40 ms after initialization.

center, the internal energy is dominated by the degeneracy energy, while the thermal energy is comparatively small. As the density is slightly lower in 2D, so is the degeneracy energy. At the same time, the total internal energy is slightly larger. Consequently, the thermal part of the internal energy, and hence the temperature, has to be much larger to compensate for the difference. This results in the temperature in the center of the NS being roughly twice as high as in the 3D data. However, this is not important for the dynamics of the system because the thermal contribution to the internal energy and pressure inside the NS core is negligible. Finally, the lower two panels of Fig. 5.6 show the distribution of the rotational velocity v^y and the distribution of the electron fraction Y_e . Both are reproduced well after the transition to 2D.

5.4.2. Evolution of the remnant

In Fig. 5.7, we show the evolution of several quantities for the models DD2_2D and DD2_2D_nov. Initially, the remnant is not in a perfect equilibrium state, due to the differences in the gauge choices during the creation of the initial data and the evolution with the BSSN formalism. Thus, it readjusts within the first 5-10 ms causing small oscillations in the massive NS. This can be

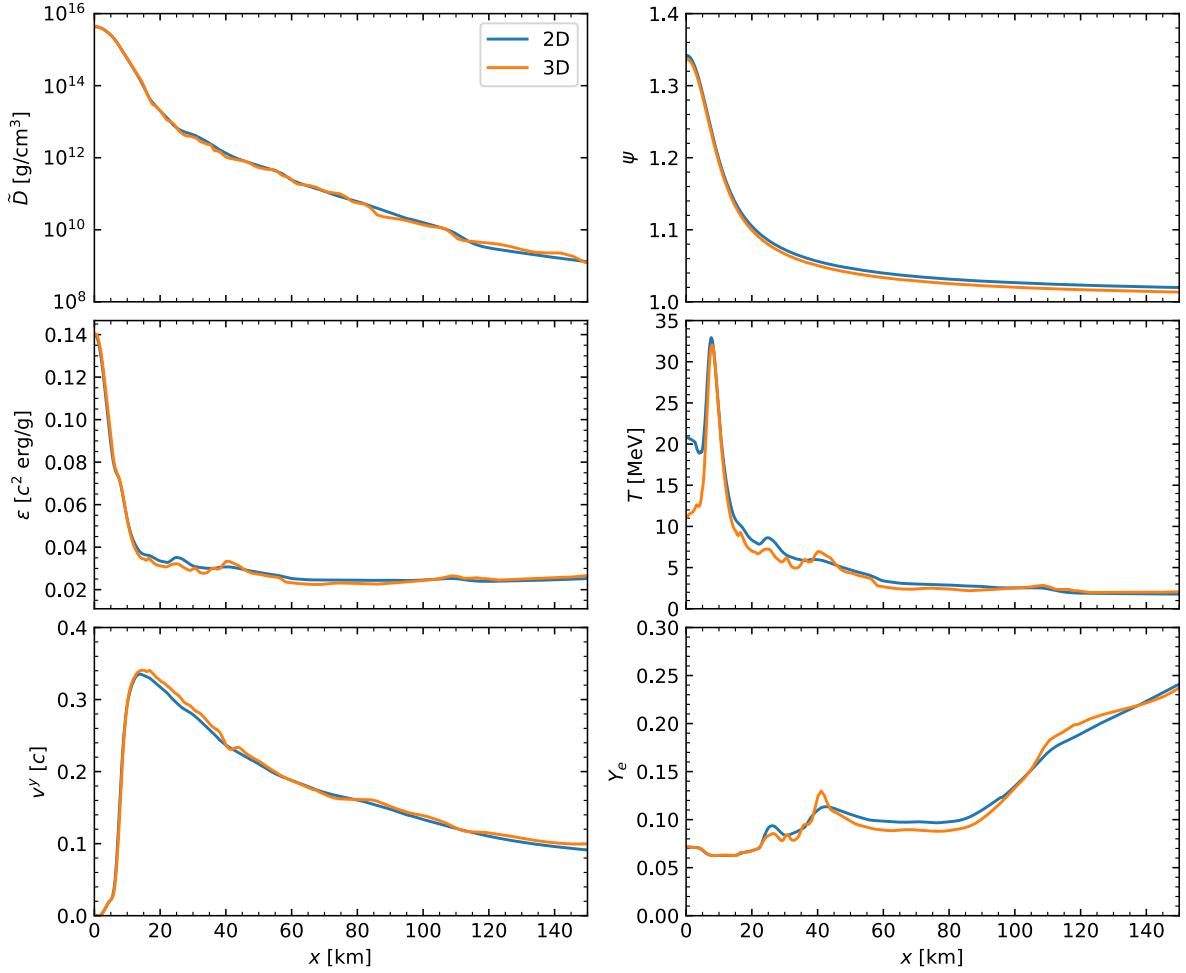


Figure 5.6.: Comparison of several quantities in the 2D initial data and the 3D simulation at the time of transition. From top left to bottom right: Conserved density, conformal factor, specific internal energy, temperature, rotational velocity, and electron fraction.

seen in the evolution of the maximum density and minimum lapse, shown in the top-left and top-right panels of Fig. 5.7, respectively. Though the change is small, the oscillations cause the ejection of matter, as described in Section 5.4.3.

To gauge if the evolution of the remnant is well reproduced by the 2D simulation, we compare the model DD2_2D with the 3D simulation it is based on. For this purpose, we continue the 3D simulation to $t - t_{\text{merg}} \approx 95$ ms. In the right panels of Fig. 5.5, we show the density distribution in the xz plane at the end of the 3D simulation together with the density in the 2D model, 40 ms after the start of the simulation. In both simulations, the vertical thickness of the accretion disk has shrunk slightly because neutrino emission reduces the disk temperature and therefore its pressure.

The density in the polar region is lower in the 2D simulation compared to the 3D simulation due to a fast outflow developing around the z axis in the 2D simulation. Figure 5.8 shows the radial velocity v^r for the models DD2_2D and DD2_2D_no ν 80 ms after the start of the simulation.

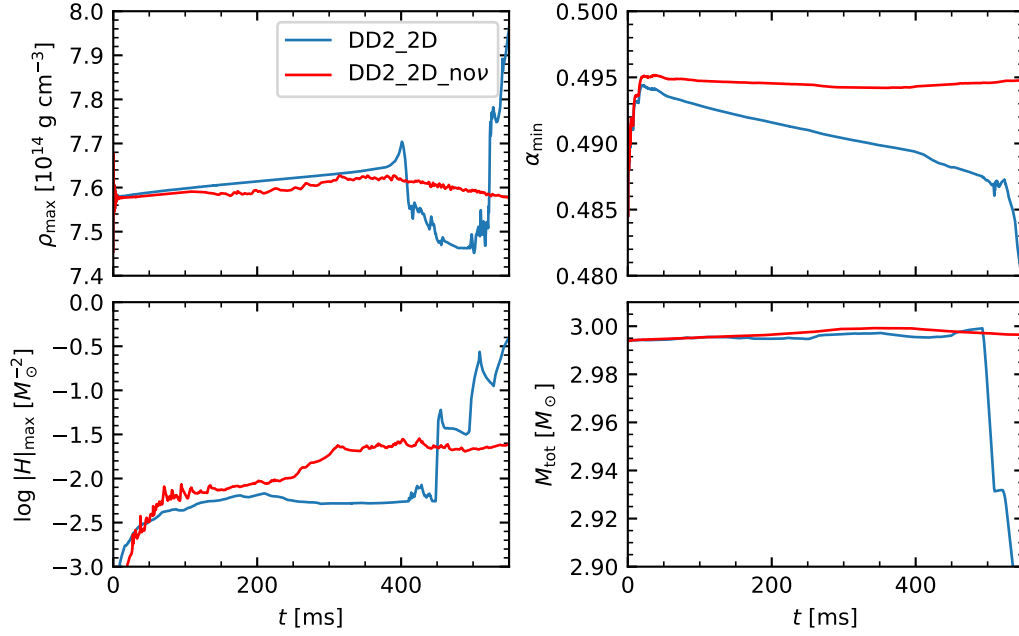


Figure 5.7.: Time series of several quantities detailing the instability, that arises in DD2_2D. Top left: maximum density, top right: minimum of the lapse function, bottom left: maximum of the absolute value of the Hamiltonian constrain violation H , bottom right: total baryon mass in the simulation domain.

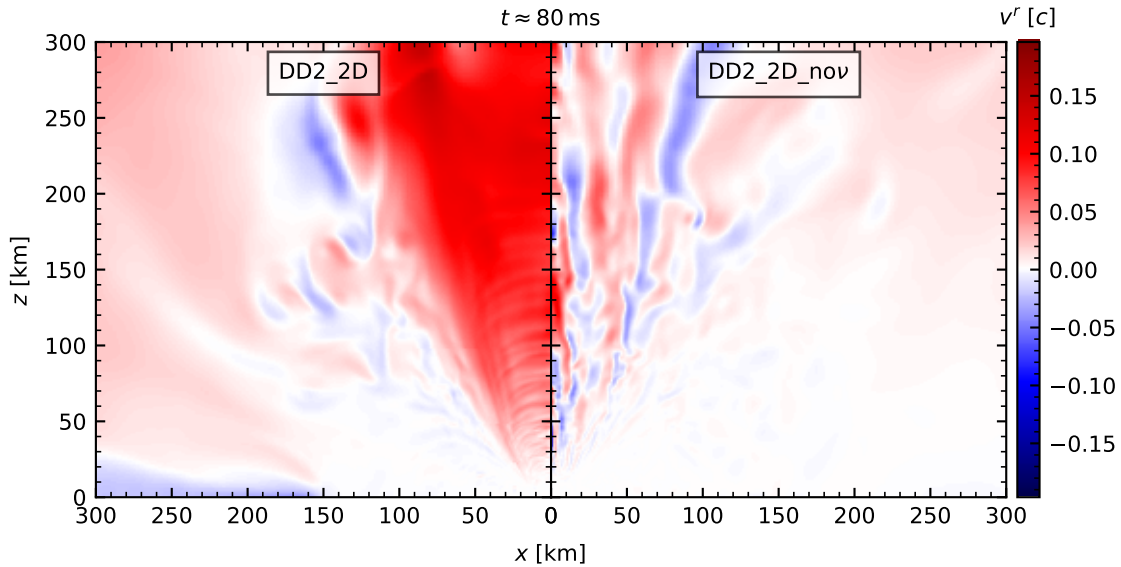


Figure 5.8.: Radial velocity in the simulations DD2_2D (left panel) and DD2_2D_nu (right panel).

The comparison shows that this outflow does not develop in the absence of neutrinos. We thus assume that it is driven by neutrino absorption. Note, that the density close to the z axis is

so low that the amount of matter ejected by this outflow is comparably small (see Fig. 5.11). Although neutrino-driven outflows also develop in 3D simulations, they typically do not form a continuous wind. Instead, the outflow is pulsed due to the asymmetry of the massive NS and the spiral arms in the disk, which can not exist in axisymmetric simulations. Moreover, 2D simulations are prone to launch outflows toward the polar directions due to the enforced symmetry. Thus, it is not surprising, that the 2D simulation develops a steady outflow, while the 3D simulation does not.

The evolution of the disk mass in DD2_2D and DD2_2D_nov is shown in the left panel of Fig. 5.9. Analogously to Fujibayashi et al. (2020c), we define the disk as all matter with density

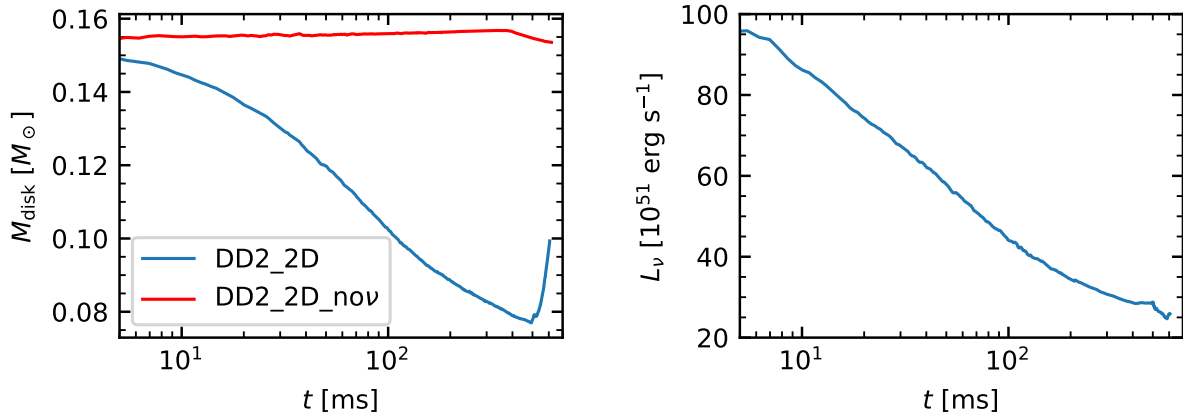


Figure 5.9.: Evolution of the disk mass (left panel) and the total neutrino luminosity (right panel) for DD2_2D and DD2_2D_nov. Note that the disk mass is defined as the mass of all matter with densities below $10^{12} \text{ g cm}^{-3}$, so it also includes the ejected matter.

below $10^{12} \text{ g cm}^{-3}$. Compared to the model DD2-135M of Fujibayashi et al. (2020c), the initial disk mass is $\sim 25\%$ lower in our model. Furthermore, in both their model and ours, about half of the disk is accreted onto the massive NS after ~ 500 ms (or more precisely into the region with $\rho > 10^{12} \text{ g cm}^{-3}$). Note that while a fraction of the disk is ejected, it is significantly smaller in comparison to the one that is accreted.

The right panel of Fig. 5.9 shows the total neutrino luminosity, i.e., the sum of the luminosities over all neutrino species. We find that the neutrino luminosity in our simulation is initially $\sim 25\%$ larger in our model DD2_2D compared to the model DD2-135M-v0 of Fujibayashi et al. (2020c). After 400 ms the luminosity has decreased by roughly 70% in both models. Note that Fujibayashi et al. (2020c) define the neutrino luminosities as the volume integral over the neutrino leakage rates, while we define it as the surface integral of the neutrino fluxes at $r \approx 750$ km. Thus, our definition includes the reduction of the luminosity due to neutrino absorption.

5.4.3. Mass ejection

Figure 5.10 shows the mass ejection rate and the total amount of mass ejected for the models DD2_2D and DD2_2D_nov, where the mass ejection rate is extracted by integrating the mass flux over the surface of a sphere with a radius of 8,000 km. In DD2_2D, the amount of ejected mass is roughly 2-3 times higher compared to DD2-135M-v0. This is most likely due to the

different ejecta content in the initial conditions. In our simulations, the initial conditions contain a substantial amount of ejecta that have not left the domain of the 3D simulation at the time of the transition. Figure Fig. 5.11 shows the mass ejection rate per polar angle $\frac{d}{d\theta}M^{\text{ej}}$ at $t \approx 80$ ms for both of our 2D models, where the mass ejection rate per polar angle is given by

$$\frac{d}{d\theta}M^{\text{ej}} = 2\pi (\alpha v^r - \beta^r) D \sqrt{\gamma} r^2 \sin \theta. \quad (5.23)$$

The large outer wave of ejecta is present in both DD2_2D and DD2_2D_no ν because it is driven by the initial conditions as described above. After the first burst, the mass ejection rate in DD2_2D_no ν drops off while a neutrino-driven outflow develops in DD2_2D. Figure 5.11 shows, that the ejection angles of the neutrino-driven ejecta are similar to the angles found for the early post-merger ejecta the 3D models in Section 4.3. The black dashed lines in Fig. 5.10 show the difference of the ejecta masses in DD2_2D and DD2_2D_no ν . Since the two models only differ in the neutrino treatment, the difference in their mass-ejection rate can be seen as a rough estimate of the purely neutrino-driven ejecta mass in DD2_2D. After 600 ms, the mass ejection rate in the model DD2-135M-v0 of Fujibayashi et al. (2020c) has dropped to $10^{-3}M_{\odot} \text{ s}^{-1}$. At the end of our simulations, however, the neutrino-driven outflow is still ongoing and the mass ejection rate is still high ($\sim 5 \times 10^{-3}M_{\odot} \text{ s}^{-1}$). This is most likely due to differences in the neutrino treatment.

5.4.4. Instability

As mentioned above, the simulation DD2_2D crashes after ~ 600 ms due to an instability that develops in the center of the NS. It can be first seen in the evolution of the maximum density in Fig. 5.7, which suddenly increases after ~ 390 ms and afterward abruptly drops. The lower left panel of Fig. 5.7 shows the constraint violation stays relatively low, even after 400 ms and only later becomes large. This points toward a failure caused by the hydrodynamical evolution of the system. Figure 5.12 shows the development of the density inside the NS core in detail: The central density rises by a few percent (top panels) and subsequently drops (bottom-left

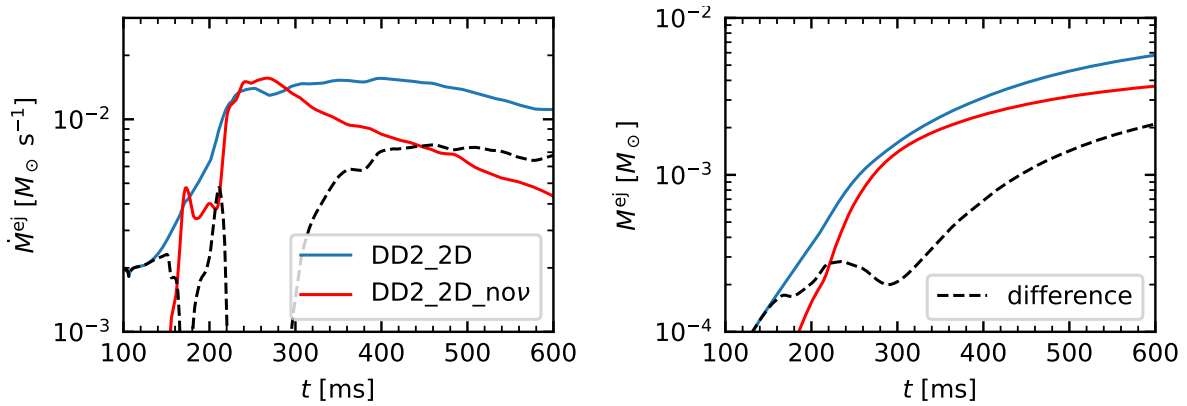


Figure 5.10.: Mass ejection rate (left panel) and total amount of mass ejected as a function of time (right panel). The dashed black lines show the difference between the models DD2_2D and DD2_2D_no ν .

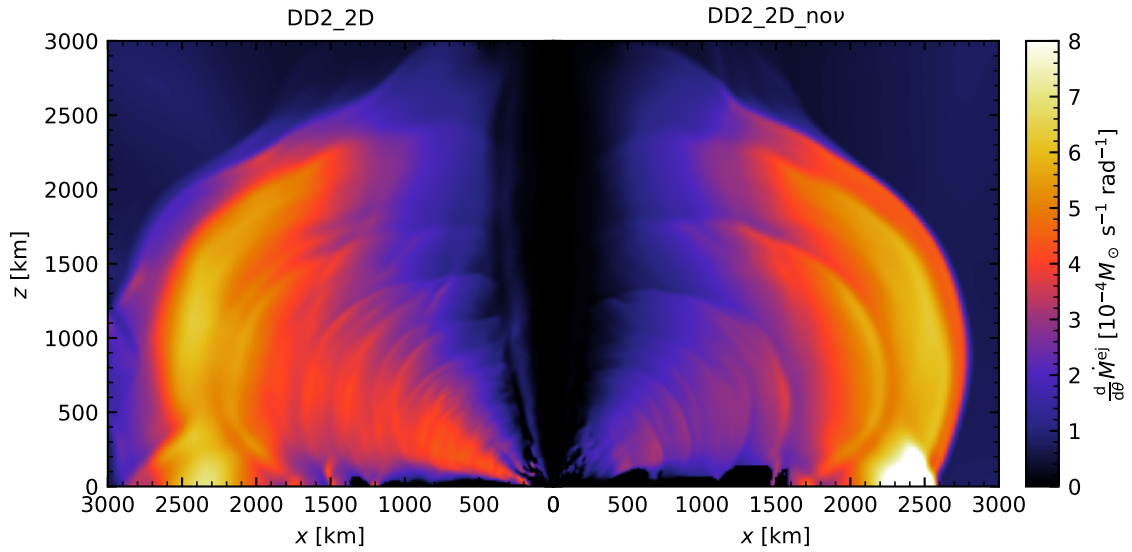


Figure 5.11.: Mass ejection rate per polar angle for DD2_2D and DD2_2D_nov at $t \approx 80$ ms.

panel). This causes large unphysical density oscillations (bottom-left panel) that eventually disrupt the NS (bottom-right panel). Eventually, the conservation of the total baryon mass in the simulation is violated, as can be seen in the bottom-right panel of Fig. 5.7. We are unsure what causes this instability and plan to further investigate it in the future.

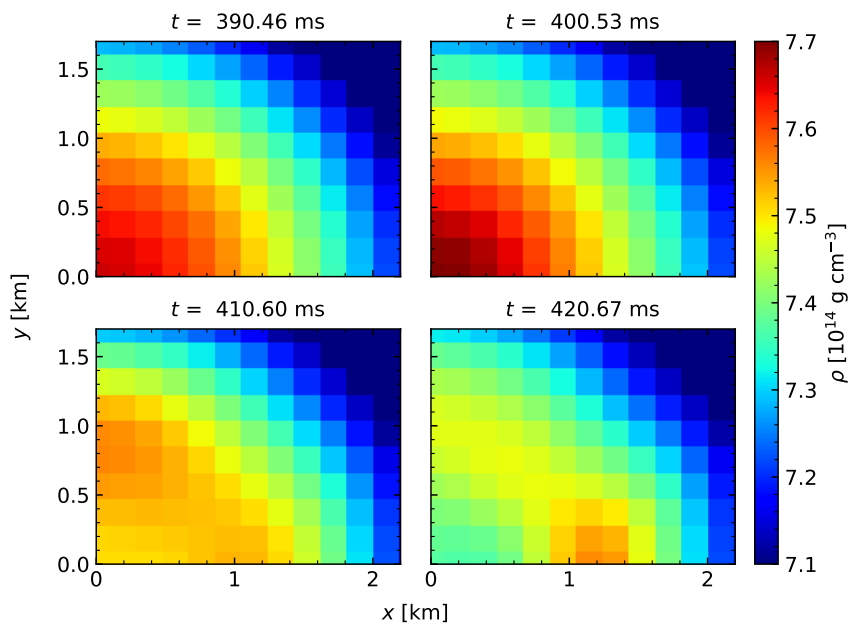


Figure 5.12.: Snapshots of the instability developing in the density.

Once these issues have been addressed, our framework will allow us to extend 3D simulations to multiple seconds. In this way, we will be able to consistently obtain the full mass ejection history of BNS mergers. This is essential for assessing the full abundance pattern of the ejecta and therefore potential features in the KN lightcurve and spectrum and to understand the role of mergers in the r -process enhancement of galaxies. Thus, we plan to connect the project discussed in Chapter 4 with the 2D simulation framework, which will enable us to gauge the influence of the EOS on the full post-merger mass ejection.

6. Summary and outlook

Merging binary neutron stars are unique and exciting events, not only for astrophysicists but also astronomers, nuclear physicists, and particle physicists. These cataclysmic events emit gravitational waves (GWs) and result in the ejection of neutron-rich material. This material undergoes r -process nucleosynthesis, leading to the production of heavy elements and the kilonova (KN). The GW waveform and the KN lightcurve and spectrum depend sensitively on the nuclear equation of state (EOS). This makes binary neutron star (BNS) mergers very useful for studying the EOS by comparing the predictions of numerical models with multi-messenger observations. However, at the same time, it means that knowledge of the EOS is vital for our understanding of the role of BNS mergers in the r -process enrichment of galaxies. Therefore, a systematic approach is needed to characterize the effect of the EOS on the merger and post-merger dynamics. Moreover, to obtain a complete picture of the ejecta properties of BNS mergers and their dependence on the EOS, it is imperative to simulate all phases of matter ejection consistently, including the post-merger accretion-disk phase.

In the first part of the thesis, we systematically investigated the influence of different nuclear matter properties in BNS-merger simulations. To this end, we employed 8 different Skyrme-based EOS models. We used the LS220 Skyrme parameters as fiducial model (Lattimer & Swesty, 1991) and systematically changed the effective mass, incompressibility, symmetry energy, and nuclear saturation point. A BNS merger simulation was performed for each EOS and analyzed the merger dynamics, the GW signal, and the properties of the dynamical ejecta. In this way, we were able to directly assess the impact of the nuclear matter properties on the merger and the associated multi-messenger observables.

A special focus was set on the effective mass and the incompressibility. Increasing the incompressibility or decreasing the effective mass increases the overall pressure inside neutron stars (NSs), i.e., it makes the EOS stiffer. The effective mass impacts the pressure at all densities inside the NS while the incompressibility mostly influences the pressure at very high densities, i.e., in the innermost core of NSs. Both parameters directly impact whether the merger remnant promptly collapses to a black hole (BH) or the time until a delayed BH formation. Furthermore, our results showed that the post-merger GW peak frequency is correlated to both parameters.

Our findings indicate that several aspects of the merger dynamics exhibit a correlation only with one of the parameters. Specifically, we discovered that larger incompressibilities result in a more rapid cessation of the NS contraction and a quicker transition to a one-armed spiral-wave mode, which has implications for the emission of GWs and the ejection of matter during the early post-merger phase. In contrast, increasing the effective mass does not exhibit the same dampening effect. Additionally, we analyzed the dependence of the dynamical ejecta mass on the EOS. To this end, we separated the tidal and shock-heated ejecta components, as they are expelled through distinct mechanisms and thus depend differently on the EOS. Our findings reveal that the amount of matter ejected through tidal forces increases significantly with larger

incompressibilities and only slightly with smaller effective masses. Conversely, the mass of the shock-heated ejecta decreases with smaller effective masses, but does not display a correlation with the incompressibility. These results demonstrate that certain dynamics in an BNS merger depend on specific density regimes of the EOS. We thus conclude that the stiffness of an EOS needs to be viewed as a density-dependant property, i.e., an EOS can be soft at lower densities (e.g., close to the saturation density) but stiff at large densities.

Furthermore, we assessed whether the nuclear matter properties at saturation density accurately describe the influence of the EOS on BNS mergers. To this end, we employed a Skyrme functional based on the Shen EOS (Shen et al., 1998a) that was first used in Yasin et al. (2020). The resulting SkShen EOS exhibits the same saturation point and matches the Shen EOS' effective mass, incompressibility, and symmetry energy at saturation density. Thus it is similar to the Shen EOS at the saturation density but diverges at high densities. Despite these differences, the remnant evolution and the amount of matter ejected in the SkShen and Shen EOS models are relatively similar, and their post-merger GW spectrum is almost identical.

This study showed the potential of our method for examining the relationship between the detailed features of the EOS and the merger outcome. However, further simulations with more variations of the EOS parameters will be required to validate the trends we found and to make quantitative statements. Our study was restricted to symmetric BNS systems, so it will be interesting to investigate asymmetric configurations as well.

The second part of this thesis focuses on simulating BNS mergers over several seconds. A significant amount of the material ejected during a BNS merger originates from the post-merger accretion disk. However, it is currently not feasible to simulate the entire post-merger phase and matter ejection in three dimensions due to the immense computational cost. To address this issue, we have implemented a simulation framework based on the cartoon method, which allows us to simulate axisymmetric systems using the same code as in the 3D simulations while significantly reducing computational resources.

In order to derive axisymmetric initial conditions of the post-merger remnant, we averaged 3D hydrodynamic quantities around the rotational axis at 55 ms post-merger and consistently construct the metric fields in the conformal flat approximation. This enables us to consistently extend BNS-merger simulations until the end of the post-merger phase without the need for excessive computational power. As a test of our implementation, we applied this method to a simulation of a neutron-star accretion-disk system resulting from a symmetric BNS merger. Our results align with previous studies in the literature. However, we found the ejected matter to be significantly larger, possibly due to differences in the way we treated neutrinos. Unfortunately, we encountered numerical difficulties that must be resolved before our setup can be used for further studies. Additionally, the primary mechanism for mass ejection in the post-merger phase is viscous heating caused by magneto-hydrodynamical (MHD) effects, which are typically approximated by a viscosity prescription. Therefore, it will be necessary to incorporate a viscous heating scheme into our simulation setup. With these advancements, we will be able to follow the whole mass-ejection history of BNS mergers. This will enable us to investigate the influence of the EOS on the r -process enhancement of the universe.

In the near future, the rapid advancement in the field of compact-object merger simulations, along with the potential of new multi-messenger observations, will lead to significant advances in our understanding of the EOS at extremely high densities as well as the role of neutron star

mergers in the production of heavy elements. The fourth observing run of LIGO, Virgo, and Kagra, which is set to begin in May of this year, is anticipated to detect the GW signal of multiple BNS mergers. It is projected that a few of these detections will also include the post-merger signal and maybe in some cases they will be accompanied by the observation of a KN transient. To effectively constrain the nuclear EOS from future multi-messenger observations, it is crucial to explore its role in BNS mergers in more detail through numerical simulations that encompass both the merger and post-merger accretion-disk phase. Our research presents novel ways to quantify the influence of the EOS in BNS mergers and contributes to a better understanding of their relationship to the properties of nuclear matter.

Appendices

A. Fluid tracers

Nucleosynthesis calculations are usually performed following escaping fluid elements in a Lagrangian picture (i.e. in a frame commoving with the fluid). The Lagrangian description offers two main benefits: The abundances of synthesized nuclei are simply advected with the fluid, i.e., except for changes due to nuclear reactions, they are conserved in a Lagrangian frame, except for changes due to nuclear reactions. Furthermore, if ejecta escape the simulation domain or the simulation is stopped, no further information about the thermodynamic history of the ejecta is available, even though r -process nucleosynthesis takes place on much longer timescales. However, the expansion of a fluid element that has escaped from the remnant can be reasonably well approximated under the assumption of adiabatic homologous expansion.

The transition from the Eulerian picture of the grid-based simulations to a Lagrangian description is usually made with so-called tracer particles – massless particles that do not interact with the fluid except for being advected by it. The path of each tracer particle is obtained by integrating the advection-velocity field $V^i = \alpha v^i + \beta$. The temperature, density, and other relevant quantities are recorded along the path by interpolation. The path along with the recorded quantities is usually referred to as trajectory. Explosive nucleosynthesis calculations are performed with a reaction network code that uses trajectories as input (see, e.g., [Hix & Thielemann \(1999\)](#), for an overview of reaction networks). By performing network calculations for a large number of tracer particles, the full nucleosynthesis in the ejecta can be determined. Calculating the total mass-averaged abundance pattern or the heating rate due to nuclear reactions requires that a mass is assigned to each tracer.

An important question is how many tracers are necessary to track the fluid’s movement with enough resolution. While tracer particles are treated as point masses, they are meant to represent a small but finite volume of the fluid. Furthermore, as the tracer is advected, this volume deforms and is potentially “spaghettified” by turbulent fluid motion. After some time, the fluid element might be so spread out that it can not be represented by a point-like tracer anymore. To overcome this issue, the number of tracers needs to be high enough to properly resolve the fluid and the distribution across the fluid needs to be even.

There are two choices when it comes to the integration of the tracer paths: Either one initializes the tracers at the beginning of the simulation and calculates their movement during the simulation (in situ) (see, e.g., [Bovard et al., 2017](#)) or one uses the output of the simulation to evolve the tracers in post-processing (see, e.g., [Fujibayashi et al., 2020a](#)). Usually, the state of the fluid is not saved in every iteration of the simulation, since this would require a very large amount of storage space. Instead, the output is saved in fixed intervals of ~ 1 ms. Therefore, the in-situ evolution of the tracers is more accurate while the accuracy of the post-processing method relies on the timestep of the simulation output. The downside of the in-situ method is, that there is no way to predict, which regions of the initial NSs will be ejected, so the tracers must be distributed evenly in the outer regions of the NSs. This results in most of the tracers still being bound inside the remnant at the end of the simulation. Thus, a very large number of

tracers needs to be placed initially, to ensure that the ejecta are properly resolved. Moreover, if a part of the ejecta ends up being underresolved, it cannot be corrected without rerunning the simulation from the moment of tracer initialization on.

When the tracers are calculated in post-processing, one can select the initialization point freely. Specifically, tracer particles can be initialized at the end of their trajectory and integrated backward in time. This guarantees, that all the ejecta are sufficiently well resolved by tracer particles. Furthermore, if the only purpose of the tracer particles is to calculate the nucleosynthesis in the ejected matter, the integration can be stopped once the fluid element reaches temperatures high enough to be considered in β -equilibrium (usually 10 GK). This reduces the fluid element distortion described above for the following reasons: First, the evolution of the tracers is as short as possible. Second, the density of the tracers generally increases during the integration and therefore the volume it represents shrinks. Third, the fluid motion outside of the remnant is usually less turbulent. The last point also means that the post-processing method's lower time resolution is not as problematic since the trajectories of the tracers are more linear. In summary, integration backward in time is the best method for calculating tracers in post-processing. This conclusion was also reached by [Sieverding et al. \(2023\)](#) in the context of supernova simulations. Note, however, that the tracer particle method can also be used to analyze the fluid motion in the post-merger remnant (see, e.g., [Bovard & Rezzolla, 2017](#); [Kastaun et al., 2016](#)). In this case, the high time resolution of in-situ tracers is necessary to follow the complicated turbulent fluid motion.

If the duration of the simulation is long and/or the simulated domain is small, the ejected matter might escape the simulation before its end. In this case, simply initializing all tracers at the last simulation step neglects potentially large parts of the ejecta. We, therefore, initialize tracers in regular intervals Δt on a sphere with a large radius R and determine the mass of the tracers based on the radial mass flux at their initial position,

$$\frac{dm}{d\Omega} = R^2 Dv^r \Delta t, \quad (\text{A.1})$$

where we have assumed that $\alpha \approx 1$ and $\beta^i \approx 0$ at large distances from the remnant. Each tracer represents an area or cell on the sphere with a solid angle $\Delta\Omega = \sin\theta\Delta\theta\Delta\phi$, where θ and ϕ are the polar and azimuthal angles, respectively. The tracer mass is obtained by integrating Eq. (A.1) over the cell represented by the tracer. A similar approach is used by the authors of [Fujibayashi et al. \(2020a\)](#). At the end of the simulation, we initialize a second set of tracers inside the sphere of radius R where their mass is assigned based on the local density. This way, we capture all of the ejected matter while still being able to use backward time integration.

Two paradigms exist for the distribution of tracers at the initialization step: Either the tracer density is constant or it is correlated to the local mass density. In the first case, all tracers represent roughly the same volume, in the second case they represent roughly the same mass. On one hand, it is intuitive to assign each tracer the same amount of mass, since this way, each tracer contributes equally to the final abundance pattern. On the other hand, the production of some elements can exclusively take place in low-density regions, which would be underresolved if the tracer distribution was based on density. We, therefore, use the following prescription to set the initial position of the tracers:

1. Distribute the tracers on the sphere with even spacing in ϕ and in $\cos(\theta)$. This way, each tracer initially represents the same solid angle $\Delta\Omega = \sin(\theta)\Delta\phi\Delta\theta$.

2. Associate a mass m to all tracers by integrating Eq. (A.1) over the area on the sphere represented by the tracer.
3. Replace each tracer with $m > m_{\text{thresh}}$ by 4 new tracers, where m_{thresh} is a constant threshold mass.
4. Repeat the previous step until the mass associated with all tracers is smaller than m_{thresh} .
5. Shift the initial position of each tracer by a random within its area on the sphere.

The threshold mass is adjusted, such that the procedure detailed above results in roughly the desired number of tracers. Finally, we randomly shift each tracer within its cell to get rid of the artificially directional bias created by the regular grid introduced in step 1. This results in a distribution where all tracers represent at most a mass of m_{thresh} , but the resolution in low-density regions is still reasonably high. Note that it is important for the scheme, that the integration in step 2 is based on multiple points for each tracer since the initial distribution of tracers is quite coarse. Thus, large fractions of the ejecta mass can be neglected if Eq. (A.1) is only evaluated in the center of the cell represented by the tracer.

The same prescription is used for the batch of tracers distributed within the domain at the last timestep of the simulation, with the following exceptions: tracers are initially equally spaced in x , y , and z , their mass is assigned by integrating the density over the volume they represent, and, if a tracer’s mass is above m_{thresh} , it is split into 8 new tracers instead of 4.

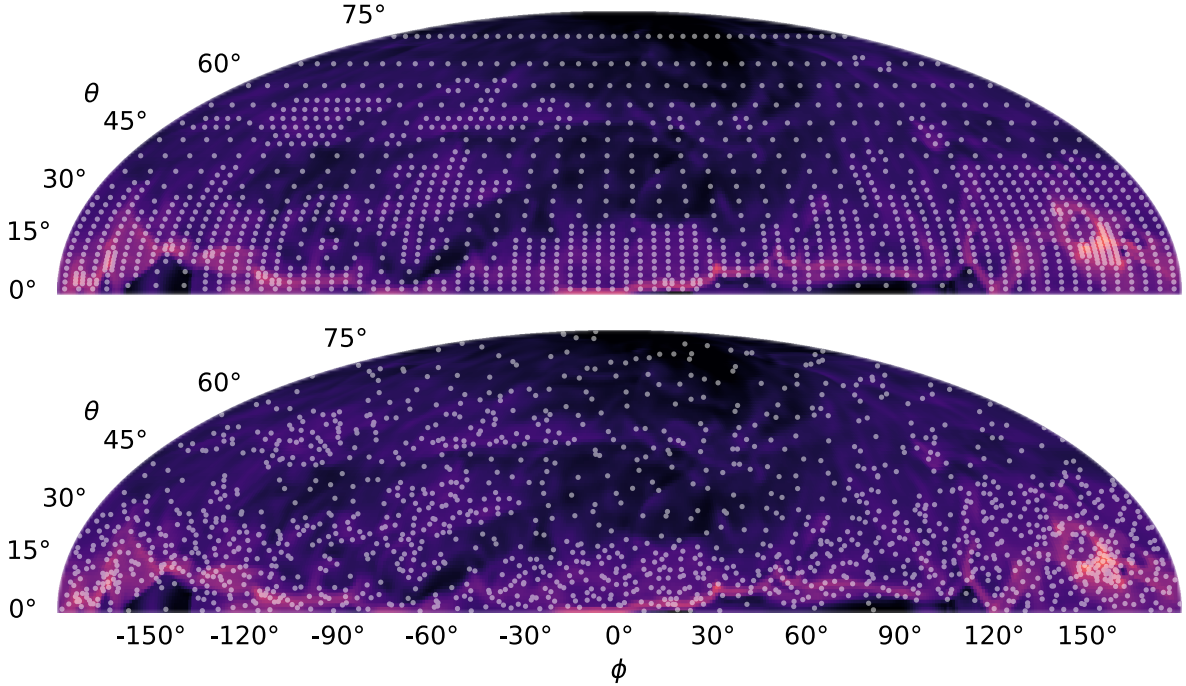


Figure A.1.: Distribution of tracers ejected at $t - t_{\text{merg}} = 30 \text{ ms}$ on a “Mollweide” projection of the northern hemisphere in the model LS255[†]. The heatmap shows the radial mass flux per unit area. Top and bottom panels show the tracer distribution before and after the random shift is applied, respectively.

Figure [A.1](#) shows an example of the distribution of ~ 1500 tracers resulting from the algorithm outlined above. The tracers are distributed on the surface of a sphere at ~ 1500 km at $t - t_{\text{merg}} = 30$ ms in the model LS255[†] (see Section [4.1.1](#)). The top and bottom panels show the tracer distribution before and after the random shift (step 5) is applied, respectively. The heatmap corresponds to the radial mass flux per unit area, Eq. ([A.1](#)). The tracer density is higher in the equatorial regions with higher mass ejection rates but still high enough in the regions with low mass ejection rates.

The time evolution of the tracer trajectories is performed with the explicit Runge-Kutta method of order 5 presented in [Dormand & Prince \(1980\)](#) and implemented in the `solve_ivp` method of the SciPy python package ([Virtanen et al., 2020](#)). The relevant hydrodynamical quantities are interpolated in space and time using linear interpolation.

Bibliography

- Abbott, B. P., Abbott, R., Abbott, T. D., et al. 2016, [PhRvL](#), 116, 61102
- . 2017a, [ApJ](#), 848, L12
- . 2017b, [PhRvL](#), 119, 161101
- . 2018, [PhRvL](#), 121, 161101
- . 2019, [PhRvX](#), 9, 011001
- Alcubierre, M., Brügmann, B., Holz, D., et al. 2001, [IJMPD](#), 10, 273
- Alcubierre, M., Allen, G., Bona, C., et al. 2004, [CQGra](#), 21, 589
- Alford, M. G., Han, S., & Schwenzler, K. 2019, [JPhG](#), 46, 114001
- Andreoni, I., Ackley, K., Cooke, J., et al. 2017, [PASA](#), 34
- Antoniadis, J., Freire, P. C. C., Wex, N., et al. 2013, [Sci](#), 340, 1233232
- Arcavi, I., Hosseinzadeh, G., Howell, D. A., et al. 2017, [Nature](#), 551, 64
- Arcones, A., & Martínez-Pinedo, G. 2011, [PhRvC](#), 83, 045809
- Arnowitt, R., Deser, S., & Misner, C. W. 2008, [GReGr](#), 40, 1997
- Arzoumanian, Z., Brazier, A., Burke-Spolaor, S., et al. 2018, [ApJS](#), 235, 37
- Baade, W., & Zwicky, F. 1934, [PhRv](#), 46, 76
- Baiotti, L. 2019, [PrPNP](#), 109, 103714
- Balbus, S. A., & Hawley, J. F. 1991, [ApJ](#), 376, 214
- Banik, S., Hempel, M., & Bandyopadhyay, D. 2014, [ApJS](#), 214, 22
- Banyuls, F., Font, J. A., Ibanez, J. M., Martí, J. M., & Miralles, J. A. 1997, [ApJ](#), 476, 221
- Barnes, J., Kasen, D., Wu, M.-R., & Martínez-Pinedo, G. 2016, [ApJ](#), 829, 110
- Baumgarte, T. W., & Shapiro, S. L. 1998, [PhRvD](#), 59, 024007
- . 2021, *Numerical Relativity: Starting from Scratch* (Cambridge: Cambridge University Press)
- Bauswein, A., & Janka, H.-T. 2012, [PhRvL](#), 108, 011101

- Bauswein, A., Janka, H.-T., Hebel, K., & Schwenk, A. 2012, [PhRvD](#), 86, 063001
- Bauswein, A., Janka, H.-T., & Oechslin, R. 2010, [Phys. Rev. D](#), 82, 084043
- Bauswein, A., & Stergioulas, N. 2015, [PhRvD](#), 91, 124056
- Bauswein, A., Stergioulas, N., & Janka, H. T. 2016, [EPJA](#), 52
- Berger, M. J., & Colella, P. 1989, [JCoPh](#), 82, 64
- Berger, M. J., & Olinger, J. 1984, [JCoPh](#), 53, 484
- Bernuzzi, S. 2020, [GReGr](#), 52, 108
- Bernuzzi, S., Dietrich, T., Tichy, W., & Brüggmann, B. 2014, [PhRvD](#), 89, 104021
- Blanchet, L. 2014, [LRR](#), 17, 2
- Blandford, R. D., & Znajek, R. L. 1977, [MNRAS](#), 179, 433
- Blaschke, D., & Chamel, N. 2018, in *The Physics and Astrophysics of Neutron Stars*, ed. L. Rezzolla, P. Pizzochero, D. I. Jones, N. Rea, & I. Vidaña, Vol. 457 (Cham: Springer International Publishing), 337–400, doi: [10.1007/978-3-319-97616-7_7](#)
- Bovard, L., Martin, D., Guercilena, F., et al. 2017, [PhRvD](#), 96, 124005
- Bovard, L., & Rezzolla, L. 2017, [CQGra](#), 34
- Brown, D., Diener, P., Sarbach, O., Schnetter, E., & Tiglio, M. 2009, [PhRvD](#), 79, 044023
- Brown, J. D. 2009, [PhRvD](#), 79, 104029
- Buonanno, A., & Damour, T. 1999, [PhRvD](#), 59, 084006
- Burbidge, E. M., Burbidge, G. R., Fowler, W. A., & Hoyle, F. 1957, [RvMP](#), 29, 547
- Busso, M., Gallino, R., & Wasserburg, G. J. 1999, [ARA&A](#), 37, 239
- Carbone, A., & Schwenk, A. 2019, [PhRvC](#), 100, 025805
- Chatziioannou, K. 2020, [GReGr](#), 52, 109
- Chatziioannou, K., Clark, J. A., Bauswein, A., et al. 2017, [PhRvD](#), 96, 124035
- Combi, L., & Siegel, D. M. 2023, [ApJ](#), 944, 28
- Constantinou, C., Muccioli, B., Prakash, M., & Lattimer, J. M. 2015, [PhRvC](#), 92, 025801
- Côté, B., Eichler, M., Arcones, A., et al. 2019, [ApJ](#), 875, 106
- Coulter, D. A., Foley, R. J., Kilpatrick, C. D., et al. 2017, [Sci](#), 358, 1556
- Courant, R., Friedrichs, K., & Lewy, H. 1928, [MatAn](#), 100, 32
- Cowan, J. J., Sneden, C., Lawler, J. E., et al. 2021, [RvMP](#), 93, 015002

- Cowperthwaite, P. S., Berger, E., Villar, V. A., et al. 2017, [ApJ](#), 848, L17
- De, S., Finstad, D., Lattimer, J. M., et al. 2018, [PhRvL](#), 121, 091102
- Dean, C., Fernández, R., & Metzger, B. D. 2021, [ApJ](#), 921, 161
- Dessart, L., Ott, C. D., Burrows, A., Rosswog, S., & Livne, E. 2009, [ApJ](#), 690, 1681
- Díaz, M. C., Macri, L. M., Lambas, D. G., et al. 2017, [ApJ](#), 848, L29
- Dietrich, T., Hinderer, T., & Samajdar, A. 2021, [GReGr](#), 53, 27
- Dietrich, T., Ujevic, M., Tichy, W., Bernuzzi, S., & Brüggmann, B. 2017, [PhRvD](#), 95, 024029
- Domoto, N., Tanaka, M., Kato, D., et al. 2022, [ApJ](#), 939, 8
- Dormand, J. R., & Prince, P. J. 1980, [JCoAM](#), 6, 19
- Drischler, C., Hebeler, K., & Schwenk, A. 2016, [PhRvC](#), 93, 054314
- . 2019, [PhRvL](#), 122, 042501
- Drout, M. R., Piro, A. L., Shappee, B. J., et al. 2017, [Sci](#), 358, 1570
- East, W. E., Paschalidis, V., & Pretorius, F. 2016a, [CQGra](#), 33, 244004
- East, W. E., Paschalidis, V., Pretorius, F., & Shapiro, S. L. 2016b, [PhRvD](#), 93, 024011
- Einfeldt, B. 1988, [SJNA](#), 25, 294
- Einstein, A. 1916, Sitzungsberichte der Königlich Preußischen Akademie der Wissenschaften, 688
- Evans, P. A., Cenko, S. B., Kennea, J. A., et al. 2017, [Sci](#), 358, 1565
- Fahlman, S., & Fernández, R. 2022, [MNRAS](#), 513, 2689
- Fan, Y. Z., Wu, X. F., & Wei, D. M. 2013, [PhRvD](#), 88, 067304
- Fernández, R., Foucart, F., & Lippuner, J. 2020, [MNRAS](#), 497, 3221
- Fernández, R., & Metzger, B. D. 2013, [MNRAS](#), 435, 502
- . 2016, [ARNPS](#), 66, 23
- Fonseca, E., Cromartie, H. T., Pennucci, T. T., et al. 2021, [ApJL](#), 915, L12
- Foucart, F., Mösta, P., Ramirez, T., et al. 2021, [PhRvD](#), 104, 123010
- Freiburghaus, C., Rembges, J.-F., Rauscher, T., et al. 1999, [ApJ](#), 516, 381
- Fujibayashi, S., Kiuchi, K., Nishimura, N., Sekiguchi, Y., & Shibata, M. 2018, [ApJ](#), 860, 64
- Fujibayashi, S., Kiuchi, K., Wanajo, S., et al. 2023, [ApJ](#), 942, 39
- Fujibayashi, S., Sekiguchi, Y., Kiuchi, K., & Shibata, M. 2017, [ApJ](#), 846, 114

- Fujibayashi, S., Shibata, M., Wanajo, S., et al. 2020a, [PhRvD](#), 101
- . 2020b, [PhRvD](#), 102
- Fujibayashi, S., Wanajo, S., Kiuchi, K., et al. 2020c, [ApJ](#), 901, 122
- Galeazzi, F., Kastaun, W., Rezzolla, L., & Font, J. A. 2013, [PhRvD](#), 88, 064009
- Godunov, S. K. 1959, *Matematicheskiĭ Sbornik. Novaya Seriya*, 47 (89), 271
- Goodale, T., Allen, G., Lanfermann, G., et al. 2003, in *High Performance Computing for Computational Science — VECPAR 2002*, Vol. 2565 (Springer Berlin Heidelberg), 197–227
- Gottlieb, S., & Shu, C.-W. 1998, [MaCom](#), 67, 73
- Gourgoulhon, E., Grandclément, P., Taniguchi, K., Marck, J.-A., & Bonazzola, S. 2001, [PhRvD](#), 63, 064029
- Haas, R., Brandt, S. R., Gabella, W. E., et al. 2020, The Einstein Toolkit. <https://zenodo.org/record/4298887>
- Hammer, H. W., König, S., & Kolck, U. V. 2020, [RvMP](#), 92, 025004
- Hansen, C. J., Montes, F., & Arcones, A. 2014, [ApJ](#), 797, 123
- Harten, A., Engquist, B., Osher, S., & Chakravarthy, S. R. 1987, [JCoPh](#), 71, 231
- Harten, A., Lax, P. D., van Leer, B., & van Leer, B. 1983, [SIAMR](#), 25, 35
- Hayashi, K., Fujibayashi, S., Kiuchi, K., et al. 2022, [PhRvD](#), 106, 023008
- Hebeler, K., Bogner, S. K., Furnstahl, R. J., Nogga, A., & Schwenk, A. 2011, [PhRvC](#), 83, 031301
- Henkel, A., Foucart, F., Raaijmakers, G., & Nissanke, S. 2023, [PhRvD](#), 107, 063028
- Hewish, A., Bell, S. J., Pilkington, J. D. H., Scott, P. F., & Collins, R. A. 1968, [Nature](#), 217, 709
- Hinder, I., Buonanno, A., Boyle, M., et al. 2013, [CQGra](#), 31, 025012
- Hinderer, T. 2008, [ApJ](#), 677, 1216
- Hix, W. R., & Thielemann, F. K. 1999, [JCoAM](#), 109, 321
- Hotokezaka, K., Kiuchi, K., Kyutoku, K., et al. 2013a, [PhRvD](#), 88, 044026
- . 2013b, [PhRvD](#), 87, 024001
- Hotokezaka, K., & Nakar, E. 2020, [ApJ](#), 891, 152
- Hu, L., Wu, X., Andreoni, I., et al. 2017, [SciBu](#), 62, 1433
- Hu, X. Y., Adams, N. A., & Shu, C. W. 2013, [JCoPh](#), 242, 169
- Huang, K. 1987, *Statistical Mechanics* (Wiley)
- Hulse, R. A., & Taylor, J. H. 1975, [ApJ](#), 201, L55

-
- Jacobi, M., Guercilena, F. M., Huth, S., et al. 2023, Effects of Nuclear Matter Properties in Neutron Star Mergers, arXiv. <https://arxiv.org/abs/2309.09233>
- Janka, H. T., & Bauswein, A. 2022, [arXiv](#)
- Just, O., Bauswein, A., Ardevol Pulpillo, R., et al. 2015, [MNRAS](#), 448, 541
- Just, O., Goriely, S., Janka, H.-T., Nagataki, S., & Bauswein, A. 2021, [MNRAS](#), 509, 1377
- Just, O., Obergaulinger, M., Janka, H.-T., Bauswein, A., & Schwarz, N. 2016, [ApJ](#), 816, L30
- Käppeler, F., Gallino, R., Bisterzo, S., & Aoki, W. 2011, [RvMP](#), 83, 157
- Kasen, D., Badnell, N. R., & Barnes, J. 2013, [ApJ](#), 774, 25
- Kasliwal, M. M., Nakar, E., Singer, L. P., et al. 2017, [Sci](#), 358, 1559
- Kastaun, W., Ciolfi, R., & Giacomazzo, B. 2016, [PhRvD](#), 94, 044060
- Kastaun, W., & Galeazzi, F. 2015, [PhRvD](#), 91, 064027
- Kawaguchi, K., Shibata, M., & Tanaka, M. 2018, [ApJ](#), 865, L21
- Keller, J., Hebel, K., & Schwenk, A. 2023, [Phys. Rev. Lett.](#), 130, 072701
- Keller, J., Wellenhofer, C., Hebel, K., & Schwenk, A. 2021, [Phys. Rev. C](#), 103, 055806
- Kiuchi, K., Fujibayashi, S., Hayashi, K., et al. 2022, [arXiv](#)
- Kiuchi, K., Kawaguchi, K., Kyutoku, K., Sekiguchi, Y., & Shibata, M. 2020, [PhRvD](#), 101, 084006
- Kreiss, H. O., & Lorenz, J. 1989, Initial-Boundary Value Problems and the Navier-Stokes Equations (Society for Industrial and Applied Mathematics (SIAM, 3600 Market Street, Floor 6, Philadelphia, PA 19104))
- Kulkarni, S. R. 2005, [arXiv](#), astro-ph/0510256
- Lasky, P. D., Haskell, B., Ravi, V., Howell, E. J., & Coward, D. M. 2014, [PhRvD](#), 89, 047302
- Lattimer, J., Pethick, C., Ravenhall, D., & Lamb, D. 1985, [NuPhA](#), 432, 646
- Lattimer, J. M., & Prakash, M. 2016, [PhR](#), 621, 127
- Lattimer, J. M., & Swesty, D. F. 1991, [NuPhA](#), 535, 331
- Lazzati, D., Perna, R., Morsony, B. J., et al. 2018, [PhRvL](#), 120, 241103
- Lehner, L., Liebling, S. L., Palenzuela, C., & Motl, P. M. 2016, [PhRvD](#), 94, 043003
- LeVeque, R. J. 1992, Numerical Methods for Conservation Laws, 2nd edn., Lectures in Mathematics ETH Zürich (Basel ; Boston: Birkhäuser Verlag)
- Li, L.-X., & Paczyński, B. 1998, [ApJ](#), 507, L59
- Lindquist, R. W. 1966, [AnPhy](#), 37, 487

- Lippuner, J., Fernández, R., Roberts, L. F., et al. 2017, [MNRAS](#), 472, 904
- Lipunov, V. M., Gorbovskoy, E., Kornilov, V. G., et al. 2017, [ApJ](#), 850, L1
- Liu, X.-D., Osher, S., & Chan, T. 1994, [JCoPh](#), 115, 200
- Löffler, F., Faber, J., Bentivegna, E., et al. 2012, [CQGra](#), 29, 115001
- Loffredo, E., Perego, A., Logoteta, D., & Branchesi, M. 2023, [A&A](#), 672, A124
- Maione, F., Pietri, R. D., Feo, A., et al. 2017, [PhRvD](#), 96, 063011
- Margalit, B., & Metzger, B. D. 2017, [ApJL](#), 850, L19
- Metzger, B. D. 2020, [LRR](#), 23, 1
- Metzger, B. D., Bauswein, A., Goriely, S., & Kasen, D. 2015, [MNRAS](#), 446, 1115
- Metzger, B. D., & Fernández, R. 2014, [MNRAS](#), 441, 3444
- Metzger, B. D., Martínez-Pinedo, G., Darbha, S., et al. 2010, [MNRAS](#), 406, 2650
- Miller, J. M., Ryan, B. R., Dolence, J. C., et al. 2019, [PhRvD](#), 100, 023008
- Miller, M. C., Lamb, F. K., Dittmann, A. J., et al. 2021, [ApJL](#), 918, L28
- Molero, M., Romano, D., Reichert, M., et al. 2021, [MNRAS](#), 505, 2913
- Most, E. R., Papenfort, L. J., Weih, L. R., & Rezzolla, L. 2020, [MNRAS](#), 499, L82
- Most, E. R., & Raithel, C. A. 2021, [PhRvD](#), 104, 124012
- Nakar, E. 2020, [PhR](#), 886, 1
- Nathanail, A., Most, E. R., & Rezzolla, L. 2021, [ApJL](#), 908, L28
- Nedora, V., Bernuzzi, S., Radice, D., et al. 2019, [ApJ](#), 886, L30
- Nedora, V., Radice, D., Bernuzzi, S., et al. 2021a, [MNRAS](#), 506, 5908
- Nedora, V., Bernuzzi, S., Radice, D., et al. 2021b, [ApJ](#), 906, 98
- Nedora, V., Schianchi, F., Bernuzzi, S., et al. 2021c, [CQGra](#), 39, 015008
- Neilsen, D., Liebling, S. L., Anderson, M., et al. 2014, [PhRvD](#), 89, 104029
- Newman, E., & Penrose, R. 1962, [JMP](#), 3, 566
- O'Connor, E., & Ott, C. D. 2010, [CQGra](#), 27, 114103
- Oppenheimer, J. R., & Volkoff, G. M. 1939, [PhRv](#), 55, 374
- Paschalidis, V., East, W. E., Pretorius, F., & Shapiro, S. L. 2015, [PhRvD](#), 92, 121502
- Paschalidis, V., & Stergioulas, N. 2017, [LRR](#), 20, 1

-
- Perego, A., Radice, D., & Bernuzzi, S. 2017, *ApJ*, 850, L37
- Perego, A., Rosswog, S., Cabezón, R. M., et al. 2014, *MNRAS*, 443, 3134
- Pian, E., D’Avanzo, P., Benetti, S., et al. 2017, *Nature*, 551, 67
- Piran, T., Nakar, E., & Rosswog, S. 2013, *MNRAS*, 430, 2121
- Pozanenko, A. S., Barkov, M. V., Minaev, P. Yu., et al. 2018, *ApJ*, 852, L30
- Radice, D., Bernuzzi, S., & Ott, C. D. 2016, *PhRvD*, 94, 064011
- Radice, D., Bernuzzi, S., & Perego, A. 2020, *ARNPS*, 70, 95
- Radice, D., Perego, A., Hotokezaka, K., et al. 2018, *ApJ*, 869, 130
- Radice, D., & Rezzolla, L. 2012, *A&A*, 547, A26
- Radice, D., Rezzolla, L., & Galeazzi, F. 2014a, *MNRAS*, 437, L46
- . 2014b, *CQGra*, 31, 075012
- Raithel, C. A., Paschalidis, V., & Özel, F. 2021, *PhRvD*, 104, 063016
- Reisswig, C., & Pollney, D. 2011, *CQGra*, 28, 195015
- Rezzolla, L., Most, E. R., & Weih, L. R. 2018, *ApJL*, 852, L25
- Rezzolla, L., & Takami, K. 2016, *PhRvD*, 93, 124051
- Rezzolla, L., & Zanotti, O. 2013, *Relativistic Hydrodynamics*, 1st edn. (Oxford: Oxford Univ. Press)
- Riley, T. E., Watts, A. L., Bogdanov, S., et al. 2019, *ApJL*, 887, L21
- Riley, T. E., Watts, A. L., Ray, P. S., et al. 2021, *ApJL*, 918, L27
- Rosswog, S. 2013, *Philosophical Transactions Of Royal Society A*, 371, 20120272
- Rosswog, S., & Liebendörfer, M. 2003, *MNRAS*, 342, 673
- Rosswog, S., Sollerman, J., Feindt, U., et al. 2018, *A&A*, 615
- Ruffert, M., Janka, H. T., & Schaefer, G. 1995, *astro ph*
- Ruiz, M., Lang, R. N., Paschalidis, V., & Shapiro, S. L. 2016, *ApJ*, 824, L6
- Runge, C. 1901, *Zeitschrift Für Mathematik Physik*, 224
- Schneider, A. d. S., Roberts, L. F., & Ott, C. D. 2018, SROEOS. <https://bitbucket.org/andschn/sroeos/src/master/>
- Schneider, A. S., Roberts, L. F., & Ott, C. D. 2017, *PhRvC*, 96, 065802
- Schneider, A. S., Roberts, L. F., Ott, C. D., & O’Connor, E. 2019, *PhRvC*, 100, 055802

- Schnetter, E., Hawley, S. H., & Hawke, I. 2004, [CQGra](#), 21, 1465
- Sekiguchi, Y., Kiuchi, K., Kyutoku, K., & Shibata, M. 2015, [PhRvD](#), 91, 064059
- Sekiguchi, Y., Kiuchi, K., Kyutoku, K., Shibata, M., & Taniguchi, K. 2016, [PhRvD](#), 93, 124046
- Shen, H., Toki, H., Oyamatsu, K., & Sumiyoshi, K. 1998a, [PThPh](#), 100, 1013
- . 1998b, [NuPhA](#), 637, 435
- . 2011, [ApJS](#), 197, 20
- Shibata, M. 1999, [PThPh](#), 101, 1199
- . 2015, 100 Years of General Relativity, Vol. 1, Numerical Relativity (WORLD SCIENTIFIC), doi: [10.1142/9692](#)
- Shibata, M., Fujibayashi, S., & Sekiguchi, Y. 2021, [PhRvD](#), 104, 63026
- Shibata, M., Kiuchi, K., Sekiguchi, Y. I., & Suwa, Y. 2011, [PThPh](#), 125, 1255
- Shibata, M., & Nakamura, T. 1995, [PhRvD](#), 52, 5428
- Shibata, M., Zhou, E., Kiuchi, K., & Fujibayashi, S. 2019, [PhRvD](#), 100, 023015
- Siegel, D. M. 2019, [EPJA](#), 55
- Siegel, D. M., & Metzger, B. D. 2017, [PhRvL](#), 119, 231102
- . 2018, [ApJ](#), 858, 52
- Sieverding, A., Waldrop, P. G., Harris, J. A., et al. 2023, [ApJ](#), 950, 34
- Smartt, S. J., Chen, T. W., Jerkstrand, A., et al. 2017, [Nature](#), 551, 75
- Snedden, C., Cowan, J. J., & Gallino, R. 2008, [ARA&A](#), 46, 241
- Steiner, A. W., Hempel, M., & Fischer, T. 2013, [ApJ](#), 774, 17
- Stergioulas, N., Bauswein, A., Zagkouris, K., & Janka, H. T. 2011, [MNRAS](#), 418, 427
- Stone, J. R., & Reinhard, P. G. 2007, [PrPNP](#), 58, 587
- Sugahara, Y., & Toki, H. 1994, [NuPhA](#), 579, 557
- Suresh, A., & Huynh, H. T. 1997, [JCoPh](#), 136, 83
- Takami, K., Rezzolla, L., & Baiotti, L. 2014, [PhRvL](#), 113, 091104
- . 2015, [PhRvD](#), 91, 064001
- Tanaka, M., & Hotokezaka, K. 2013, [ApJ](#), 775, 113
- Tanaka, M., Kato, D., Gaigalas, G., et al. 2018, [ApJ](#), 852, 109
- Tanvir, N. R., Levan, A. J., González-Fernández, C., et al. 2017, [ApJ](#), 848, L27

- Taylor, J. H., & Weisberg, J. M. 1982, [ApJ](#), 253, 908
- Thorne, K. S. 1981, [MNRAS](#), 194, 439
- Timmes, F. X., & Arnett, D. 1999, [ApJS](#), 125, 277
- Tolos, L., & Fabbietti, L. 2020, [PrPNP](#), 112, 103770
- Travaglio, C., Gallino, R., Arnone, E., et al. 2004, [ApJ](#), 601, 864
- Troja, E., Piro, L., Eerten, H. V., et al. 2017, [Nature](#), 551, 71
- Troja, E., van Eerten, H., Zhang, B., et al. 2020, [MNRAS](#), 498, 5643
- Utsumi, Y., Tanaka, M. M., Tominaga, N., et al. 2017, [PASJ](#), 69, 101
- Valenti, S., Sand, J. D., Yang, S., et al. 2017, [ApJ](#), 848, L24
- van der Vorst, H. A. 1992, [SJSC](#), 13, 631
- van Riper, K. A., & Lattimer, J. M. 1981, [ApJ](#), 249, 270
- Villar, V. A., Guillochon, J., Berger, E., et al. 2017, [ApJ](#), 851, L21
- Virtanen, P., Gommers, R., Oliphant, T. E., et al. 2020, [NatMe](#), 17, 261
- Wang, M., Audi, G., Kondev, F. G., et al. 2017, [ChPhC](#), 41, 030003
- Watson, D., Hansen, C. J., Selsing, J., et al. 2019, [Nature](#), 574, 497
- Waxman, E., Ofek, E. O., Kushnir, D., & Gal-Yam, A. 2018, [MNRAS](#), 481, 3423
- Xie, X., Zrake, J., & MacFadyen, A. 2018, [ApJ](#), 863, 58
- Yasin, H., Schäfer, S., Arcones, A., & Schwenk, A. 2020, [PhRvL](#), 124, 092701
- Zhang, B., & Mészáros, P. 2001, [ApJ](#), 552, L35

Acknowledgements

At this point, I want to thank you to everyone who has supported me in the past years. Especially to Almudena Arcones, for supervising me during my master's and Ph.D. thesis, for enabling many participations in schools and conferences, and generally for introducing me to the world of nuclear astrophysics. It has been a privilege to be a part of your group for over five years now.

Thank you Kai Hebel for many helpful discussions on nuclear theory and for agreeing to be the second assessor for this thesis.

Very special thanks go to Federico Guercilena. You have taught me so much and answered many stupid questions along the way. I hope we keep working together and complete what we have started.

I would like to thank all my collaborators: Sabrina Huth for creating the original EOS tables and providing new ones on short notice and Bruno Giacomazzo, Wolfgang Kastaun, Takami Kuroda, and Martin Obergaulinger for supporting Federico and me during the implementation of the 2D setup.

My work heavily relied on many open-source projects: the Einstein toolkit, WhiskyTHC, the SROEOS code, the python packages numpy and scipy, and many more. I want to thank the authors and maintainers for their effort.

In my time in the nuclear astrophysics group, I have had the pleasure to work, discuss, drink coffee, and generally hang out with the old generation: Carlos, Federico, Hannah, Jonas, Julia, Marius, Martin, Max, Moritz, and Takami, and the new generation: Finia, Gerard, Giacomo, Jan, and Thanasis. Thank you for creating such a warm and welcoming atmosphere within this group. Special thanks go to Gerard, Giacomo, Hannah, Jonas, Kevin, Moritz, and Thanasis for many fun evenings in the Ratskeller, Grohe, the bouldering gym, and playing board games.

I also want to thank my friends Jochen, Richard, Sammy, and Steven although they are bad at SSB64. My family and especially my mother have always supported me, thank you for all you have done for me. Tatjana, I could not be happier to have you by my side. Thank you for all your support and patience over the past seven years, especially during the last months of writing my thesis.

This work was supported by the Deutsche Forschungsgemeinschaft (DFG, German Research Foundation) - Project-ID 279384907 - SFB 1245 and the European Research Council Grant No. 677912 EUROPIUM. The simulations were performed on the national supercomputer HPE Apollo Hawk at the High Performance Computing (HPC) Center Stuttgart (HLRS) under the grant microBNS/44163.

*It's the kind of thing that makes you
glad you stopped and smelled the pine
trees along the way, you know?*

— Gabro

Curriculum Vitae

Maximilian Jacobi

2019 – 2023 Doctoral studies and member of the scientific staff,
TU Darmstadt, Germany

January 2nd 2019 Master's degree, thesis title: "Influence of astrophysical and nuclear
physics uncertainties on the nucleosynthesis in proton-rich
neutrino-driven winds"

2016 – 2019 Master studies, TU Darmstadt, Germany

January 14th 2016 Bachelor's degree, thesis title: "Theoretical exploration of the
neutron-rich region of the nuclear chart"

2012 – 2016 Bachelor studies, TU Darmstadt, Germany

Erklärungen laut Promotionsordnung

§ 8 Abs. 1 lit. c PromO

Ich versichere hiermit, dass die elektronische Version meiner Dissertation mit der schriftlichen Version übereinstimmt.

§ 8 Abs. 1 lit. d PromO

Ich versichere hiermit, dass zu einem vorherigen Zeitpunkt noch keine Promotion versucht wurde. In diesem Fall sind nähere Angaben über Zeitpunkt, Hochschule, Dissertationsthema und Ergebnis dieses Versuchs mitzuteilen.

§ 9 Abs. 1 PromO

Ich versichere hiermit, dass die vorliegende Dissertation selbstständig und nur unter Verwendung der angegebenen Quellen verfasst wurde.

§ 9 Abs. 2 PromO

Die Arbeit hat bisher noch nicht zu Prüfungszwecken gedient.

Darmstadt, 6. Februar 2023

M. Jacobi